Institute of Solid State Research (IFF)
Quantum Theory of Materials (IFF-1)

Tomographic Problems in the Diagnostics of Fuel Cell Stacks

Julian Hirschfeld

JÜLICH
FORSCHUNGSZENTRUM

Tomographic Problems in the Diagnostics of Fuel Cell Stacks

Julian Hirschfeld

Universität Duisburg-Essen

Fachbereich Physik

Studiengang: Physik Diplom II

Tomographic problems in the diagnostics of fuel cell stacks

Diplomarbeit von *Julian Hirschfeld*

angefertigt im

Forschungszentrum Jülich

Institut für Festkörperforschung (IFF)

16. März 2009

This is a slightly modified version of my diploma thesis based on new insights. Some descriptions have been altered, whereas no results have been changed.

Contents

List of Tables

Abstract

A novel scheme for detecting inhomogeneous internal currents in a fuel cell stack is suggested. Plates of high conductivity, including small parallel slits, are placed between each fuel cell in a stack. These may consist of aluminum. In this diploma thesis the scheme is investigated for the case that the flowfield plates in use consist of graphite. Whenever a local inhomogeneity in the current density of a particular cell occurs, currents in the adjacent metal plates emerge to compensate the difference to the next cell's current density distribution. Due to the slits in the metal plates, these currents are enforced to the surface of the stack, where they can be detected more easily. Further effects of the metal plates are first, the high conductivity of the small plates completely prevents the inhomogeneities from spreading to neighboring cells. And secondly, even at the particular cell the inhomogeneity is distributed equally over the undamaged area of the cell. Thus this scheme leads to much better diagnostic possibilities and at the same time reduces electric instabilities to an extent where they probable become harmless. This scheme will be explained first in a simple model to clarify the idea. But very precise 3 dimensional computations using realistic parameters, representing real fuel cell materials, are presented corroborating the results of the simple model. On the basis of the measured surface currents, information about anomalies of the currents in the MEA can be obtained by using the methods of tomography. Unfortunately tomography alone does not lead to unique results in this case. But when assuming plausible defect structures one can exclude improbable deficiencies by applying a special form of simulated annealing. In this way most defects can be localized and their extent be determined.

Zusammenfassung

Es wird ein neuartiges Schema zur Bestimmung ungleichmäßiger interner Ströme in einem Brennstoffzellen Stapel vorgeschlagen. Platten hoher Leitfähigkeit, die kleine parallele Schlitze enthalten, werden zwischen jede Brennstoffzelle in einem Stapel gesetzt. Diese können zum Beispiel aus Aluminium bestehen. In dieser Diplomarbeit wird dieses Schema für den Fall untersucht, dass die Bipolarplatten aus Graphit bestehen. Tauchen Inhomogenitäten in der Stromdichte einer Zelle auf, bilden sich Ströme in den anliegenden Metallplatten, welche den Unterschied zu der Stromdichteverteilung der folgenden Zelle ausgleichen. Die Schlitze in der Platte zwingen diese Ausgleichsströme an die Oberfläche des Stapels, wo sie besser detektiert werden können. Weitere Effekte der Metallplatten sind erstens, dass es durch die sehr hohe elektrische Leitfähigkeit möglich ist die Stromdichteverteilungen der einzelnen Brennstoffzellen voneinander zu entkoppeln, wodurch Ungleichmäßigkeiten im elektrischen Strom sich nicht mehr auf benachbarte Zellen ausbreiten können. Und zweitens, dass sogar in der defekten Brennstoffzelle die Stromverteilung so ausgeglichen wird, dass es zu keinen Stromspitzen an Rändern von Defekten kommt. Dieses Schema führt somit sowohl zu viel besserer Diagnostik als auch zu einem stabileren Betrieb von Brennstoffzellenstapeln. Zuerst wird diese Methode in einem einfachen analytischen Modell erläutert. Allerdings werden dessen Ergebnisse durch sehr präzise dreidimensionale Berechnungen unter Verwendung realistischer Parameter, die reale Brennstoffzellenmaterialien repräsentieren, untermauert. Auf Basis der gemessenen Oberflächenströme können, durch Verwendung von tomographischen Verfahren, Informationen über Strom Anomalien erhalten werden. Unglücklicherweise führt in diesem Fall das Anwenden von Tomographie allein zu keinen eindeutigen Ergebnissen. Allerdings durch Annahme sinnvoller Defektstrukturen ist es, durch die Anwendung einer speziellen Art von Simulated Annealing, möglich unwahrscheinliche Mängel auszuschließen. Auf diesem Weg können die meisten Defekte lokalisiert und deren Ausdehnung bestimmt werden.

1 Introduction

A fuel cell is a galvanic element similar to a battery. A galvanic element converts chemical energy directly into electrical energy. In a battery the reducing agent and the oxidizing agent are stored inside. If all of the reducing agent is oxidized and all of the oxidizing agent is reduced, the battery is depleted and cannot produce any more current. In an accumulator battery the electrochemical processes occurring in the discharge can be reverted by applying an opposite current. Thus the battery can be recharged, at least partly, since memory effects[1] may prevent the completion of this process. Contrary to the battery, the fuel cell converts chemical energy of constantly added fuel into electrical energy. As fuel cells cannot deplete, there is in principle no upper limit for energy conversion, but in fact degradation takes place. Thus a fuel cell has also a limited lifetime, which does not depend on a specific amount of stored fuel. The causes of degradation are manifold and part of current research. Due to the wide spectrum of degradation effects the maximal lifetime of fuel cells vary between a few thousand hours and some ten thousand hours [1, 2]. Better diagnostics for fuel cell applications and stabilization of the operation by inhibition of damage spread would clearly contribute to a longer and more stable lifetime.

The heart of a low temperature fuel cell is the **M**embrane **E**lectrode **A**ssembly (MEA) covered on both sides with flowfield plates (typically consisting of graphite or steel[3]), in which the gases or fluids of the fuel as well as the exhaust gases are transported. Since a single fuel cell can typically produce a voltage of about $0.3\,\mathrm{V}$ (DMFC), $0.7\,\mathrm{V}$ (PEMFC) to $0.9\,\mathrm{V}$ (SOFC) [4] only, several or many (about 100) fuel cells are connected - usually in series - forming a stack[5]. There are interesting modifications of connecting fuel cells[6] but for simplicity only the standard case (c.f. Fig. (1.1)) is taken into consideration.

It is not a trivial engineering task to keep even a single fuel cell in a stable state[7] for a very long period even if the power requirements remain constant over that period. The efficiency depends on the temperature, humidity[8] of the polymeric electrolyte[2] and on fuel as well as exhaust gas conditions[9, 10, 11]. All this can lead to irregularities in the local electric current density produced by the MEA. Therefore the current density can differ by a factor of 1.5 - 3 in a single MEA[12, 13, 14]. And here lies a problem of the stack: An irregular electric current of one cell, still harmless for this one, may accumulate due to the fact that the next fuel cells in series or the preceding ones or both are influenced by these irregularities[15].

---

[1]The memory effect occurs in some types of accumulators, if recharged prior to complete depletion. E.g. in a $NiCd$ accumulator cadmium crystals are eliminated and are by that no longer available for the electrochemical reaction.

[2]Of course this problem occurs only in fuel cells, whose electrolyte is in fact a polymer membrane, namely *proton exchange membrane fuel cell* and *direct methanol fuel cell*.
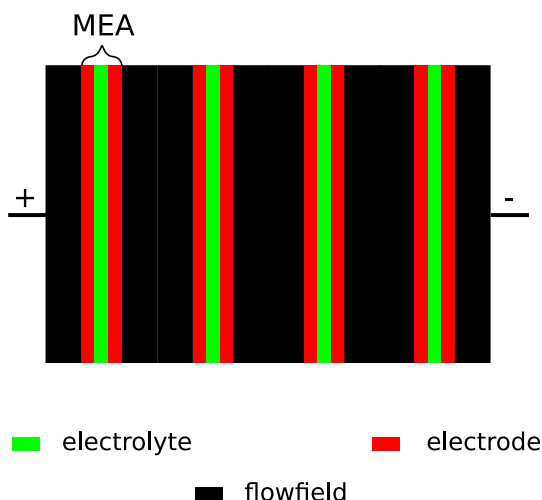
Figure 1.1: Schematic view of a standard low temperature (less than $250°C$) fuel cell stack with 4 single cells. The 4 **M**embrane **E**lectrode **A**ssembly (MEA) plates containing two catalytic and one electrolyte layers each are embedded between the flowfield plates.

It is therefore mandatory

- to have good diagnostics available by which irregularities of the currents occurring at one cell can be detected enabling to change parameters and thus reduce the irregularities.

- finding some means effectively suppressing the tendency for irregularities.

If one cell gets damaged (due to e.g. oxidation of the catalyst) it is difficult to locate the particular cell. For a single cell some diagnostic methods to gain knowledge about the current density distribution are known. Three methods have been presented by Stumper et al. [16], the partial MEA approach, the sub-cell method and the current distribution mapping. The last method is the most advanced one of these three, because it provides a highly resolved current density map by measuring the current directly at many locations of the cell. Although the method is highly advanced, it can only be applied to a single fuel cell and is not eligible to be applied to a fuel cell in a commercial product. Diagnostic methods, which can be applied to a fuel cell stack are the electrochemical impedance spectroscopy (EIS) [17] and the current interruption method [18]. Using these methods one can gain knowledge about different kinds of defects in a particular fuel cell of a stack. However, it provides only integrated information for entire cells. A further possibility consists of measuring the magnetic field and obtaining information about inner currents by applying magnetotomography[19, 20]. At first sight this method looks very promising, but suffers from the difficulty that the fields to be measured are small (of the order of the magnetic field of the earth). In fact hitherto the method has only been discussed for single cell problems[21].

A scheme which fulfills both the above requirements is developed[34]. In the present form it is most easily applied to stacks with graphite flowfield plates. The idea is simple:

Highly conducting plates (e.g. made of aluminum) positioned between the cells will enforce a smoothing of the normal currents in the MEAs of the cells. (Throughout this thesis *normal* currents denote currents pointing in stack direction[3]. All currents being orthogonal to *normal* currents are called *transverse* currents. The same nomenclature holds for conductivities.) However, this smoothing out can be achieved only by non negligible transverse currents in the plates. Now slits appropriately placed in the highly conducting plates should guide these parallel currents to the surface of the stack where they can be detected. At the same time the highly conducting plates should suppress any spreading of irregular currents to the adjacent fuel cells in series.

In chapter 2 an overview about the functionality of fuel cells is given. The basics about fuel cell operation and their efficiency is discussed. At the end of this chapter a short survey about some types of fuel cells is presented. The advantages and disadvantages of each type of fuel cells are evaluated. In chapter 3 the above outlined scheme is applied to a simple model containing plates of perfect conductivity. It will be shown that it is in principle possible to get information about the state of individual cells and the location of defects in a cell. Furthermore the inverse problem is adumbrated, which contains the determination of the MEA condition on the basis of the stack surface currents. At this point it will be shown, that problems occur, which cannot be solved by the simple model. First, parasitic effects emerge in real fuel cells reducing the surface currents. Secondly, the spreading of current irregularities and their inhibition by metal plates cannot even be estimated by the simple model. Thirdly, due to the small number of surface currents, the tomographic problem is not unique. These are the three major issues of this diploma thesis. In chapter 4 first the finite-volume method is presented. This method is eligible to calculate potentials (e.g. the electric potential ϕ, the magnetic vector potential $\vec{A}$ or the air pressure p) in a complex body. Subsequently, the simulated annealing method is described. It is a generic statistical optimization algorithm based on the principle of crystallization in nature. Using this, it is possible to find a global minimum among many local ones. In the following chapter the computations regarding the forward problem[4] are repeated but now for a realistic stack with realistic parameters. This requires solutions of partial differential equations in 3 dimensions, which are done by the finite-volume algorithm. It will turn out that the results of the simple model are usable in many cases at least in first order. On the other hand the practical applicability and the extent of the smoothing can only be verified by these numerical computations. The last point in this chapter is the numerical computation of the numerical basis for the inverse problem. It is used to investigate how and to which extent it is possible to determine the condition of the MEA if only the surface currents in the slitted metal plates are known. This investigation is the content of chapter 6. At the end of the thesis a conclusion summing up all results is given.

---

[3]The *normal* currents, pointing in stack direction must not be mistaken for the normal current densities used in the finite-volume method (c.f. Chapter 3), which are defined differently.

[4]The calculation of the current density distribution in the fuel cell for a given MEA condition.

2 Fuel cell functionality

2.1 Operating principle

As mentioned in the introduction a fuel cell is a galvanic element, which converts chemical energy of constantly added fuel into electrical energy. A galvanic element consists of an electrolyte, a cathode, an anode and a casing. To produce an external electrical current between the electrodes, the anode needs to be surrounded by fuel and the cathode by an oxidizing agent. In fuel cells different kinds of fuels, like natural gas, methanol or hydrogen, can be used (depending on the electrolyte). On the cathode side there is only the choice between pure and atmospheric oxygen. The reaction is more efficient if pure oxygen is used, nevertheless air has the advantage of being cheap and omnipresent in terrestrial applications. The most efficient reaction occurs if hydrogen is used as fuel and pure oxygen as the oxidizing agent. It is in addition the simplest reaction from a chemical point of view. A mixture of oxygen and hydrogen is called detonation gas, which reacts highly exothermic. In an exothermic reaction chemical energy is released. Though by burning the detonation gas the chemical energy is completely converted into heat. In the direct reaction

$$H_2 + \frac{1}{2}O_2 \rightarrow H_2O \tag{2.1}$$

a total reaction enthalpy[1] of about $\Delta H^{H_2 0_l} = -286\,\mathrm{KJ \cdot mol^{-1}}$ is released[2], if water is produced in liquid form. However, in a fuel cell the direct reaction is prevented by keeping fuel and oxidizing agent separated. The total reaction is divided into the fuel oxidation at the anode and the oxygen reduction at the cathode:

$$H_2 \rightarrow 2H^+ + 2e^-, \quad \text{anode reaction} \tag{2.2}$$

$$\frac{1}{2}O_2 + 2H^+ + 2e^- \rightarrow H_2O, \quad \text{cathode reaction} \tag{2.3}$$

---

[1]The reaction enthalpy ΔH is the change of heat. The inner energy U of a substance is primarily given by the binding energy of its atoms. The change of inner energy ΔU in a reaction causes a pressure-volume work $p\Delta V$ and a change of heat. Thus, ΔH is given by the change of inner energy minus the pressure-volume work: $\Delta H = \Delta U + p\Delta V$ (in an exothermic reaction ΔU and ΔH is negative).

[2]If chemical energy is released in a reaction, it is called an exothermic reaction and the change of reaction enthalpy is negative. If energy needs to be added to the reactants to keep the reaction running, it is called an endothermic reaction and the change in reaction enthalpy is positive.
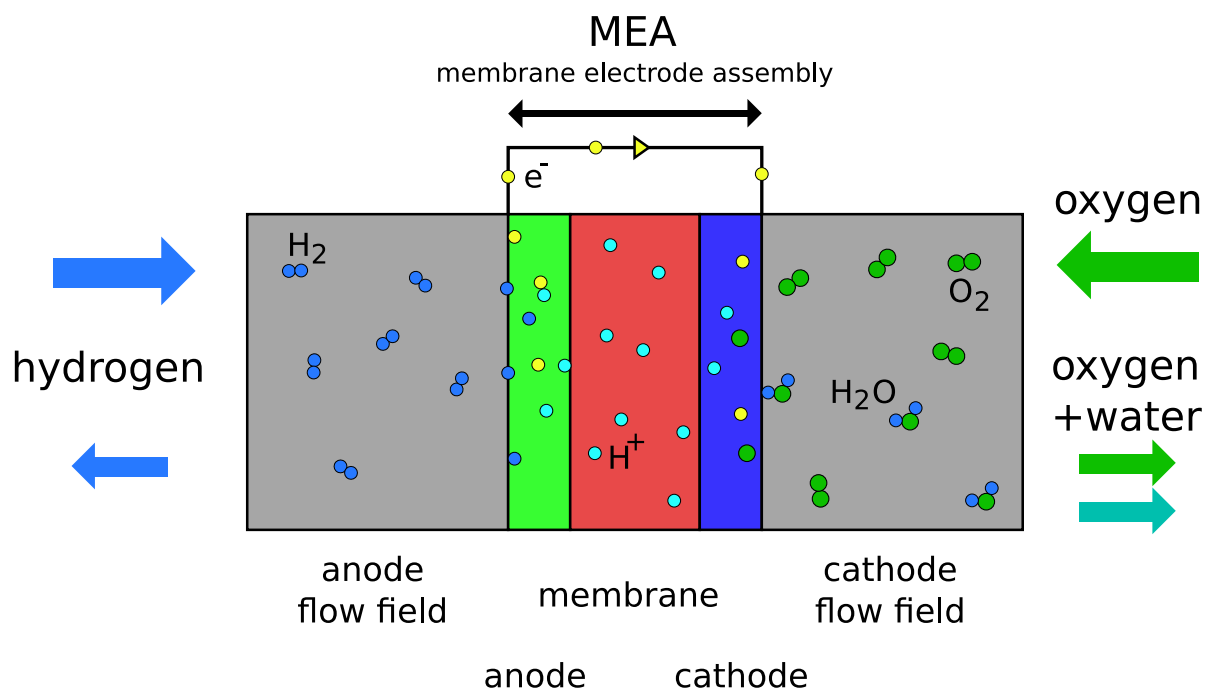
Figure 2.1: Schematic view of a hydrogen-oxygen fuel cell. The hydrogen is blown through the anode flowfield. On the surface of the catalyst inside of the porous anode, the hydrogen molecules are dissociated and the hydrogen atoms are ionized. The H^+ ions permeate across the, electronic isolating and gas blocking, membrane, whereas the electrons pass through an external load. On the cathode side the oxygen dissociates and, together with the hydrogen ions, it is electrochemical reduced to water.

Following the Hess's law[3], the change in the reaction enthalpy in the fuel cell is equal to the one in the direct reaction. Since the direct detonation gas reaction needs thermal energy (the activation energy of an exothermic reaction) in form of a flame or a spark to start, the divided reaction in the fuel cell does not start under normal conditions as well. In low temperature fuel cells there is nearly no thermal energy added, but rather the activation energy of the reactions at the electrodes is lowered by a catalyst. Often the catalyst consists of platinum, because of its high stability in oxidizing and in reducing environment. Since the thermal energy in a high temperature fuel cell is much higher, the catalyst can be less noble. The thermodynamic aspects of the fuel cell reactions are discussed in the following section in more detail.

As any galvanic element a fuel cell consists of an electrolyte, a cathode and an anode, the unification of these components is called **M**embrane **E**lectrode **A**ssembly (MEA). Additionally, there are flowfields on both sides of the MEA to distribute the fuel over the anode surface, and the oxygen respectively over the cathode surface. Since gas

---

[3]The Hess's law has been formulated in 1840 by Germain Hess: *The change of reaction enthalpy is constant, no matter if it runs directly or via many sub-reactions.*[24]

has to reach the electrolyte, the electrodes are porous. In fact the reactions listed in Eq. (2.2) and Eq. (2.3) take place only at **T**hree **P**hase **B**oundaries (TPB), where gas phase, electric conducting catalyst and the ion conducting electrolyte are in contact. The reason is obvious: the hydrogen molecules from the gas phase dissociate on the catalyst surface and then ionize releasing electrons. The hydrogen could also ionize at an arbitrary location on the catalyst surface, but since the ions cannot migrate to the cathode without contact to an ion conductor, they will eventually recombine. As the ions migrate through the membrane, and the electrons cannot, it is possible to bypass the electron current via a load. Further details of the fuel cell structure are shown in Fig. (2.1).

2.2 Thermodynamic aspects

> **The second law of thermodynamics:** *The entropy in a closed adiabatic system tends to increase. Only in a reversible process the change of entropy is zero.*
>
> $$\Delta S \geq 0 \tag{2.4}$$

Due to the second law of thermodynamics Eq. (2.4) only a part of the reaction enthalpy can be transferred into electrical energy. The convertible energy is called Gibbs free energy and is given by:

$$\Delta G = \Delta H - T\Delta S \tag{2.5}$$

Here T denotes the absolute temperature of the system and $T\Delta S$ the heat produced in the reaction due to the change of entropy. Hence, the generates electrical energy W_{el} is given by ΔG, if no other losses occur[4]:

$$W_{\mathrm{el}} = \Delta G \tag{2.6}$$

The molar electric energy is given by the transferred charge $-n \cdot F$ times the voltage U^0, where $F = N_A \cdot e$ is the Faraday constant and N_A is the Avogadro number. F is the total charge of a mol electrons, and n is the number of transferred electrons in a reaction (c.f. Eq. (2.2) and Eq. (2.3)). In a galvanic element the **O**pen **C**ircuit **V**oltage (OCV) U^0 is the voltage between the electrodes without any current flowing. The open circuit voltage is historically called *electromotive force*. But since U^0 have the dimension of a voltage and not that of a force, this name is misleading and U^0 is referred to as OCV. Thus, the Gibbs free energy of the reaction can be written as:

$$\Delta G = -n \cdot F \cdot U^0 \tag{2.7}$$

Respectively the OCV as:

$$U^0 = -\frac{\Delta G}{n \cdot F} \tag{2.8}$$

---

[4]Obviously, this is not the fact in reality, since further energy is converted into heat due to other processes (e.g. Ohm losses). For further details see section 2.4.

Under normal conditions[5] the Gibbs free energy is $\Delta G^0 = -237\,\text{KJ}\cdot\text{mol}^{-1}$, if water is produced in liquid form. Therefore the OCV under normal conditions is:

$$U_0^0 = \frac{237\,\text{KJ}\cdot\text{mol}^{-1}}{2\cdot 96494\,\text{C}\cdot\text{mol}^{-1}} = 1.23\text{V} \tag{2.9}$$

To calculate the OCV for arbitrary temperatures, the temperature dependency of U^0 has to be investigated:

$$\left(\frac{\partial U^0(T)}{\partial T}\right)_p = -\frac{1}{n\cdot F}\cdot\frac{\partial}{\partial T}(\Delta H - T\Delta S) \tag{2.10}$$

$$= \frac{\Delta S}{n\cdot F}$$

If the reaction entropy is constant over a temperature interval ΔT, the temperature dependent OCV can be obtained by integration:

$$U^0(T) = \int_{T_0}^{T}\left(\frac{\partial U^0(T')}{\partial T'}\right)_p dT' = \frac{\Delta S}{n\cdot F}(T - T_0) + U_0^0 \tag{2.11}$$

Since it is not an easy task to determine the entropy change ΔS by experiment, the OCV is measured for different temperatures. As voltage is a relative quantity, the measurement of the electrode potential requires a reference point. A list of electrode voltages in reference to the **N**ormal **H**ydrogen **E**lectrode (NHE) H/H^+ is given in Literature (e.g.[24]). To calculate the actual OCV of a galvanic element, the voltages of both electrodes in reference to the NHE can be looked up and subtracted:

$$\Delta U_0^0 = U_{0|\text{cathode}}^0 - U_{0|\text{anode}}^0 \tag{2.12}$$

For arbitrary conditions, the electrode potentials can be calculated by the Nernst equation[27]

$$U^0 = U_0^0 + \frac{R\cdot T}{n\cdot F}\cdot ln\left(\frac{\prod_i a_{i|\text{ox}}^{\nu_i}}{\prod_j a_{j|\text{red}}^{\nu_j}}\right) \tag{2.13}$$

where R denotes the gas constant, $a_{i|\text{ox}}$ the chemical activity[6] of the oxidizing species, $a_{j|\text{red}}$ the chemical activity of the reducing species and $\nu_{i,j}$ the corresponding stoichiometric coefficient. In the case of the hydrogen fuel cell, in which liquid water is produced,

---

[5]pressure $p^0 = 1013\,\text{hPa}$, temperature $T^0 = 25\,°\text{C}$

[6]By the activity coefficient f $(0 \le f \le 1)$ corrected mole fraction c to describe the deviation from the law of mass action. For higher mole fractions the activity coefficient deviates stronger from unity.

the electrode potential can be calculated by:

$$U^0_{\text{anode}} = U^0_{0|H/H^+} + \frac{R \cdot T}{2 \cdot F} \cdot ln\left(\frac{a^2_{H^+}}{a_{H_2}}\right) \tag{2.14}$$

$$U^0_{\text{cathode}} = U^0_{0|O_2/H^+} + \frac{R \cdot T}{2 \cdot F} \cdot ln\left(\frac{\sqrt{a_{O_2}} \cdot a^2_{H^+}}{a_{H_2O}}\right) \tag{2.15}$$

If the gases are ideal, the activities a_i are equal to their partial pressures p_i. If only liquid water is produced in the cathode, the activity of water a_{H_2O} is unity. Under normal conditions with an air breathing cathode this leads to

$$U^0_{\text{anode}} = 0 \tag{2.16}$$

$$U^0_{\text{cathode}} = 1.23V + \frac{8.314 \, \text{J} \cdot \text{mol}^{-1} \cdot \text{K}^{-1} \cdot 298 \, \text{K}}{2 \cdot 96485 \, \text{C} \cdot \text{mol}^{-1}} \cdot ln\left(\sqrt{0.21}\right) = 1.219 \, \text{V} \tag{2.17}$$

as $U^0_{0|H/H^+}$ is exactly the potential of the NHE (by that zero per definition) and both p_{H+} and p_{H_2} are one. Thus the open circuit voltage of a hydrogen/air fuel cell is $\Delta U = 1.219 \, \text{V}$.

2.3 Fuel cell polarization

Even though it is possible to calculate the theoretical open circuit voltage by Eq. (2.13), it can not be measured in a real fuel cell. Gas permeation across the membrane can occur by which the direct reaction takes place at the cathode. On the one hand the chemical energy stored in the permeated fuel is converted into heat and is thus lost. On the other hand the permeation leads to mixed potentials. Since there is a finite partial pressure of fuel at the cathode, the one of the oxidizing agent is reduced and by that the OCV (c.f. Eq. (2.13)). As the permeation is independent of the current drawn from the fuel cell, it leads to a constant offset in the polarization curve $U(j)$.

Under load there are various effects decreasing the cell voltage. These effects are typically quantized as overpotentials[7] η, which is the deviation of the actual cell voltage U from the theoretical open circuit voltage:

$$\eta = U - U^0 \tag{2.18}$$

The most important overpotentials are:

- Activation overpotential η_A

- Ohmic overpotential η_Ω

- Concentration overpotential η_C

---

[7]The overpotential is also called overvoltage or polarization.
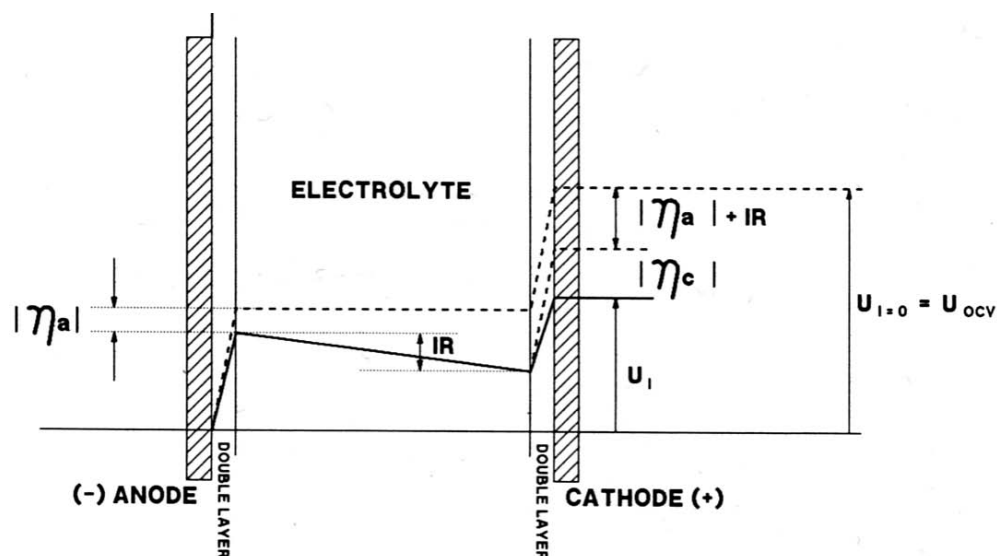
Figure 2.2: The activation overpotential η_A is divided into anodic activation losses η_a and cathodic activation losses η_c. The Ohmic losses are identified by $\eta_\Omega = IR$. The dashed line indicates the voltage without any current drawn from the fuel cell. The continuous line indicates the situation under load.[25]

Ohmic losses occur in all fuel cell parts, but the other two effects take place at the electrodes. Thus they can be separately observed at the anode and at the cathode. The activation overpotential combined with the Ohmic losses across the MEA is shown in Fig. (2.2).

2.3.1 Activation overpotential

Even if no current is drawn from the fuel cell, the reactants dissolve and ionize. Thus surface charges form at the electrode/electrolyte interface. The positive ions concentrate in the electrolyte and the electrons in the electrode. Although the MEA is globally still neutral, an electric field analogous to the one of a plate capacitor forms at the interface. This electric double layer is a further barrier for the ionized species to overcome. So the total potential barrier is given by the intrinsic activation energy of a reaction step plus the double layer potential. Even though the barrier has to be overcome in each reaction step including a material transition, the activation overpotential is given only by the **R**ate **D**etermining **S**tep (RDS)[8]. The current density limited by the activation

---

[8]A reaction can be divided into individual steps, like fuel adsorption on the catalyst or the ionization. Since the reaction rate of the overall reaction is determined by each step, there is always one step with the slowest kinetic. This, figuratively spoken, weakest link of the reaction chain is the rate determining step.

catalyst	$j_0^0 \; [\frac{mA}{cm^2}]$
lead	$2.5 \cdot 10^{-13}$
tin	$3.0 \cdot 10^{-11}$
silver	$4.0 \cdot 10^{-7}$
nickel	$6.0 \cdot 10^{-6}$
platinum	$5.0 \cdot 10^{-4}$
palladium	$4.0 \cdot 10^{-3}$

Table 2.1: Typical reference exchange current densities at normal conditions for various metals.[28]

overpotential is given by the Butler-Volmer Equation[27]:

$$j = j_0 \left[exp\left(\frac{\alpha \cdot \eta_A \cdot n \cdot F}{R \cdot T} \right) - exp\left(-\frac{(1-\alpha) \cdot \eta_A \cdot n \cdot F}{R \cdot T} \right) \right] \qquad (2.19)$$

Besides the known quantities, there is the transfer coefficient α and the exchange current density j_0 in the Butler-Volmer equation. The transfer coefficient α denotes the fraction of the change in activation overpotential, which leads to a change in the reaction rate. For fuel cells this is typically $\alpha = 0.5$. If no current is drawn from the fuel cell, both exponential functions are equal, since the first one represents the anodic partial current density and the second one the cathodic partial current density. The exchange current density j_0 is a function of the effective catalyst surface[9] a, the molar fractions of the reactants at the electrode x and a reference exchange current density j_0^0:

$$j_0 = j_0^0 \cdot x \cdot a \qquad (2.20)$$

The reference exchange current density depends strongly on the catalyst material. Typical values are given in Tab. (2.1). For a hydrogen/oxygen fuel cell, the hydrogen oxidation is much faster than the oxygen reduction. Thus the oxygen reduction is the rate determining step. Under disregard of the anodic activation polarization the Butler-Volmer equation simplifies to:

$$j = -j_0 \cdot exp\left(-\frac{\alpha \cdot n \cdot F}{R \cdot T} \eta_{A,c} \right) \qquad (2.21)$$

Thus the cathodic activation overpotential is given by:

$$\eta_{A,c} = -\frac{R \cdot T}{\alpha \cdot n \cdot F} \cdot ln\left(\frac{|j|}{|j_0|} \right), \quad \text{with } j < 0 \qquad (2.22)$$

---

[9]The effective catalyst surface is the ratio of the active catalyst surface to the geometrical one.

Which is equal to the empirical Tafel equation

$$|\eta_{A,c}| = b \cdot ln\left(\frac{|j|}{|j_0|}\right) \tag{2.23}$$

with the Tafel slope b.

2.3.2 Ohmic overpotential

All electron conductors have finite electronic conductivity and all ion conductors have finite ionic conductivity. Since there are both kinds of conductors present in a fuel cell, Ohmic losses can also be found in fuel cells. Ionic resistances ρ_{ion} emerge in the membrane and in the electrode, electronic resistances ρ_e can be found in the electrode and flowfield plates. Furthermore there are contact resistances between different parts of the fuel cell. As these surface effects can be allocated to either electronic or ionic resistances, they are included in either ρ_e or ρ_{ion}. Altogether these resistances lead to the Ohmic overpotential

$$\eta_\Omega = j(\rho_{ion} + \rho_e) \tag{2.24}$$

with the specific resistances ρ_{ion} and ρ_e.

2.3.3 Concentration overpotential

As soon as current is drawn from the fuel cell, the reactants at the electrodes are consumed in the reactions. Therefore the concentration of fuel in the direct vicinity of the anode and the concentration of oxygen respectively in the direct vicinity of the cathode drops immediately. Due to diffusion the reactants are transported from the flowfield to the TPB, where the reactions take place. At high current densities the fuel and the oxygen is consumed rapidly. Since the diffusion rates in the electrodes are finite, the reactants may not be transported fast enough across the electrode to compensate the consumption. Based on the Butler-Volmer equation, the concentration overpotential can be written as:

$$\eta_C = \frac{2 \cdot R \cdot T}{n \cdot F} \cdot \left[ln\left(\frac{c_{red}}{c_{red}^0}\right) - ln\left(\frac{c_{ox}}{c_{ox}^0}\right)\right], \quad \text{with } \alpha = \frac{1}{2} \tag{2.25}$$

Here, c_{ox} is the concentration of the oxidizing species at the cathode surface, whereas c_{ox}^0 is the concentration of the oxidizing species in the current free case. The same holds for the concentrations of the reducing species c_{red} and c_{red}^0 at the anode surface. The more current is drawn from the fuel cell, the lower the reactant concentration at the electrode surfaces. One can deduce, that there is a limiting current density, at which the concentration of one reactant at the respective electrode surface is zero. Due to the logarithmic dependency, η_C increases rapidly for low concentrations. In virtue of the larger molecule size of oxygen in comparison to hydrogen, the hydrogen diffusion is higher than the on of oxygen. Thus the anodic concentration overpotential can be
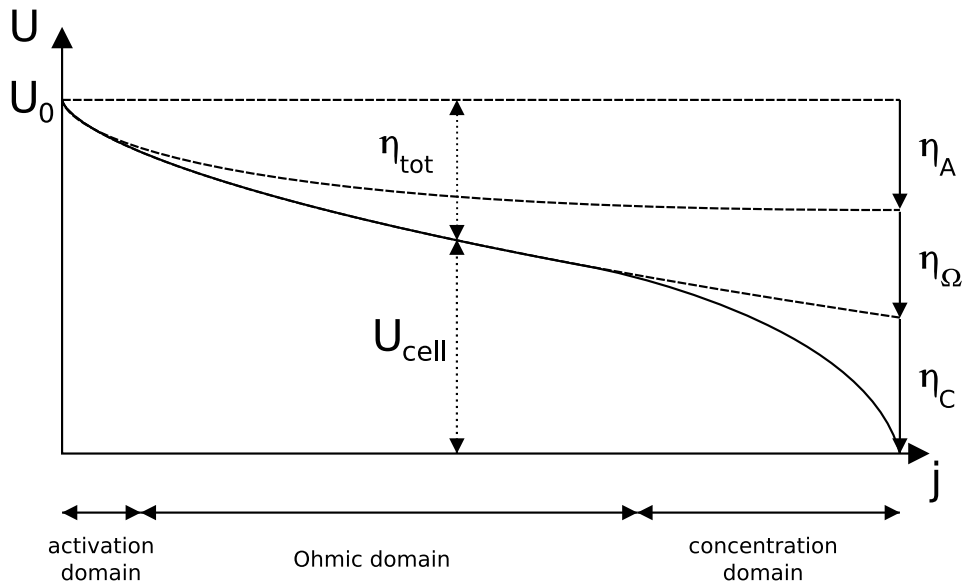
Figure 2.3: A typical polarization curve is governed by the activation overpotential η_A in the low current density domain, by the Ohmic overpotential η_Ω in the intermediate domain, and by the concentration overpotential η_C in the high current density domain. The relation of the losses due to the total overpotential η_{tot} to the remaining cell voltage U_{cell} is shown at a possible operating point.

neglected and the oxygen diffusion becomes the rate determining step at high current densities. Although the fuel diffusion can be neglected at the hydrogen/oxygen fuel cell, the situation is different for the **D**irect **M**ethanol **F**uel **C**ell (DMFC), in which the anode is flooded by a water-methanol mixture and carbon dioxide is produced at the anode. Hence the fuel diffusion to the three phase boundaries is hindered by the evacuation of the CO_2.

2.3.4 The fuel cell polarization curve

These three effects together lead to the typical fuel cell polarization curve. A schematic view of the curve is given in Fig. (2.3). It can be unambiguously divided into three domains. In the low current density domain the activation overpotential leads to a dip. As mentioned before, the activation overpotential is mostly given by the catalyst. Thus, if the catalytic active area is increased, or if palladium is used for the catalyst, the voltage loss in the low current density domain will be reduced. Since these voltage losses affect the cell voltage even at higher current densities, the improvement of the catalyst leads to a higher cell voltage at all current densities.

The polarization curve in the intermediate current density domain has a constant slope, as it is governed by Ohmic losses. To attenuate the voltage losses in the interme-diate domain, the resistances of fuel cell components have to be reduced. This could be
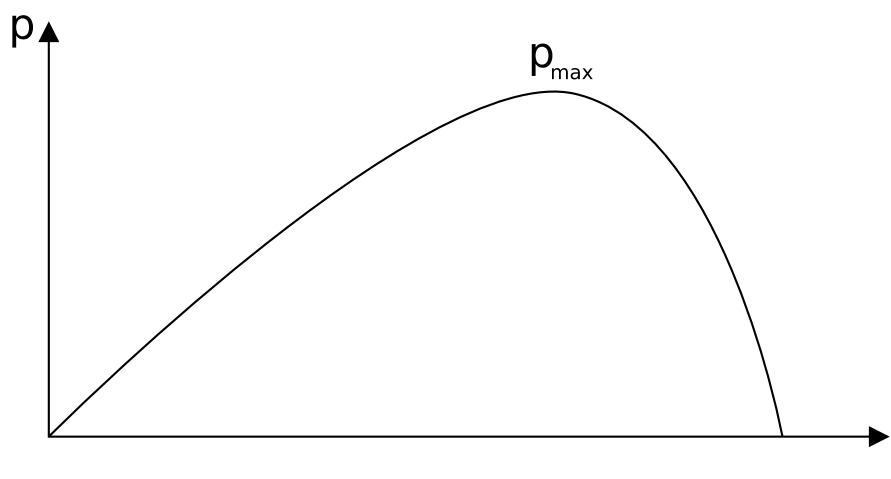
Figure 2.4: Associated with the polarization curve demonstrated in Fig. (2.3) is a power density curve $p(j)$. Since the electric power density is given by $p = j \cdot U$ and the cell voltage drops at high current densities, the fuel cells power density has a maximum p_{max}. It should be mentioned, that the maximal power density might not be the optimal operating point, since the cell voltage and by that the fuel cell efficiency (c.f. section 2.4 paragraph "Voltage efficiency") could already be too low at this current density.

accomplished by diminishing the MEA thickness.

At high current densities, the reactant diffusion to the electrodes becomes the rate determining step. This effect cannot be lowered or even wiped out. However, it is possible to shift the limiting current density to higher values by improving the electrode porosity.

It is possible to define a resistance at the operating point U_{OP} in the polarization curve by $\rho = \partial U_{\mathrm{OP}}/\partial j$. If this point is located in the Ohmic domain, the linearized resistance is valid for rather large deviations $\Delta U = U - U_{\mathrm{OP}}$. This operating point resistance will be important at a later point.

Usually it is meaningful to estimate the fuel cell performance on basis of its maximal electrical power. Therefore power density curves (c.f. Fig. (2.4)) are interesting evaluation tools.

2.4 Fuel cell efficiency

The greatest advantage of fuel cells in comparison to classical combustion engines is the maximal efficiency, since it is not limited by the Carnot efficiency:

$$\eta_{\mathrm{carnot}} = 1 - \frac{T_{\mathrm{low}}}{T_{\mathrm{high}}} \tag{2.26}$$

Thus it is possible to convert much more chemical energy per mol fuel into electrical energy than e.g. in a gas power plant. If fuel cells are used as electrical energy sources for electrotraction, they have to compete with the efficiency of diesel engines, which is less than 45%. But even if the fuel cell efficiency is not bound to the Carnot efficiency, the actual one is much below 100%.

There are some effects determining the overall fuel cell efficiency:

- thermodynamics

- internal voltage losses

- fuel permeation across the membrane

Thermodynamic efficiency   The theoretical maximal efficiency of the fuel cell is given by thermodynamics. Due to the second law of thermodynamics (c.f. Eq. (2.4)) the entropy tends to increase. Thus a fraction of the reaction enthalpy ΔH is always converted into heat. This fraction is given by the change of entropy and the absolute temperature $T\Delta S$. Therefore, the thermodynamic efficiency is given by:

$$\epsilon_{\text{th}} = \frac{\Delta G}{\Delta H} = 1 - \frac{T\Delta S}{\Delta H} \tag{2.27}$$

The change of reaction enthalpy in Eq. (2.1) is $\Delta H = -286\,\text{KJ} \cdot \text{mol}^{-1}$. Under normal conditions with liquid water as the product, the Gibbs free energy is $\Delta G = -237\,\text{KJ} \cdot \text{mol}^{-1}$. Thus the thermodynamic efficiency of the hydrogen/oxygen fuel cell is:

$$\epsilon_{th} = \frac{237\,\text{KJ} \cdot \text{mol}^{-1}}{286\,\text{KJ} \cdot \text{mol}^{-1}} = 0.82 \tag{2.28}$$

This value strongly depends on the chemical reaction. For example the entropy change of the $C + 1/2O_2 \rightarrow CO$ reaction is negative, which can occur in high temperature fuel cells. Therefore, the thermodynamic efficiency of this reaction is larger than one. Though all reactions comes along with positive entropy changes, which are interesting for fuel cell applications.

Voltage efficiency   In virtue of Ohmic losses a resistor in an electrical circuit heats up. The dissipated power is given by $P = RI^2$, with the resistance R of the resistor. This also happens in all electric and ionic conducting materials of fuel cells. A further fraction of the cell voltage is used to run the chemical reaction, which is given by the activation loss. The voltage efficiency combines all losses due to electrode kinetics and Ohmic losses. It is defined by the measurable open circuit voltage U_0 and the actual cell voltage U at a certain current density:

$$\epsilon_{\text{V}} = \frac{U}{U_0} \tag{2.29}$$

This efficiency has typically a value of about:

$$\epsilon_V \approx 0.7 \tag{2.30}$$

Current efficiency   The current efficiency is a combination of the Faradaic efficiency ϵ_F and the fuel utilization N. As it is hardly possible to distribute the fuel homogeneously throughout the MEA, more fuel is blown across the flowfield channels than necessary to run the reaction. The fraction of the fuel injected into the flowfield to the actual needed fuel denotes the utilization. This modifiable factor is typically set to 0.85 [29]. The Faradaic efficiency includes fuel losses due to permeation or leakage. It is defined as the fraction of the cell current I to the theoretical current depending on the reaction speed[10] v.

$$\epsilon_F = \frac{I}{I_{theo}} = \frac{I}{F \cdot n \cdot v} \tag{2.31}$$

Thus the current efficiency is given by:

$$\epsilon_C = \epsilon_F \cdot N = \frac{I \cdot N}{F \cdot n \cdot v} \tag{2.32}$$

If pure hydrogen and pure oxygen is used and neither fuel permeation nor fuel leakage occurs, the Faradaic efficiency is one. In this case the current efficiency is equal to the fuel utilization:

$$\epsilon_C \approx 0.85 \tag{2.33}$$

Overall efficiency   The overall fuel cell efficiency is the product of all individual efficiencies:

$$\epsilon_{FC} = \epsilon_{th} \cdot \epsilon_V \cdot \epsilon_C = \frac{\Delta H - T\Delta S}{\Delta H} \cdot \frac{U}{U_0} \cdot \frac{I \cdot N}{F \cdot n \cdot v} \approx 0.5 \tag{2.34}$$

In this example the efficiency is just by a little margin higher than the maximal diesel engine efficiency. But the spectrum of fuel cell systems is very broad and the efficiency of these differ strongly. By improving the electrode kinetics or running the fuel cell at lower current densities it is possible to increase the efficiency. Furthermore if the fuel utilization is unity, which could be accomplished by fuel recirculation, the efficiency in this example would be about $\epsilon_{FC} \approx 0.58$. The maximal diesel efficiency is obtained only under perfect conditions. For example, the diesel engine efficiency of a car in a traffic congestion drops down to less than 10%. The efficiency of a possible fuel cell driven car would still be much higher. In Fig. (2.5) an efficiency comparison of different power generating systems is presented, which also shows the broad spectrum of fuel cell efficiencies.

Eq. (2.34) represents the electric energy only. If thermal discharge is also used by power-heat coupling, an efficiency of about 85% is possible.

---

[10]The reaction speed is defined as the fuel quantity in numbers of mol, which is consumed per second.
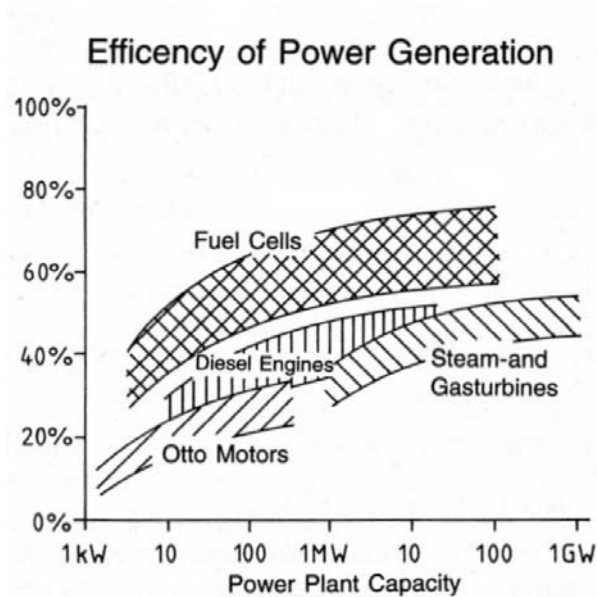
Figure 2.5: The efficiency of power generators varies as a function of the scale. The efficiency domain of the fuel cell is very broad, which is due to the large spectrum of fuel cell systems.[26]

2.5 Fuel cell types

There are many different types of fuel cells. The division between fuel cell types is done by the electrolyte, except for the direct methanol fuel cell, which is a special type of the proton exchange membrane fuel cell. This is meaningful, as the electrolyte determines which kind of ions are transported, which temperature range the fuel cell can be run in and which catalyst can be used. Each type of fuel cells has its own advantages and drawbacks. However one common reasons why they are not produced in series yet is, that all fuel cell types are too expensive, and therefore cannot compete with state of the art power generators.

2.5.1 Proton exchange membrane fuel cell (PEMFC)

The heart of the PEMFC is the proton conducting polymer membrane. For the time being fuel cells with Nafion membranes have the highest power density among the PEMFCs. Similar to Teflon, the Nafion membrane consists of polymer chains. While the Teflon polymers are linear chains of CF_2 monomers, the Nafion chain has additional sulphonal groups (SO_3H). If water is added to the polymer, the sulphonal groups dispense hydrogen ions. Hence the membrane becomes proton conductive when humidified. The electrodes are usually made of platinum-particle containing carbon-carriers. Either pure hydrogen or hydrogen from reformation processes is feed into the PEMFC. The cathode can be flooded by pure oxygen or by air. Since the PEMFC is a hydrogen/oxygen fuel

cell and the transported ion is the proton, the oxidizing of hydrogen at the anode and the oxygen reduction at the cathode are given by the reaction equations Eq. (2.2) and Eq. (2.3).

The PEMFC can produce high power densities of some hundred milliwatts per square centimeter. It has high mechanical stability and operating times of some ten thousand operating hours. As mentioned before, the electrochemical reaction only takes place at the three phase boundaries, and in the direct vicinity. Therefore all platinum particles are useless, which are not located at a three phase boundary. This leads to platinum usages being one order of magnitude higher than economically tolerable. Furthermore, the ion conductivity of the Nafion membrane depends on the humidification, which leads to a complicated water management. If the humidification is too low, the membrane drys out and the conductivity drops to zero. If the humidification is too high, the membrane erodes and the conductivity drops, too. In addition, the platinum catalyst is very sensible to carbon monoxide poisoning, as the CO molecule binds the active locations of the catalyst and occupy them for a long time.

2.5.2 Direct methanol fuel cell (DMFC)

As mentioned before, the DMFC is a modification of the PEMFC. The fuel cell design is equal to the design of the PEMFC, but the reactions are rather different. In contrast to the gaseous hydrogen in the PEMFC, the fuel in this type is feed in liquid form. It is a water-methanol mix. The methanol oxidation at the anode can be described by the following stoichiometric formula:

$$CH_3OH + H_2O \rightarrow CO_2 + 6H^+ + 6e^- \tag{2.35}$$
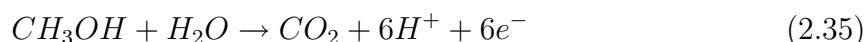
Since protons are transported across the membrane as well, the oxygen reduction is equal to Eq. (2.3).

Storing hydrogen is still a major issue, since the density is even under a pressure of 200 bar very low. Furthermore the hydrogen compression is a highly energy consuming process. But as the fuel is feed in liquid form into the DMFC, no gas tanks are required. Since methanol can be stored in liquid form under a pressure of 8 bar, only simple tanks are necessary. Therefore the peripheral systems of the DMFC are less complex and less expensive. Thus it is even possible to build very small fuel cell systems (e.g. as an energy source for cell phones). The water in the liquid fuel ensures the humidification of the membrane, thus no membrane dehydration occurs.

In spite of the advantages of the DMFC there are a lot of drawbacks. The reaction kinetics at the anode are slower than in the PEMFC. This leads to lower power densities and higher platinum loads. In fact the required platinum is by a factor of twenty higher than in a PEMFC. Furthermore CO_2 is produced in the electrochemical reaction, which needs to be removed from the anode to ensure high fuel concentration at the three phase boundaries. Thus a lower maximal current density due to concentration overpotential can be expected.

2.5.3 Alkaline fuel cell (AFC)

The electrolyte in the alkaline fuel cell is a liquid base. Mostly it is concentrated caustic potash (KOH). For low temperature applications ($60°C - 90°C$) the concentration is about 35-50 wt.-% . The AFC had been applied in the Apollo space shuttle program, using caustic potash concentrations of about 85 wt.-% at operating temperatures of about $250°C$[11]. In contrast to the acid based fuel cells, no protons are transported in the AFC but hydroxide ions. This leads to a water production at the anode and a water consumption at the cathode. The respective reactions are:

$$H_2 + 2OH^- \rightarrow 2H_2O + 2e^-, \quad \text{anode reaction} \tag{2.36}$$

$$\frac{1}{2}O_2 + H_2O + 2e^- \rightarrow 2OH^-, \quad \text{cathode reaction} \tag{2.37}$$
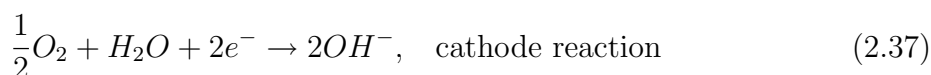
In virtue of the alkaline environment, the reaction kinetics are higher than in fuel cells with acidic electrolytes. Thus it is possible to achieve high current densities, and high efficiencies without the usage of platinum catalyst. Typical catalyst materials in the AFC are nickel and silver. Since these metals are much cheaper than platinum, it is more affordable than the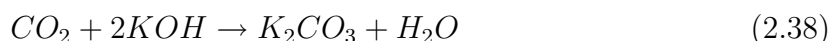 PEMFC. The circulating electrolyte facilitates the water and heat management, as both can be removed via the electrolyte loop.

Nevertheless the AFC has as well drawbacks. If caustic potash and carbon dioxide has contact, potassium carbonate is formed:

$$CO_2 + 2KOH \rightarrow K_2CO_3 + H_2O \tag{2.38}$$

In addition the following reaction takes place under carbon dioxide containing ambiance:

$$CO_2 + 2OH^- \rightarrow CO_3^{2-} + H_2O \tag{2.39}$$
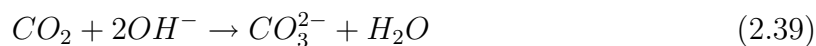
First, this leads to a dilution of the caustic potash, as the KOH is consumed. Secondly, the hydroxide ions are lost, which carry the ion current in the AFC. Thirdly, the carbonate molecules do not solve in water and thus deposit inter alia in the pores of the electrolyte confining membrane and clog them. Therefore the carbon dioxide needs to be removed from any participating gas flows. This can be accomplished by using pure oxygen or filtering carbon dioxide from air[12].

A derivative of the AFC is the **M**olten **C**arbonate **F**uel **C**ell (MCFC). The electrolyte is a molten salt consisting of alkali carbonates, which is conducting for carbon oxide ions CO_3^{2-}. Since alkali carbonates melt at higher temperatures, the operating temperature is above $600°C$. In the MCFC there are no problems regarding carbon dioxide. Of course the MCFC has its own problems concerning the high temperature and the molten salt electrolyte. This type of fuel cell will not be discussed here in detail.

---

[11]The Apollo alkaline fuel cell had an operating pressure of $200\,\text{bar}$ to prevent potash boiling.

[12]Carbon dioxide can be removed from the air by a soda lime filter, or by leading the air through old caustic potash.

2.5.4 Solid oxide fuel cell (SOFC)

The operating temperature of the solid oxide fuel cell is the highest of all fuel cell types. It is above 700°C, partly even above 1000°C. The electrolyte of the SOFC is an oxygen ion O^{2-} conducting solid oxide, mostly **Y**ttrium **S**tabilized **Z**irconium oxide (YSZ). The anode is a composite consisting of nickel and YSZ to increase the number of three phase boundaries, while the cathode consists of **L**anthanum **S**trontium **M**anganese (LSM). If hydrogen is feed into the SOFC the following reactions take place at the electrodes:

$$H_2 + O^{2-} \rightarrow H_2O + 2e^-, \quad \text{anode reaction} \tag{2.40}$$

$$\frac{1}{2}O_2 + 2e^- \rightarrow O^{2-}, \quad \text{cathode reaction} \tag{2.41}$$
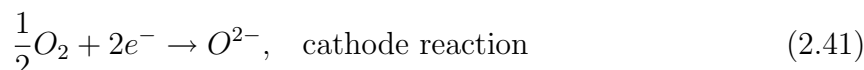
Though other fuel types, like natural gas, can be used in the SOFC.

The ion conductivity is based on crystal defects, whose number is greatly increased by yttrium doping. To jump from one crystal site to an empty one, the oxygen ion needs to overcome a potential wall. The energy needed to change the crystal site is called the activation energy, which is a material parameter. The jump rate is given by this activation energy, the applied electric field and the thermal energy. Since the electric field is given by the electrode potential and the activation energy by the material, the only free parameter to increase the jump rate is the temperature. Thus high temperatures are needed to ensure sufficient ion conductivity. Along with the high temperatures come advantages. As reaction kinetics are faster at higher temperatures, no noble catalyst is needed and the activation losses are minimal. Due to the solid oxide electrolyte neither poisoning nor pore clogging occurs and no water management is needed. Furthermore the SOFC has a good tolerance to overload, underload and short-circuiting.

Due to the high temperatures there are on the one hand the mentioned advantages, on the other hand there are also many disadvantages. Since the entropic losses are linear in temperature (c.f. Eq. (2.5)), both the OCV and the thermodynamic efficiency is lower than in other fuel cell types. However, the higher entropic losses can be used to maintain the high operating temperature. Furthermore expensive interconnector and casing materials are necessary. These are build of cermets (e.g. $LaCrO_3$) or iron/chrome alloys. To use interconnectors build of standard stainless steel, temperatures of approximately 600°C should not be exceeded, since the hardness of stainless steel drops considerably above this temperature. The mechanical properties of the SOFC materials are crucial. The thermal expansion coefficient of all materials must be sufficient low and as equal as possible among one another to prevent ruptures in the structure. Even SOFCs with thermal stable materials need about fifteen minutes to heat up, which makes the application of SOFCs in the automotive market very problematic for the time being.

By lowering the operating temperature under 600°C the interconnector material issue could be solved. Since the ion conductivity of YSZ at these temperatures is too low, it could no longer be used in such an intermediate temperature SOFC. Candidates for YSZ replacement are cerium oxide and gadolinium oxide. Although these materials have higher ionic conductivities at lower temperatures, the thermal stability is dubious.

Obviously, based on the information given in this chapter, it is a complicated task to satisfactorily operate fuel cells. The efficiency and lifetime depends on many parameters, of which only few are directly adjustable. The PEMFC and DMFC have a problematic water management, the AFC is very sensitive to carbon dioxide and the the SOFC operation includes a difficult heat management. These are only the major issues of the discussed fuel cells. Even if some problems are of minor importance in a single fuel cell, the situation becomes more complicated in a stack. The minor issues could rise to major ones in a stack, as they might accumulate. Therefore it is mandatory to find further diagnostic methods, which are applicable to stacks. In the following chapter the previous outlined diagnostic scheme is presented, which also leads to improved operation stability.

3 Diagnostics of fuel cell stacks

In this chapter the novel diagnostic scheme for fuel cell stacks is presented[34]. It permits to find damages occurring in a fuel cell of a stack not only without interfering with the fuel cell operation, but also greatly stabilizing the stack operation. First in section 3.1 a model is presented, which in spite of its simplicity contains all the ingredients of the phenomenon. This is an idealized model, which cannot even give assumptions about the applicability of this method. After clarifying the diagnostic scheme, more general statements are done in section 3.2. Although these statements are more general, they are embedded in an ideal model as well.

3.1 A simple model

Plates of very high conductivity (e.g. aluminum) are placed between all fuel cells of a stack (c.f. Fig. (3.1)). The plates have all the same number N_S of slits dividing the plates into $N_S + 1$ equal stripes. These stripes are not electrically isolated of each other. Instead they are connected at their ends in such a way that a transverse current can flow through the plate only by zigzagging through it touching the border of the plate at the locations s_i. At these locations the transverse currents can be measured, providing information about which particular fuel cell and which part of its MEA does not work correctly. The latter information can be obtained since adjacent plates are rotated by 90° and therefore its stripes are perpendicular to those of the previous and next plate. The determination of the location and intensity of the damage on the basis of the measured bridge currents is called the inverse problem.

An example may clarify the phenomenon further: Consider one plate of perfect conductivity m between two fuel cells M1 and M2 both having an effective MEA area A. Assuming a damaged area a with zero conductivity in the first fuel cell M1, the current density in the remaining undamaged area increases to:

$$j_d = \frac{I_0}{A - a}, \quad \text{where } I_0 \text{ is the total electric current} \tag{3.1}$$

As the resistance of plate m is assumed to be negligible, the normal component of the current density must be the same everywhere in the remaining fuel cell area of M1. The current across the stripe with the damaged area a is given by

$$i_d = j_d \cdot \left(\frac{A}{N_S + 1} - a \right) = \frac{A \cdot I_0}{(N_S + 1)(A - a)} - \frac{a \cdot I_0}{A - a} \tag{3.2}$$
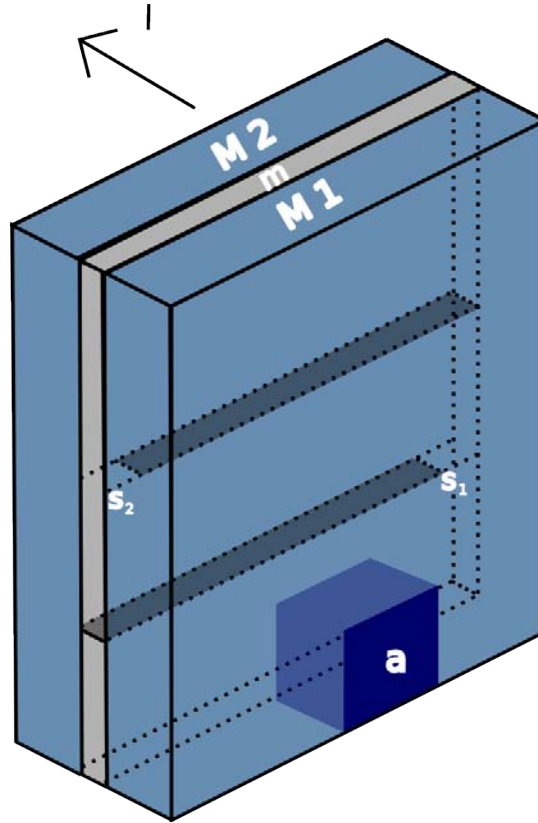
Figure 3.1: Schematic view showing a plate m of a material (e.g. aluminum) with very high conductivity. The plate is located between the fuel cells M1 and M2 and split into stripes (slits indicated by shaded areas). The main direction of the current is indicated by an arrow. It is assumed that the MEA of M1 has a damaged area a acting as an insulator. Because of the very high conductivity in m, the current density in each of the cells is practically constant - except in the area a where it is zero. Due to current conservation, transverse currents will rise in m flowing through the connections between the stripes at locations s_1 and s_2.

and the one across the undamaged stripes by:

$$i_{\mathrm{ud}} = \frac{A \cdot I_0}{(N_{\mathrm{S}} + 1)(A - a)} \tag{3.3}$$

Thus, the difference current

$$i_{\mathrm{diff}} = i_{\mathrm{ud}} - i_{\mathrm{d}} = \frac{a \cdot I_0}{A - a} \tag{3.4}$$

has now to be distributed over the remaining fuel cell area of M1. This requires a transverse compensation current and because of the slits, part of the current has to pass

damage Position	i_{s_1}	i_{s_2}	i_{s_1}/i_{s_2}
top	$-i_Q$	$-2 \cdot i_Q$	0.5
middle	$-i_Q$	i_Q	-1
bottom	$2 \cdot i_Q$	i_Q	2

Table 3.1: Currents at locations s_1 and s_2 for the ideal system with negligible resistance of the m plate.

the locations s_i. To obtain a homogeneous current density in M2 a compensation current of

$$i_Q = \frac{a \cdot I_0}{(N_S + 1) \cdot (A - a)} \tag{3.5}$$

has to flow from each intact stripe via the metal plate m to the defect one. If there are two slits in the plate m as shown in Fig. (3.1), two different currents are detected, one at s_1 and the other at s_2. If the damaged area is for example in the lower part of the MEA, the currents are

$$i_{s_1} = 2 \cdot i_Q \tag{3.6}$$

and

$$i_{s_2} = i_Q \tag{3.7}$$

with the definition:

$$i_Q = \frac{a \cdot I_0}{3 \cdot (A - a)} \tag{3.8}$$

As expected, the magnitude of the current at the location s_i changes with the size of the damaged area. If the damage occurs at another location, the relations between the currents change as well. The results for the three distinguishable damage locations are given in Tab. (3.1).

As can be seen from Tab. (3.1), in the case under consideration a unique relation between the position of a localized damage and the currents i_{s_1} and i_{s_2} exists. In fact, from the values it can be inferred how significant the damage is and in which stripe of the MEA (defined by the stripes of plate m) the damage has appeared. A corresponding analysis done at the previous plate m' (not shown in Fig. (3.1)) provides information in which stripe of M1 (this time defined by the plate m') the damage has occurred. Since the stripes of plate m' are perpendicular to the stripes of m, the combination of them divides the area of M1 into 9 rectangles and thus it can be inferred from the surface currents connecting the stripes in which of the 9 rectangles the damage is located and how big it is.

If the damage is not local but extended or if several local damages occur at the same time and not only at one fuel cell, the situation becomes much more complex.

Besides novel diagnostic possibilities, the additional plates have the effect of suppressing all inhomogeneous currents caused by a somehow erratic or not correctly working fuel cell. The inhomogeneities in the current density distribution are smoothed out at once, avoiding any peak currents at the damaged cell as well as at the adjacent cells.

vertical damage Position	horizontal damage position	i_1	i_2
top	left	$-i_Q$	$-i_Q$
bottom	left	i_Q	$-i_Q$
top	right	$-i_Q$	i_Q
bottom	right	i_Q	i_Q

Table 3.2: Currents at the bridges in the confining metal plates for the ideal system with negligible resistance of the m plate. The current i_Q is defined by Eq. (3.5) for $N_S = 1$.

Thus a much more stable and therefore a much more reliable operation of the fuel cell stack is predicted.

The simple model does not present estimates how well this scheme will work in reality. E.g. a competition between currents migrating through the graphite layers and those in the plates will take place and reduce the currents at the locations s_i. The simple model does not contain information how strong this effect is and whether or not currents at the locations are still measurable in practice in spite of this effect. A realistic answer to these questions requires detailed numerical computations. The numerical procedure as well as their results will be presented in chapter 5.

3.2 Generalization

In the previous section the diagnostic scheme has only been discussed for one metal plate with two slits. To describe the method in its full power and in its full complexity, the transition to arbitrary numbers of slits N_S in both metal plates confining a MEA has to be done. Furthermore the issue of the inverse problem needs to be addressed.

Since the slits in the MEA confining metal plates are perpendicular, a virtual segmentation of the MEA into

$$N_{\text{seg}} = (N_S + 1)^2 \tag{3.9}$$

segments is achieved. This segmentation is called virtual, since neither the MEA nor the flowfield plates are changed in any way. A segment is the smallest element a damage can be reduced to. Thus this virtual segmentation defines the resolution of the diagnostic method. The higher the number of slits, the higher is the resolution. Including both metal plates, the number of currents defining the state of one MEA is:

$$N_{\text{cur}} = 2 \cdot N_S \tag{3.10}$$

For the easiest case $N_S = 1$ there are four distinguishable defect locations, which are shown in Tab. (3.2).

3.2.1 The thin MEA approximation

[36]Ohm's law

$$\vec{j}(\vec{r}) = \sigma(\vec{r}) \cdot \vec{E}(\vec{r}) \tag{3.11}$$

describes the dependency of the current density on the electric field in electronic conductors. For currents carried by electrons in the graphite or metallic flowfield plates the electronic conductivity σ_{el} is in a very good approximation constant. Although the conductivity may change due to temperature variations, it is invariant to an alteration of the electric field. This does not hold inside of the MEA, as the current across it is carried by ions and catalytic processes take place at the electrodes. Even though the migration of ions is driven by the electric field, the resulting current depends in a complex, non linear way on the voltage drop.

One can circumvent this difficulty when investigating only the neighborhood of an operating point $(E_{\mathrm{OP}}, j_{\mathrm{OP}})$ by defining the quantity

$$\sigma_{\mathrm{lin}} = \frac{\partial j_{\mathrm{OP}}}{\partial E_{\mathrm{OP}}} \tag{3.12}$$

which has the dimension of a conductivity. Now it is possible to use

$$\vec{j}(\vec{r}) - \vec{j}_{\mathrm{OP}}(\vec{r}) = \sigma_{\mathrm{lin}} \cdot \left(\vec{E} - \vec{E}_{\mathrm{OP}} \right) \tag{3.13}$$

to calculate the deviation from the operating point. The disadvantage of this procedure is twofold: First, even an only locally malfunctioning MEA does not remain in the linear regime of the operation point. Secondly, σ_{lin} is a physically not elusive quantity for characterizing the processes taking place in the MEA.

To avoid all these problems the local normal current density j_n in the MEA is investigated. This quantity has a clear physical meaning: Catalyst and electrolyte degradation at a certain point lead to a reduction or even to a total inhibition of the normal current density j_n at just this location of the MEA.

This quantity is obtained in the following way:

Let $\vec{r}_{\mathrm{A}}$ be a location at the external anode surface as well as $\vec{r_C}$ the equivalent point at the external cathode surface. Furthermore $j_n(\vec{r}_{\mathrm{A}})$ is the current entering the MEA at the location $\vec{r}_{\mathrm{A}}$. Due to the very low mobility of the ions in the electrolyte, most of the ions will migrate straight through it. Since the transverse currents in the catalyst layers should also be comparatively small[1] one obtains as a very good approximation:

$$j_{\mathrm{MEA}}(\vec{r}) \approx j_n(\vec{r}_{\mathrm{A}}) \approx j_n(\vec{r}_{\mathrm{C}}) \tag{3.14}$$

The local current density j_{MEA} gives a direct information about the state of the MEA at each location. Furthermore it defines in a unique way the boundary conditions for the regions outside the MEA, in which the Ohm's law can be applied. Of course this approximation Eq. (3.14) works best if the MEA is very thin. Due to that, it is called the "thin MEA approximation".

---

[1] There may exist layers, still within the MEA but outside of electrolyte and catalysts, having a possibly non negligible transverse conductivity. For simplicity this refinement is not considered. In principle there is no reason not to take those layers into account because there the conductivity is a property of the material.

3.2.2 Linear transformation

In the previous subsection it has been shown that the transverse MEA conductivity is very low, particularly in comparison to the aluminum plates, which are parallel to it. Thus the local normal currents do not change while passing through the MEA. Therefore it is meaningful to use the MEA current density as a direct representation of the MEA state. Reconstructing the MEA current density on the basis of the bridge currents is the purport of the diagnostic method. Since no structures smaller than one segment can be resolved, the inverse problem is the reconstruction of the integrated current across each segment in the MEA.

Prior to the reconstruction is the forward problem, which is the assembling of the linear transformation matrix $\mathcal{A}$, described by

$$\mathcal{A} \cdot \vec{i}_{\mathrm{seg}} = \vec{i}_{\mathrm{S}} \tag{3.15}$$

with the N_{seg} dimensional vector $\vec{i}_{\mathrm{seg}}$, which contains the integrated currents across each segment. $\vec{i}_{\mathrm{S}}$ is the N_{cur} dimensional vector containing the bridge currents in the confining metal plates. Now the linear transformation is separated into a matrix $\tilde{\mathcal{A}}$ depending only on the slit number and a matrix $\mathcal{B}$ containing all transformation parameters:

$$\mathcal{A} = \tilde{\mathcal{A}}(N_{\mathrm{S}}) \cdot \mathcal{B} \tag{3.16}$$

$\tilde{\mathcal{A}}(N_{\mathrm{S}})$ can be derived from the data given in Tab. (3.1) and Tab. (3.2). For $N_{\mathrm{S}} = 1$, it has the following form:

$$\tilde{\mathcal{A}}(1) = \frac{1}{2} \begin{pmatrix} -1 & 1 & -1 & 1 \\ -1 & -1 & 1 & 1 \end{pmatrix} \tag{3.17}$$

For arbitrary slit numbers, the linear transformation matrix can be constructed in the following way:

$$\tilde{\mathcal{A}}^T(N_{\mathrm{S}}) := \frac{1}{N_{\mathrm{S}}+1} \begin{pmatrix} \vec{u}_{h|1} & \dots & \vec{u}_{h|N_{\mathrm{S}}} & \vec{u}_{v|1} & \dots & \vec{u}_{v|N_{\mathrm{S}}} \end{pmatrix} \tag{3.18}$$

The column vectors $\vec{u}_{h|n}$ represents the horizontal slitted metal plate given by

$$\vec{u}_{h|n} = \begin{pmatrix} k\text{-times} \begin{cases} n\text{-times} & \{-(k-n) \\ (k-n)\text{-times} & \{n \end{cases} \end{pmatrix} \tag{3.19}$$

with the number of stripes $k = N_S + 1$. Analogously the column vectors $\vec{u}_{v|n}$ represent the vertical slitted metal plate:

$$\vec{u}_{v|n} = \begin{pmatrix} (n \cdot k)\text{-times} & \{k-n \\ k(k-n)\text{-times} & \{-n \end{pmatrix} \tag{3.20}$$
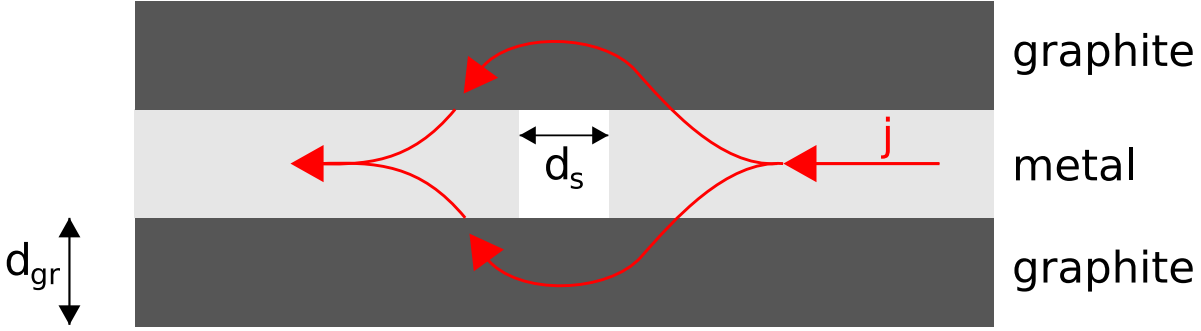
Figure 3.2: Cross section of the slitted metal plate showing the parasitic currents through the bypass in the graphite layers. The compensation current in this metal plate flows from the right side to the left side, whereas the intended current path would be via a bridge in the metal plate (not shown).

$\mathcal{B}$ is a diagonal matrix

$$\mathcal{B} = \begin{pmatrix} \beta_1 & 0 & 0 & 0 \\ 0 & \beta_2 & 0 & 0 \\ 0 & 0 & \ddots & 0 \\ 0 & 0 & 0 & \beta_{N_{seg}} \end{pmatrix} \tag{3.21}$$

with the diagonal elements β, which are functions of the total electric current I_0, the damage area a and the total fuel cell area A:

$$\beta = \beta(I_0, a, A) \tag{3.22}$$

Each diagonal element is the proportionality factor for one segment current. These can be equal for all segment currents.

3.3 Approximation of current losses

As mentioned before, the ideal model can give only the idea of the diagnostic method. Even though numerical calculations are required to determine if the currents at the bridges s_i are large enough to be measured, some statements concerning parasitic currents can be done.

Before that some details about the calculated fuel cell are needed. A PEMFC with graphite flowfield plates with a cross section of about 200mm × 180mm is the fuel cell of choice. All layers (i.e. MEA, graphite flowfield and metal plate) have a thickness of 1mm. The slitted metal plates are fabricated of aluminum, which has an electric conductivity of $\sigma_{\text{Al}} = 4 \cdot 10^7 \, \text{S} \cdot \text{m}^{-1}$.

There are two effects, which could lead to parasitic currents and therefore decrease the measurable current at the bridges.

- The first effect is the circulation of the current through the graphite flowfields

(c.f. Fig. (3.2)). The magnitude of current taking this bypass is given by the slit dimensions and graphite conductivity. To estimate the order of current lost due to this effect, the resistance of the bypass R_{bp} is approximated by:

$$R_{bp} = \frac{l}{2 \cdot d_{\mathrm{gr}} \cdot L_{\mathrm{stripe}} \cdot \sigma_{\mathrm{gr}}} \qquad (3.23)$$

Here d_{gr} denotes the thickness of the graphite layer and L_{stripe} the length of the stripe, therefore the product $d_{\mathrm{gr}} \cdot L_{\mathrm{stripe}}$ is the cross section of the bypass. Furthermore $\sigma_{gr} = 4200\,S \cdot m^{-1}$ is the conductivity of the graphite and l the length of the bypass, which is further approximated by $l = 3 \cdot d_{\mathrm{S}}$, with the slit width d_{S}. Since the metal plate is embedded in two graphite layers, there are two equal bypasses. The parallel circuit of two equal resistances leads to a total resistance, which is the half of a single resistance. If $d_{\mathrm{S}} = d_{\mathrm{gr}} = 10^{-3}\,\mathrm{m}$ and $L_{\mathrm{stripe}} = 0.18\,\mathrm{m}$, the bypass resistance is:

$$R_{\mathrm{bp}} = \frac{3 \cdot 10^{-3}\,\mathrm{m}}{2 \cdot 10^{-3}\,\mathrm{m} \cdot 0.18\,\mathrm{m} \cdot 4200\,\mathrm{S} \cdot \mathrm{m}^{-1}} \approx 2 \cdot 10^{-3}\,\Omega \qquad (3.24)$$

A more sophisticated approximation, which also include the normal resistance of the graphite layer is given in the appendix A.4.

- The second effect appears due to finite metal conductivity and a not vanishing MEA conductivity. In the ideal model the MEA acts like a perfect electric dam, so the current density leaving the metal plate is totally homogeneous. Though in a real fuel cell the dam effect is not perfect and the current density may not be completely homogeneous. Thus a fraction of the current may drain away before it passes the bridges. The resistance R_{d} the draining current needs to overcome is also approximated for one stripe. This resistance represents the severity of this effect:

$$R_{\mathrm{d}} = \frac{d_{\mathrm{MEA}}}{A_{\mathrm{stripe}} \cdot \sigma_{\mathrm{MEA}}} \qquad (3.25)$$

As mentioned before, the conductivity of the MEA σ_{MEA} is an opaque quantity, which depends on many parameters. However, for calculations in which the exact value is of no concern, an approximated conductivity at an operating point can be used (c.f. subsection 2.3.4). At a given current density, there is an internal voltage drop due to the various effects of overpotentials described in the second chapter. Altogether, the current density and the voltage drop define the approximated conductivity for a given MEA thickness. Here, the MEA thickness is set to $d_{\mathrm{MEA}} = 1 \cdot 10^{-3}\,\mathrm{m}$, for which a current density of $j = 166.6\,\mathrm{mA} \cdot \mathrm{cm}^{-1}$ and an internal voltage drop of $\eta = 0.3\,\mathrm{V}$ lead to a MEA conductivity of:

$$\sigma_{\mathrm{MEA}} = \frac{d_{\mathrm{MEA}} \cdot j}{\eta} = \frac{1 \cdot 10^{-3}\mathrm{m} \cdot 1666\,\mathrm{A} \cdot \mathrm{m}^{-2}}{0.3\,\mathrm{V}} = 5.5\frac{\mathrm{S}}{\mathrm{m}} \qquad (3.26)$$

With this MEA conductivity and a stripe area of $A_{\mathrm{stripe}} = 0.0666\,\mathrm{m} \cdot 0.18\mathrm{m} =$

$1.2 \cdot 10^{-2} \, \mathrm{m}^2$, the resistance of the drain effect is about:

$$R_{\mathrm{d}} \approx 1.5 \cdot 10^{-2} \Omega \tag{3.27}$$

The comparison between these two effects shows that the bypass through the flowfield plate is the more severe one, as the resistance is by an order of magnitude smaller than the drain effect. These approximations still do not reveal whether the diagnostic method is applicable or not. Nevertheless, it is possible to give a statement concerning the bridge resistances: Since the resistance of the metal plate can still be neglected in comparison to these effects, the bridge resistance may be as large as R_{bp} to measure half of the ideal current.

Now it is obvious, that parallel current paths are present in the fuel cell, which lead to parasitic currents. To calculate the remaining bridge currents accurately, detailed computations including the fuel cell geometry and material parameters are needed. This problem is solved by the application of the finite-volume method to the diagnostic scheme. This three dimensional grid method is introduced in the following chapter and applied in the fifth one. Since the number of segment currents increases quadratically with the slit number, but the number of measurable bridge currents increases only linearly, the null space of the inverse calculation rises quadratically, too. Therefore many segment current configurations lead to the same bridge currents, though many of these are connected with unphysical defect structures. To find probable segment current configurations amongst all possible ones, a variant of the simulated annealing method is employed, by which solutions may be distinguished by their defect structure. This method is also introduced in the following chapter and applied in the sixth one.

4 Numerical methods

In this chapter the numerical methods used in this work are described. First the finite-volume method is discussed. It permits to solve boundary value problems of arbitrary system designs on a grid. In engineering it is usually employed to solve the Navier-Stokes-Equation simulating aerodynamic or hydrodynamic problems. It is also applicable to electrostatic and magnetostatic problems, as well as to electrodynamic and magnetodynamic problems. In contrast to other grid methods, like finite element or finite difference methods, it is possible to show the observance of all Maxwell equations in its discretization.

Secondly the simulated annealing method is described, which is a generic statistical optimization algorithm for the determination of a global minimum between local ones. This method has an analogy in nature, since it has been copied from the crystallization of liquids.

4.1 Finite-Volume method for electrostatic boundary value problems

4.1.1 Basics

Current conservation   In an enclosed electrical system the continuum equation

$$div\,\vec{j} + \frac{\partial \rho}{\partial t} = 0 \tag{4.1}$$

has to hold. For the stationary case this reduces to the current conservation:

$$div\,\vec{j} = 0 \tag{4.2}$$

Following the local Ohm's law

$$\vec{j} = \sigma \cdot \vec{E} \tag{4.3}$$

the current density $\vec{j}$ can be replaced by the product of the conductivity tensor σ and the electric field $\vec{E}$:

$$div\,(\sigma \cdot \vec{E}) = 0 \tag{4.4}$$

As the electric field is given by the negative gradient of the electric potential ϕ, the latter equation is transferred to the following differential equation:

$$-div\,(\sigma \cdot grad\,\phi) = 0 \qquad\qquad (4.5)$$

This is a second-order elliptic partial differential equation for the potential. To obtain the potential distribution across a body Ω for given boundary conditions, Eq. (4.5) has to be solved at every location of Ω. Thus, if Ω is a macroscopic object, a three dimensional boundary value problem has to be solved. In the static case the potential $\phi(\vec{x})$ is fully determined by the boundary conditions. Since the current density distribution $\vec{j}(\vec{x})$ can be derived from the potential and the conductivity, it is as well fully defined by the boundary conditions.

Boundary conditions   There are various possibilities to define the boundary conditions of a system. The most important and most used boundary conditions are the Neumann boundary condition and the Dirichlet boundary condition.

Neumann boundary condition: The potential derivative at the Neumann boundary Γ_n is fixed, in an electrostatic system this is the normal current density $\vec{j}_n$.

$$\sigma\frac{\partial\phi}{\partial\vec{n}}(\vec{r}) = -\vec{j}_n(\vec{r}), \;\; \vec{r}\epsilon\Gamma_n \qquad\qquad (4.6)$$

Dirichlet boundary condition: The potential at the Dirichlet boundary Γ_d is fixed.

$$\phi(\vec{r}) = \phi_d(\vec{r}), \;\; \vec{r}\epsilon\Gamma_d \qquad\qquad (4.7)$$

Gauss integral theorem   The basic tool of the finite-volume method is the Gauss integral theorem. It connects the n-dimensional integration of the divergence of a vector field over a volume with the $(n-1)$-dimensional integration of the vector field itself. In the three dimensional case the Gauss integral theorem transforms a volume integration into a surface integration. If the magnetic field is calculated by the finite-volume method, the Stokes integral theorem is required, too (c.f. appendix A.2).

Gauss integral theorem: The integral of the divergence of the vectorial current density $\vec{j}$ over an enclosed volume V with a partial continuously differentiable boundary ∂V is equal to the integration of the normal current density components $\vec{j} \cdot \vec{n}$ over the surface, with the normal vector of the surface $\vec{n}$.

$$\int_\Omega div\,\vec{j}\,dV = \int_{\partial\Omega} \vec{j} \cdot \vec{n}\,dA \tag{4.8}$$

4.1.2 Discretization of the potential

To obtain the current distribution in a body Ω for a given boundary condition, the differential equation Eq. (4.5) has to be solved at each point of Ω. Therefore Ω is segmented into small cells $\omega_{\mu\nu}$, which cover Ω completely. In the simplest way this grid is constructed of cuboids. In this case it is easy to calculate the surface currents and cover Ω consistently. Thus adjacent cells always share entire surfaces, so it can not happen that one side of a cell is in contact with two different cells. It is possible to change the size of the cuboids layer by layer[1], but it is mandatory, that all cells of one layer have the same width, to prevent the described overlap of multiple faces. The potential is defined in the center of the cells, while the currents are defined on the surfaces. Fig. (4.1) shows a simple example of a grid, which fulfills all requirements. For the sake of simplicity the following derivation of the finite-volume algorithm is done in two dimensions, but it can effortlessly be extended to three dimensions.

For the cell $\omega_{\mu\nu}$ (c.f. Fig. (4.1)) the differential equation Eq. (4.5) is discretized. First of all the Gauss integral theorem is applied to transform the surface integral to a line integral (in 3D respectively the volume integral to a surface integral):

$$\int_{\omega_{\mu\nu}} div\,(\sigma \cdot grad\,\phi)dA = \int_{\partial\omega_{\mu\nu}} \sigma \cdot grad\,\phi \cdot \vec{n}\,ds \tag{4.9}$$

This reduces the computing time vastly[2]. The closed line integral is separated into four individual line integrals (3D: into six individual surface integrals):

$$\int_{\partial\omega_{\mu\nu}} \sigma \cdot grad\,\phi \cdot \vec{n}\,ds = \int_{\partial\omega_L} \sigma \frac{\partial\phi}{\partial x}dy - \int_{\partial\omega_R} \sigma \frac{\partial\phi}{\partial x}dy + \int_{\partial\omega_B} \sigma \frac{\partial\phi}{\partial y}dx - \int_{\partial\omega_T} \sigma \frac{\partial\phi}{\partial y}dx \tag{4.10}$$

Here the index of $\partial\omega$ denotes the individual sides of the cell (**T**op, **B**ottom, **L**eft and **R**ight). The signs are chosen with respect to the direction of the surface normal vectors.

---

[1] For example a z-layer consists of all cells with the same z-coordinate. The cuboid size in z-direction h_z can change from one z-layer to the next. Since the same holds for x- and y-layers, the contact surface of adjacent cells cannot differ.

[2] The computing time for a volume integration has a cubic dependency on the system size $\propto N^3$ (N is the number of cells). The reduction to a surface integral leads to a quadratic dependency. In two dimensions the application leads to a linear dependency.
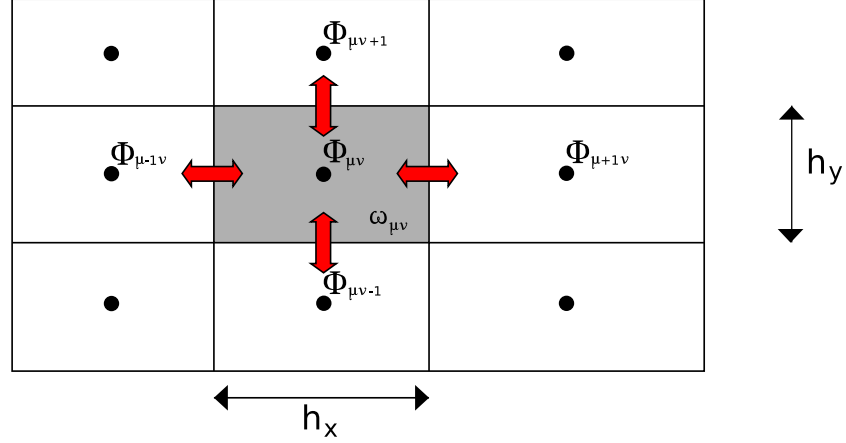
Figure 4.1: This picture shows an exemplary discretization of the two dimensional body Ω. The black dots represents the location of the potential. For the central cell the current density locations are indicated by the red arrows.

In this way all positive currents enter the cell through the bottom and left side. Eq. (4.10) is an exact representation of the differential equation Eq. (4.5) for the cell $\omega_{\mu,\nu}$.

Canonical approximations To calculate Eq. (4.10) numerically some approximations have to be introduced. As the potential is discretized in the center of the cells, it is obvious to approximate the derivative by the difference quotient. Assuming a constant potential on each individual side of the cell, it is possible to calculate the integrals in Eq. (4.10) easily:

$$
\begin{aligned}
\int_{\partial\omega_{\mathrm{L}}} \sigma \frac{\partial\phi}{\partial x} dy &\approx \sigma_{\mu-1/2,\nu} \frac{\phi_{\mu,\nu} - \phi_{\mu-1,\nu}}{h_{x|\mu-1/2,\nu}} h_y \\
\int_{\partial\omega_{\mathrm{R}}} \sigma \frac{\partial\phi}{\partial x} dy &\approx \sigma_{\mu+1/2,\nu} \frac{\phi_{\mu+1,\nu} - \phi_{\mu,\nu}}{h_{x|\mu+1/2,\nu}} h_y \\
\int_{\partial\omega_{\mathrm{B}}} \sigma \frac{\partial\phi}{\partial y} dx &\approx \sigma_{\mu,\nu-1/2} \frac{\phi_{\mu,\nu} - \phi_{\mu,\nu-1}}{h_{y|\mu,\nu-1/2}} h_x \\
\int_{\partial\omega_{\mathrm{T}}} \sigma \frac{\partial\phi}{\partial y} dx &\approx \sigma_{\mu,\nu+1/2} \frac{\phi_{\mu,\nu+1} - \phi_{\mu,\nu}}{h_{y|\mu,\nu+1/2}} h_x
\end{aligned}
\tag{4.11}
$$

Here $h_{x|\mu-1/2,\nu}$ is the distance between the center of $\omega_{\mu,\nu}$ and $\omega_{\mu-1,\nu}$. These approximations are called canonical approximation. Since the current density is defined at the face center of the cells, the conductivities has to be defined at this point as well.

4.1.3 Conductivity

As can be seen from Eq. (4.11) the conductivity σ depends on the location. At each cell side the derivative in only one direction is calculated. Therefore the conductivity
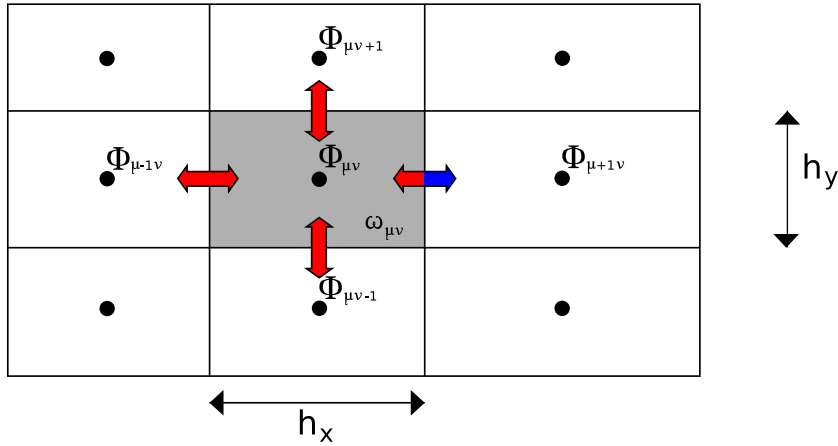
Figure 4.2: The colors of the arrows denote the conductivities at the boundaries of $\omega_{\mu,\nu}$. The bi-colored arrow expresses different conductivities of two adjacent cells in the same direction.

also depends on the direction and can thus be given by a diagonal tensor. As the material properties of Ω should not change within a cell, it is convenient to define the conductivity for whole cells. Although the material parameters do not change within a cell, they can be anisotropic. The conductivity of a single central cell is shown in Fig. (4.2). A problem occurs if two adjacent cells are of different material, and by that have different conductivities in the same direction. On first sight it is not decided which conductivity has to be used for the calculation of the current density between these two cells. Nevertheless it is possible to define the conductivity of a material interface at the boundary between two cells, by using the harmonic mean value of both conductivities. For two cells of the same size this is given by:

$$\sigma_{\mathrm{h}} = 2 \left(\frac{1}{\sigma_1} + \frac{1}{\sigma_2} \right)^{-1} \tag{4.12}$$

A derivation and a discussion of the conductivity at material boundaries is given in the appendix A.1.

4.1.4 Discretized boundary conditions

Neumann boundary conditions The gradient is calculated between every two adjacent potential locations, which are inside of Ω. These current densities are identified as $\vec{j}_{\mathrm{G}}$ (c.f. Fig. (4.3)). The current densities at the boundary of Ω are predefined as $\vec{j}_0$. Most of the boundary current vector $\vec{j}_0$ components are typically zero. Only the source and the drain locations have non zero components. Using Neumann boundary conditions the
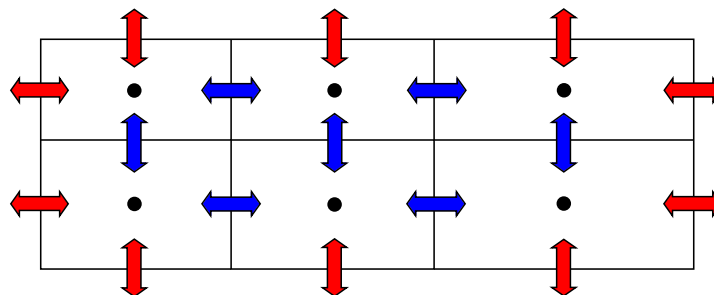
Figure 4.3: In the case of Neumann boundary conditions, the current density at the boundary of Ω is predefined. The blue arrows indicate the gradient current densities $\vec{j}_\mathrm{G}$ between the potentials of each adjacent cell. The red arrows indicate the predefined boundary current densities $\vec{j}_0$.

current conservations has the following form:

$$div(\vec{j}_\mathrm{G} + \vec{j}_0) = 0 \tag{4.13}$$

For all cells, which are not connected to a source or drain, this transfers to Eq. (4.2). In cells connected to a source or a drain, the sum over the gradient currents must be equal to the negative boundary value predefined for this cell. Using only Neumann boundary conditions does not lead to a unique solution, since the current density distribution is invariant to a global homogeneous change in the potential. Therefore the potential needs to be fixed at least at one location to obtain a unique solution. Furthermore it is possible to use both boundary conditions in the same body (at different boundaries) to avoid this issue.

Dirichlet boundary conditions   In the case of Dirichlet boundary conditions the potential on the boundary of Ω is predefined and the gradient is calculated on each surface of each cell (c.f. Fig. (4.4)). To calculate the gradient on the boundary, potentials on virtual points on the outside of Ω, the so called ghost points, are needed. To determine the ghost point potential, it is assumed, that the virtual cell is of the same size and has the the same conductivity as the adjacent inner cell. In addition a linear potential progression across the boundary is assumed. Due to the linearity of the potential (c.f. appendix A.1) it is possible to use

$$\phi(x_2) = \phi(x_0) - (x_0 - x_2) \cdot E_2 \tag{4.14}$$

for the external cell. As the conductivity in both cells is consistent, the electric field is equal as well. Thus, the electric field E_2 can be substituted by the canonical approximation of E_1:

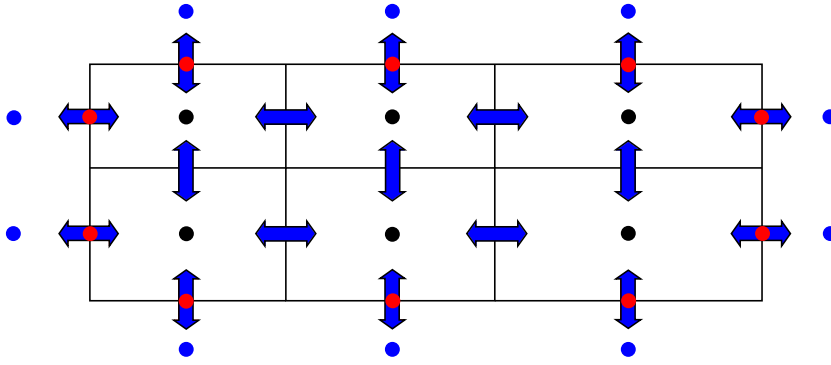$$\phi(x_2) = \phi(x_0) - \frac{x_0 - x_2}{x_0 - x_1}(\phi(x_0) - \phi(x_1)) \tag{4.15}$$

Figure 4.4: In the case of Dirichlet boundary conditions the potential at the boundary of Ω is predefined. The blue arrows indicate the gradient current densities $\vec{j}_{\mathrm{G}}$. The blue dots x_2 indicate the ghost points, the black ones x_1 the potential in the surface cells of Ω and the red ones x_0 the predefined potential at the boundary.

Both cells are of the same size, so $x_2 - x_0$ is equal to $x_0 - x_1$, which leads to the linear approximation of the ghost point potential $\phi(x_2)$:

$$\phi(x_2) = 2 \cdot \phi(x_0) - \phi(x_1) \tag{4.16}$$

4.1.5 Discretized differential equation

To solve the electrostatic boundary problem for Ω, the differential equation has to be solved for each cell $\omega_{\mu\nu}$. Let n_{j} be the total number of current density points, and n_ϕ be the total number of potential points in Ω for a given grid, then we define:

- the $n_{\mathrm{j}} \times n_\phi$ dimensional matrix $\mathcal{G}$, which contains the canonical approximations of the gradient.

- the diagonal $n_{\mathrm{j}} \times n_{\mathrm{j}}$ matrix $\mathcal{S}$, which contains the conductivities of all current density locations.

- the $n_\phi \times n_{\mathrm{j}}$ dimensional matrix $\mathcal{D}$, which contains the sum over all surface currents for each cell.

Thus, for Neumann boundary conditions the discretized differential equation becomes:

$$\mathcal{D} \cdot \mathcal{S} \cdot \mathcal{G} \cdot \vec{\phi} = \mathcal{D} \cdot \vec{j}_0 \tag{4.17}$$

This matrix differential equation can be written as

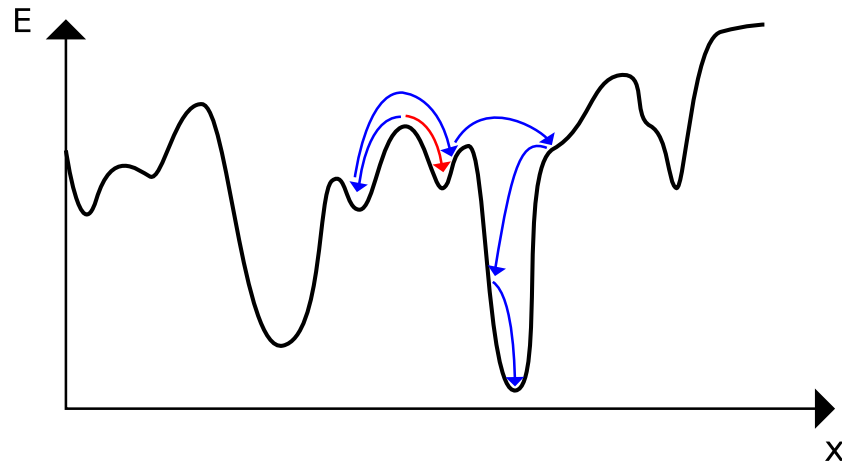$$\mathcal{B}\vec{\phi} = \vec{b} \tag{4.18}$$

Figure 4.5: Schematic plot of an energy function E in dependency of one variable x. Beginning from the same initial position the direct method (red arrow) gets stuck in the first local minimum, whereas the simulated annealing algorithm finds the global minimum following a random walk (blue arrows).

where $\mathcal{B} = \mathcal{D} \cdot \mathcal{S} \cdot \mathcal{G}$ is a non singular $n_\phi \times n_\phi$ dimensional matrix and $\vec{b} = \mathcal{D}\vec{j}_0$ is a n_ϕ dimensional vector, which contains the inhomogeneity (boundary conditions) of the problem. Eq. (4.18) is a usual algebraic equation, which can be solved with standard numerical techniques.

It is also possible to assemble a differential equation for the magnetic field in the finite-volume discretization, which is presented in the appendix A.2. As mentioned before all Maxwell equations are fulfilled in the finite-volume method. This is shown in appendix A.3

4.2 Simulated annealing method

The method of simulated annealing is a generic statistical optimization algorithm. It surpasses direct methods (e.g. *steepest descent* and *conjugate gradient*) for problems, in which the global minimum is hidden amongst many local minima. The direct methods find the closest local minimum to the initial point, whereas the simulated annealing method can overcome local minima to find the global one (c.f. Fig. (4.5)). This algorithm has been developed to find optimal layouts of complex integrated circuits in micro chips. Furthermore it is possible to solve the famous traveling salesman problem, which is a NP-complete[3] problem. These two examples are both discrete combinatorial problems, but it is also possible to solve continuous problem.

It should be mentioned, that the simulated annealing technique is not completely artificial, in fact it is copied from nature. If a liquid is cooled down and eventually

---

[3]*non polynomial*: The complexity of the problem increases exponential with its size.

condensate, the final structure in the solid body depends on the cooling speed. If the liquid is cooled down rapidly, polycrystalline or amorphous structures are formed. On the contrary, if the liquid is slowly annealed, monocrystalline structures form. In a rapid temperature drop there is not enough time for the atoms or molecules to form the optimal structure, as their mobility decreases too fast. In a slow, adiabatic, temperature drop, the gradual decrease of the particle mobility leads to a continuous reconfiguration of the structure. Therefore a more stable fabric is obtained. The total energy of an amorphous structure is higher than that of a monocrystalline one. Therefore the rapidly cooled system is stuck in a local energy minimum, whereas the gradual annealed system reached the global one. This principle is transferred to a numerical algorithm, which can be applied to any optimization problem. Although it is often possible to find a representative minimum, in most of the problems it is not possible to check if it is the *global* one.

In addition to the mentioned benefits of this technique, it is possible to use it as a *black box* if no deeper knowledge about the problem is present. As long as an energy function[4] is known, a representative minimum can be found (at least in principle; the computer power is always a limiting factor). If additional information is known, it can be implemented either directly into the energy function or as a constraint into the algorithm. In spite of the wide applicability, the algorithm is quite easy to implement.

The heart of the simulated annealing method is the evaluation of transition rates between configurations $\pi_{n \to n+1}$. In the majority of cases this is done by the metropolis algorithm. In nature the Boltzmann distribution $\propto exp(-\beta \cdot \Delta E)$ [5] determines whether a change to an unfavorable configuration is done or not. This is adapted to the metropolis algorithm. Since downhill steps should always be accepted, the transition rate for the metropolis step is given in the following form:

$$\pi_{n \to n+1} = \begin{cases} e^{-\beta \cdot \Delta E} & \text{, for } \Delta E < 0 \\ 1 & \text{, otherwise} \end{cases} \tag{4.19}$$

Using the metropolis algorithm, it is possible to overcome local minima of a depth $\Delta E_{\min} < 1/\beta$.

The simulated annealing algorithm for continuous variables

1. Initialization of the variables $\{x\}$: This can be done randomly. This represents high temperatures, as in this case all configurations have the same probability. If there is an initial guess for the optimum, it can be used as the starting configuration. However, initial guesses has to be treated with care, as intuition can fail and may lead to a deep local minimum only. The random initialization could lead to

---

[4]It does not need to be a real energy function, it can be a cost function or a general Lagrangian as well.

[5]ΔE is the energy difference, $\beta = (k_B T)^{-1}$ is the inverse temperature with the Boltzmann constant k_B and the systems temperature T.

a better result. Furthermore the initial temperature has to be defined. For thermodynamical systems this can be done straightforward with the real temperature. For other systems the temperature parameter β has to be defined in such a way, that a specific fraction of the uphill steps is accepted.

2. Variable shift: One variable $x_{\nu|n}$ is shifted by a random value $x_{\nu|n+1} = x_{\nu|n} + \Delta x_i$. The choice of the random walk evoke discussions in the literature, as in certain situations (like the walk through a narrow valley) a simple random number generator proposes to many uphill steps. The use of the *downhill simplex* method could be advantageous in such a situation.

3. Metropolis step: The total energy of the new configuration E_{n+1} is calculated and the transition rate $\pi_{n \to n+1}$ is determined by Eq. (4.19) with $\Delta E = E_{n+1} - E_n$. At this point it is possible to implement constraints. This is done by overriding the transition rate manually to zero, if the new configuration violates a constraint.

4. Monte Carlo step: Repeat 2. and 3. for each variable $\{x\}$. In reference to the Monte Carlo simulation, the variable shift proposal in addition to the evaluation of this proposal for all variables is called Monte Carlo step (MCS).

5. Temperature change: After repeating point 4 N_{MCS} times, the temperature is lowered $T \to T - dT$ or $\beta \to \beta + d\beta$ respectively. As the lowering of temperature comes along with a lower uphill step acceptance rate, it is meaningful to lower the maximal variable shift Δx_{max} by a factor ξ, with $\Delta x_{T-dT} = \xi \cdot \Delta x_T$ and $\xi \leq 1$, to prevent an algorithm deadlock.

6. Break condition: Various break conditions can be chosen. One possible condition is the convergence of energy.

As can be seen a number of numerical parameters has to be set prior to the executing of the algorithm:

- The initial variable shift Δx_{init}

- Change of variable shift ξ

- Initial temperature parameter β

- Temperature change rate dT or $d\beta$ (reciprocal)

- Number of Monte Carlo steps per temperature step N_{MCS}

- A generic break condition

5 The forward problem

In this chapter, the forward problem is discussed. First, detailed numerical calculations regarding the slit currents and their results are presented. These show if the simple idea, presented in chapter 3, is applicable to a real fuel cell. Furthermore the results show how much current is lost by circulating the slits via flowfield plates and in which magnitude the slit current can be expected for different types of flowfield plates. Thereafter follows an assessment of the operation stabilizing effect of the metal plates. Therefore further detailed numerical calculations are done on the basis of the finite-volume method. The third part of this chapter deals with the numerical assembly of the linear transformation matrix $\mathcal{A}$. Since the computation of $\mathcal{A}$ becomes very expensive for larger numers of slits per aluminum plate, the calculation arrangement is reduced to the most necessary parts, which are discussed in this part of the chapter.

5.1 Numerical investigation of the bridge currents

To investigate the currents at the bridges only one slitted metal plate is needed. Although a second metal plate is needed to distinguish the defect location, it yields no further information about the magnitude of the bridge currents. Therefore only one double slitted metal plate is used in the calculation (c.f. Fig. (5.1)). In front of the first metal plate and behind the last one, homogeneous Neumann boundary conditions are defined in such a way, that the total electric current is $60\,\mathrm{A}$. This is obtained by boundary current densities of about $j_N = 1666\,\mathrm{A} \cdot \mathrm{m}^{-2}$. Since inhomogeneities in the MEAs could affect further fuel cells in the stack, the current density in the MEAs is decoupled from the boundary conditions by the addition of unslitted metal plates in front of the arrangement and behind it. Without the additional metal plates, the boundary conditions would enforce an unphysical homogeneous current density in the MEA causing an unwanted change in the bridge currents. To obtain the currents at the locations s_1 and s_2, in dependency of the flowfield material and the damage in the MEA M1, the potential distribution is calculated in the finite-volume method. Therefore Fig. (5.1) is separated in conformity to the finite-volume prerequisites.

5.1.1 Finite-volume grid

The FV-cell[1] size in Y-direction (the stack direction) is constant. Due to the harmonic averaging of the conductivities, no errors are introduced at material interfaces. Therefore

---

[1]The elemental separation of the finite-volume discretization (FV-cell) should not be mistaken for the fuel cell.
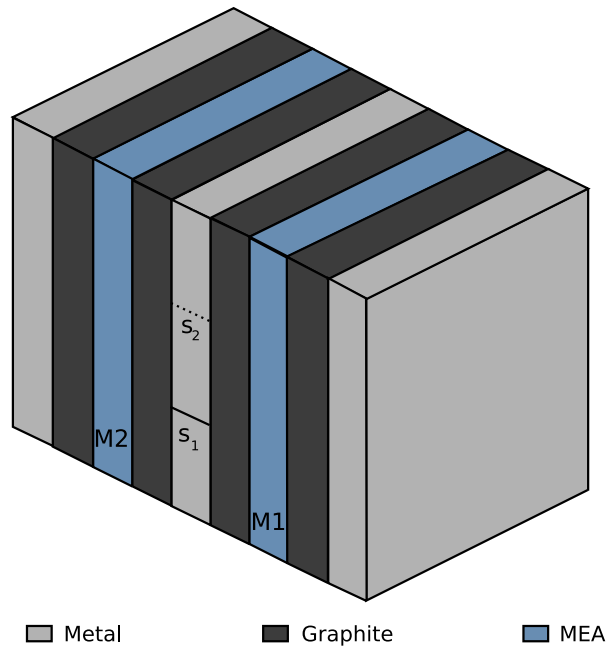
Figure 5.1: Sketch of the arrangement used for numerical calculations. The slitted aluminum plate is sandwiched between two fuel cells. Each of the MEAs is surrounded by two flowfield plates. The system is confined at both sides by aluminum plates, on whose outer surface constant Neumann boundary conditions of about $1666 \, \text{A} \cdot \text{m}^{-2}$ are defined. Everywhere else the Neumann boundary condition is zero. The size of the fuel cells and that of each plate is $200 \, \text{mm} \times 180 \, \text{mm} \times 1 \, \text{mm}$. The thickness of the slits is set to $1 \, \text{mm}$. The connection of the upper slit s_2 is placed on the opposite side of the aluminum plate (indicated by the dotted line).

it suffices to choose the separation equal to the layer thickness $\Delta y = 10^{-3}$m. The X-Z-plane is separated in dependency of the slit number. As each slit should be modeled correctly but a separation equal to the slit size is too expensive, the FV-grid is refined in the vicinity of a slit. Actually two FV-cells form the width of a slit for a more precise calculation of the parasitic currents via the graphite plate. In Fig. (5.2) the grid in the vicinity of slits is shown. The FV-cell size increases stepwise with the distance from the slit in the following manner: $0.5 \, \text{mm} \rightarrow 1 \, \text{mm} \rightarrow 2 \, \text{mm} \rightarrow 3 \, \text{mm} \rightarrow \approx 5 \, \text{mm}$, where the smallest value is the FV-cell width inside of the slit. The largest one is the maximal FV-cell width, which is not exactly $5 \, \text{mm}$, since it is adjusted in such a manner, that the grid covers the fuel cell surface completely. Based on these regulations, the previously discussed fuel cell arrangement (c.f. Fig. (5.1)) is discretized as shown in Fig. (5.3).

5.1.2 The slit bridge resistance

As seen before, the resistance of the bridge is the crucial quantity, which decides the applicability of the diagnostic method. Though it does not suffice to model the bridge in the metal plate and calculate the currents through it. In reality a measurement device is
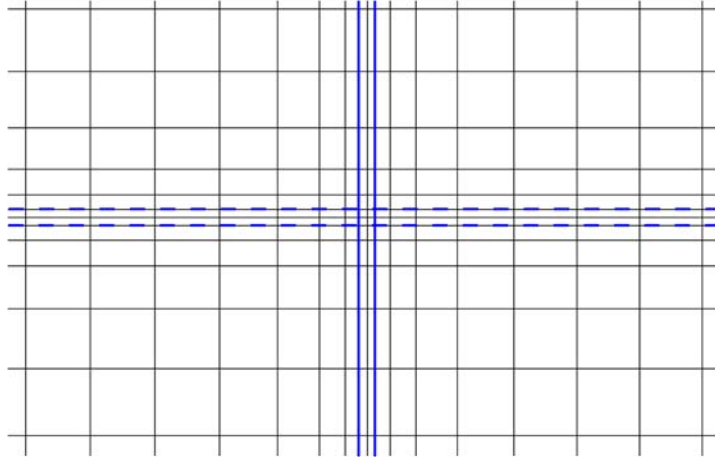
Figure 5.2: The finite-volume grid in the vicinity of slits. The borders of one slit is indicated by the vertical blue lines, the borders of the slit in the following metal plate is indicated by the horizontal dashed line. The FV-cell size increases stepwise to the maximal FV-cell size in the X-Z-area.

connected to both stripes to measure the bridge current. Therefore the inner resistance of such a measurement device and its contact to the metal plate needs to be considered. To implement this into the finite-volume method, Neumann boundary conditions $i_{S,a}$ and $i_{S,b}$ are imposed by a narrow margin above ($i_{S,a}$) and below ($i_{S,b}$) the slits. These have to obey the rule $i_S = i_{S,a} = -i_{S,b}$. The boundary value problem is solved for an initial guess. This yields the potentials $\phi_{S,a}$ and $\phi_{S,b}$ at the contact points. Based on the voltage drop and the current i_S, the bridge resistance $R_S = \Delta\phi_S/i_S$ can be calculated. In this way the bridge resistance as a function of the bridge current $R_S(i_S)$ is obtained. However, the bridge currents are unknown and the bridge resistance is given, therefor the inverse function $i_S(R_S)$ is wanted. More precisely the bridge currents for a given resistance R_0 is sought. This problem can be described as a zero-point search for the quantity $\Delta R = R_S - R_0$, which is solved by the Pegasus algorithm[37, 38]. Thus the exact bridge currents for a given bridge resistance R_0 is obtained.

A representative bridge resistance, which determines whether the diagnostic scheme is applicable to a particular fuel cell, has to be found. The resistance connected to the maximal ohmic powerloss at the bridge is influenced by the parasitic currents across the graphite plates. If the bridge resistance is larger than the one leading to the maximal powerloss, the parasitic currents surpass the ones at the bridges. Hence, this resistance represents the magnitude of parasitic losses in a given fuel cell and is furthermore an upper limit which should not be exceeded by measuring devices. It is determined by manually varying the bridge resistance. For isotropic graphite and a variety of typically used graphite flowfield materials (c.f. Tab. (5.1)) this resistance is determined. If it is larger than the inner resistance of a commercial measurement device, it is possible to measure the emerging bridge currents. This is applied to the arrangement shown in Fig. (5.1) and respectively Fig. (5.3), whereas only one slit is needed to determine the
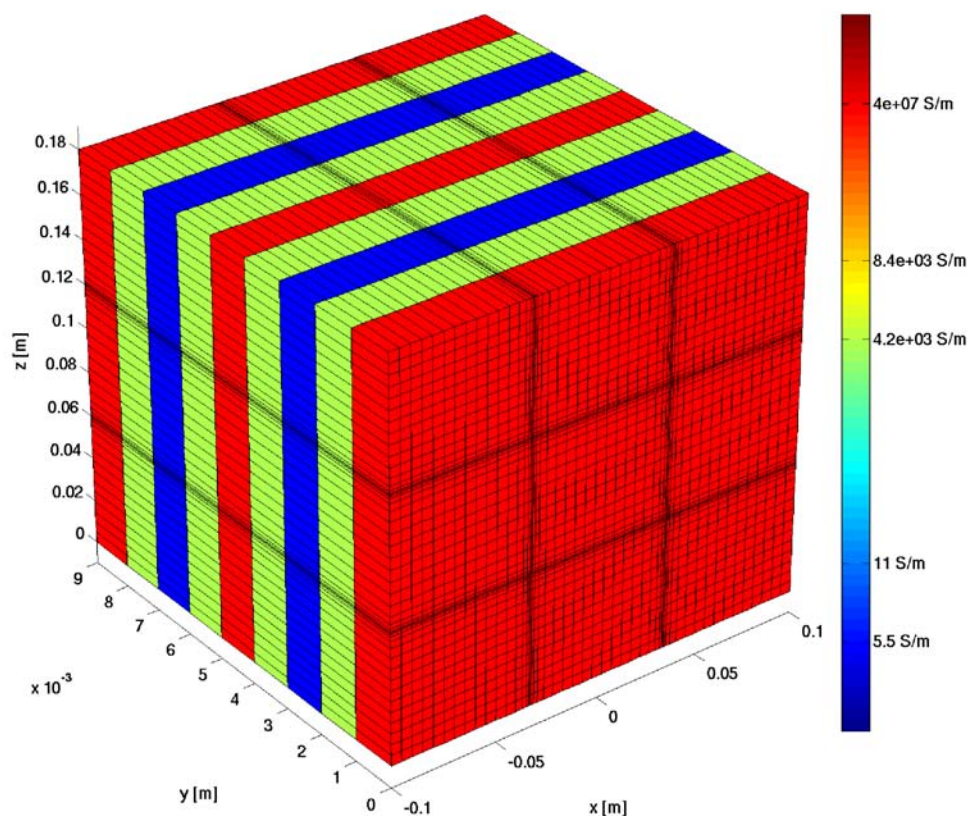
Figure 5.3: Finite-volume grid of the simulated fuel cell arrangement. The color code defines the conductivity of a layer. The aluminum plates are the red layers, the graphite flowfield plates (at this fabricated of isotropic graphite) are indicated by the green layers and the blue layers are the MEAs. Even though there is only one slitted metal plate (the central one), the grid is refined in the vicinity of both possible slits direction (in the X- and Z-direction).

resistance connected with the maximal powerloss. The slit is oriented in the Z-direction. A defect is placed in the MEA M1. Its area is one ninth of the total fuel cell surface and its conductivity is set to $\sigma_d = 10^{-5}\,\mathrm{S\cdot m^{-1}}$. In the rest of the MEA the previous discussed (c.f. section 3.2) conductivity of $\sigma_{\mathrm{MEA}} = 5.5\,\mathrm{S\cdot m^{-1}}$ is used, since the exact value is of no concern at this point. Applying this gemometry to Eq. (3.5)[2], the corresponding characteristic current is given by $i_Q = 3.75\,\mathrm{A}$. The resulting bridge resistances are listed in Tab. (5.2). These results are compared with a low cost commercial current sensor.

---

[2]In the analytical formula, the defect conductivity has no contribution. But as the conductivity of the defect in the numerical arrangement is five orders of magnitude smaller than the one in the remaining MEA, it is valid to assume an isolating damage for the calculation of the characteristic current i_Q.

flowfield material	$\sigma_\perp$ [S $\cdot$ m^{-1}]	$\sigma_\parallel$ [S $\cdot$ m^{-1}]
isotropic graphite	$4.2 \cdot 10^3$	$4.2 \cdot 10^3$
Eisenhuth Sigracet PPG 86	$5.6 \cdot 10^3$	$1.8 \cdot 10^3$
Eisenhuth Sigracet BMA 5	$1.0 \cdot 10^4$	$2.0 \cdot 10^3$
Eisenhuth Sigracet BBP 4	$2.0 \cdot 10^4$	$4.2 \cdot 10^3$
SGL Sigraflex	$1.3 \cdot 10^5$	$1.7 \cdot 10^3$

Table 5.1: List of transverse and normal conductivities ($\sigma_\perp$ and $\sigma_\parallel$) representing typical materials being used for flowfield plates of low and medium temperature fuel cells and in addition isotropic graphite.

flowfield material	R_{S} [$10^{-3}\,\Omega$]	i_s [A]	P_s [mW]
isotropic graphite	1.64	1.81	5.35
Sigracet PPG 86	1.67	1.81	5.46
Sigracet BMA 5	1.18	1.77	3.69
Sigracet BBP 4	0.66	1.66	1.80
Sigraflex	0.38	1.48	0.85

Table 5.2: Resistances leading to maximum powerloss at the bridges for flowfield plates of typical materials (c.f. Tab. (5.1)). The bridge current i_s and the corresponding power loss P_s is presented as well, whereas these values are bound to the specific damage.

As a reference the *Allegro Current Sensor: ACS750*[3] is used[4]. The inner resistance of this IC-sensor is only $120\,\mu\Omega$, and is therefore smaller than any resistance presented in Tab. (5.2).

5.1.3 Bridge currents for various graphite plates

The bridge currents emerging at the locations s_1 and s_2 of the arrangement shown in Fig. (5.1) are calculated for the graphite plates of Tab. (5.1). For a comparison to the simple model, there are also three different locations of the same damage included in the calculation. The locations are in the center of each stripe. Due to the parasitic currents, the ideal values presented in Tab. (3.1) can not be reproduced completely. To quantify the loss of signal intensity, the fraction of the remaining bridge current

$$\alpha = \frac{i_Q^*}{i_Q} \tag{5.1}$$

is introduced, where i_Q^*[5] denotes the remaining characteristic current. The characteristic current for the double slitted aluminum plate in reference to Eq. (3.5) is $i_Q = 2.5\,\mathrm{A}$.

---

[3]Build by Allegro MicroSystems, Inc., Worcester, Massachusetts, U.S.A.

[4]Many thanks to Heinz Pfeifer for calling our attention to this current sensor.

[5]Average of the individual bridge currents, where the $2i_Q$ values contribute with the weight $1/2$ each.

	damage position	i_{s_1} [A]	i_{s_2} [A]	i_{s_1}/i_{s_2}
isotropic graphite	top	-1.128	-2.308	0.488
$i_Q^* = 1.161\,\mathrm{A}$	middle	-1.201	1.201	-1
$\alpha = 0.46$	bottom	2.308	1.128	2.046
Sigracet PPG 86	top	-1.129	-2.296	0.492
$i_Q^* = 1.155\,\mathrm{A}$	middle	-1.188	1.188	-1
$\alpha = 0.46$	bottom	-2.296	1.129	2.034
Sigracet BMA 5	top	-1.1	-2.225	0.494
$i_Q^* = 1.118\,\mathrm{A}$	middle	-1.132	1.132	-1
$\alpha = 0.45$	bottom	2.225	1.1	2.023
Sigracet BBP 4	top	-1.021	-2.056	0.497
$i_Q^* = 1.054\,\mathrm{A}$	middle	-1.032	1.032	-1
$\alpha = 0.42$	bottom	2.056	1.021	2.014
Sigraflex	top	-0.903	-1.708	0.529
$i_Q^* = 0.854\,\mathrm{A}$	middle	-0.805	0.805	-1
$\alpha = 0.34$	bottom	1.708	0.903	1.891

Table 5.3: The bridge currents at the locations s_1 and s_2 (c.f. Fig. (5.1)) compared for various graphite plates (c.f. Tab. (5.1)). Furthermore the remaining characteristic currents i_Q^* and the reduction factor α is given for each graphite plate.

Tab. (5.3) shows the results for the different materials, computed with the resistance for maximum powerloss given in Tab. (5.2). Already at a first glance, the similarity between the current ratios i_{S_1}/i_{S_2} obtained from the realistic computations (c.f. Tab. (5.3)) and those of the simple model (c.f. Tab. (3.1)) is obvious. The reason for that is the high conductivity of aluminum and the small (effective) conductivity of the MEAs. Therefore a damage in a MEA leads to transverse currents between the aluminum stripes that can be rather well estimated by the simple model. Of course the simple model is unable to predict how much of these currents will pass the locations s_i where the stripes are connected. Indeed currents can bypass a slit between two stripes by diving into the graphite and returning into the aluminum. However, because of the high conductivity of aluminum this happens along the total length of the slit and gives rise to a resistance being both rather independent of the damage location in a stripe and nearly the same for all stripes. An averaged reduction factor $\alpha > 0.3$ should be acceptable. The actual α values are shown in Tab. (5.3).

5.1.4 Thickness of metal plates

If the diagnostic scheme is applied to a 100 cell stack, the total length increases by about 10cm. Stack size is no major problem for stationary applications like block-unit power stations or in quasi-stationary applications on vessels. Though in mobile applications the stack size and the weight of the total fuel cell system are crucial parameters. Therefore

it is meaningful to investigate the reduction factor dependency on the aluminum plate thickness. Based on the internal resistance of the Allegro current sensor and on the resistance for the maximal powerloss, this dependency is computed. In all finite-volume computations presented in this chapter, the grid layer thickness in y-direction is fixed. Therefore the resistance of the slitted metal plate is modified to simulate a change in the metal plate thickness. The transverse $\sigma_\perp$ and the normal $\sigma_\parallel$ conductivities are modified to such an extent, that the conductance $L^*_{\perp,\parallel}$ in both directions of the $d_y = 1\,\mathrm{mm}$ thick metal plate corresponds to the conductance $L_{\perp,\parallel}$ of the plate with reduced thickness $\gamma \cdot d_y$. The normal conductance of the metal plate of reduced thickness is given by:

$$L_\parallel = \frac{d_x \cdot d_z}{\gamma \cdot d_y} \cdot \sigma_\parallel \tag{5.2}$$

The conductance with the modified conductivity by:

$$L^*_\parallel = \frac{d_x \cdot d_z}{d_y} \cdot \sigma^*_\parallel \tag{5.3}$$

From $L_\parallel = L^*_\parallel$ follows

$$\sigma^*_\parallel = \frac{\sigma_\parallel}{\gamma} \tag{5.4}$$

and respectively for the transverse conductivity:

$$\sigma^*_\perp = \gamma \cdot \sigma_\perp \tag{5.5}$$

Using the arrangement as shown in Fig. (5.1) with only one slit again, the reduction factor dependency of the metal layer thickness is calculated. In fact the function $\alpha(\gamma)$ is calculated for three different bridge resistances per material.

1. The resistance connected with the maximal powerloss at the bridge.

2. An estimated total resistance of the measurement device and the harnessing. An optimistic estimate is the double internal resistance of the Allegro current sensor: $R_\mathrm{S} = 0.24 \cdot 10^{-3}\,\Omega$.

3. An more pessimistic estimate of the total resistance: $R_\mathrm{S} = 0.5 \cdot 10^{-3}\,\Omega$

Although Eq. (5.4) and Eq. (5.5) are correct for real conductor plates of different thickness and the harmonic mean value for material interfaces is used in the finite-volume discretization, the conductivity modification simulates only changes in layer thickness. Therefore the results presented in Fig. (5.4) should be seen qualitatively. On first glance the graphs show large similarities. The curves can be separated into three parts. At low γ values, the reduction factor is independent of the bridge resistance and is only given by the resistance of the metal plate itself. The higher the γ value, the more important are the bridge resistances. Thus in this intermediate part of the curve the reduction factors increases with a slope inverse proportional to R_S. At high γ values the reduction factor converges to a constant value given by the bridge and the flowfield material.
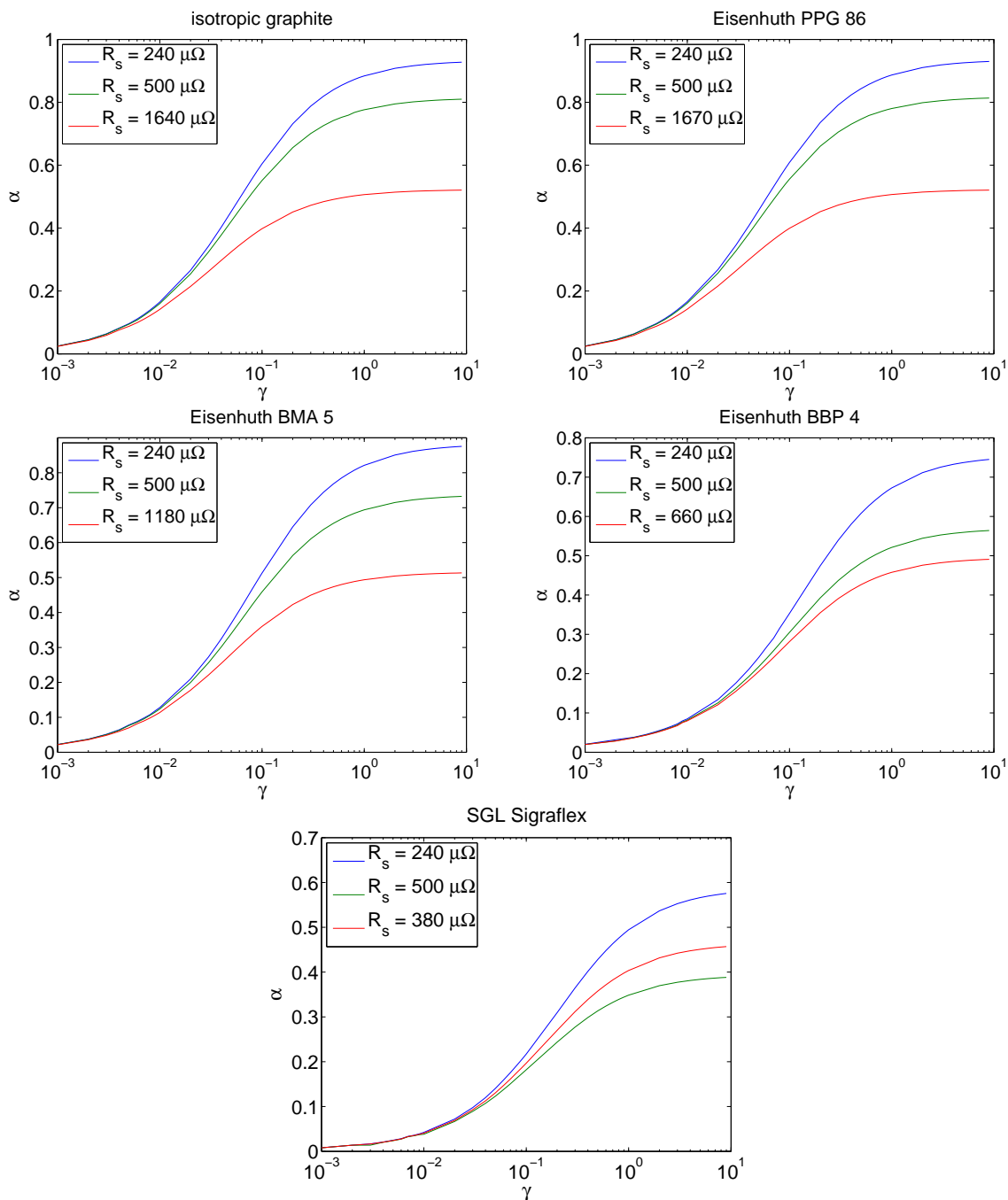
Figure 5.4: Qualitative results for the reduction α dependency on the metal layer thickness represented by the γ factor.

closing pressure $[\mathrm{KN \cdot cm^{-2}}]$	$\sigma_{\mathrm{dl},\parallel}$ $[10^3 \mathrm{S \cdot m^{-1}}]$
0.049	0.442
0.099	0.761
0.148	1.142
0.198	1.370
0.247	1.713
0.296	1.958
0.346	2.284
0.395	3.426
0.444	4.568

Table 5.4: The closing pressure dependent normal conductivity of the diffusion layer fabricated by "Freudenberg". The measurements have been done by A. Glüsen in the "Forschungszentrum Jülich".

If only a reduction factor of $\alpha = 0.3$ should be maintained, the aluminum thickness can be reduced in most cases. For the pessimistic estimate of the total measuring device resistance, the aluminum plate thickness could be reduced to 30μm for isotropic graphite and PPG 86, to 50μm for BMA 5 and to 100μm for BBP 4. Whereas when Sigraflex is used, the aluminum plate thickness should not be reduced at all.

5.1.5 Diffusion layer

In a PEM fuel cell, there is a further layer, which is not included in the calculations. The gas diffusion layer typically consists of graphite paper, felt or fabric with a thin coating of Teflon for increased hydrophobia. This layer is inserted between MEA and flowfield plate to increase the homogeneity of the gas distribution on the electrode surface. The normal electric conductivity depends strongly on the closing pressure of the fuel cell stack (c.f. Tab. (5.4)). The transverse conductivity is closing pressure independent $\sigma_{\mathrm{dl},\perp} = 6 \cdot 10^3 \mathrm{S \cdot m^{-1}}$. At high pressures the conductivity of this material is in both directions larger than the one of isotropic graphite. An approximation clarifying this behavior is given in the appendix A.5. Since the diffusion layer is only $0.2\,\mathrm{mm}$ thick, its contribution to the total parasitic current is small. Furthermore it is problematic to include it into the finite-volume grid, since the layer thickness is fixed. Therefore it has been omitted. Using the same method as in the determination of the $\alpha(\gamma)$ dependency, it is possible to estimate the impact of the diffusion layer on the reduction factor. As closing pressures of about $0.3\,\mathrm{KN \cdot cm^{-2}}$ are typical in fuel cell stacks, a normal conductivity of $\sigma_{\mathrm{dl},\parallel} = 2000\,\mathrm{S \cdot m^{-1}}$ is used in the computation. Based on Eq. (5.4) and Eq. (5.5), the modified conductivities used in the finite-volume calculations are

$$\sigma_{\mathrm{dl},\parallel}^{*} = 1.0 \cdot 10^4 \mathrm{S \cdot m^{-1}} \tag{5.6}$$
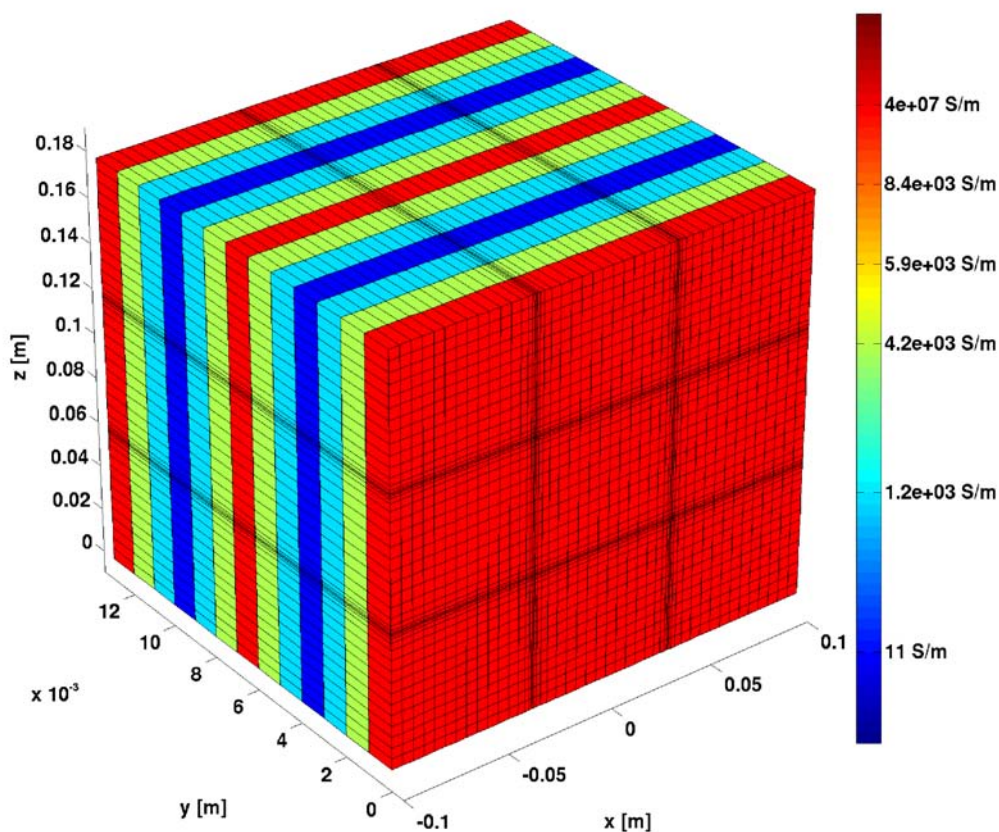
Figure 5.5: Modification of the finite-volume grid of the arrangement shown in Fig. (5.1). The only change is the addition of diffusion layers (pale blue).

$$\sigma_{\mathrm{dl},\perp}^{*} = 1.2 \cdot 10^{3}\mathrm{S} \cdot \mathrm{m}^{-1} \tag{5.7}$$

The calculations are done on the grid shown in Fig. (5.5) with the same bridge resistances as in the previous calculations (c.f. Tab. (5.3)). Thus the impact can be seen directly. The results in Tab. (5.5) show that the impact of the diffusion layer is smaller than 10% and larger for materials with low transverse conductivity. As there are actually no flowfield plates fabricated of isotropic graphite, the material with the largest deterioration due to the diffusion layer is PPG 86. The loss for this material is even less than 7%. The impact on systems with BBP 4 and Sigraflex can be completely neglected. Since in an equivalent circuit the diffusion layer and flowfield plate are parallel resistors (R_{dl} and R_{ff}), the fraction of the current flowing through the diffusion layer resistor is determined by quotient $R_{\mathrm{ff}}/R_{\mathrm{dl}}$. For BBP 4 this fraction is about 0.1 and for Sigraflex even one order of magnitude smaller. Thus the entire current flows through the Sigraflex layer no matter if there is a parallel diffusion layer or not.

material	$i^*_{Q,\mathrm{dl}}$ [A]	α_{dl}	$\alpha_{\mathrm{dl}}/\alpha$
isotropic	1.005	0.42	90.5%
PPG 86	1.077	0.43	93.3%
BMA 5	1.068	0.43	95.5%
BBP 4	1.005	0.42	99.5%
Sigraflex	0.850	0.34	100%

Table 5.5: Characteristic currents $i^*_{Q,\mathrm{dl}}$ and the reduction factor α_{dl} with the addition of the diffusion layer in the arrangement.

5.2 Stabilization of fuel cell stack operation

It is quite normal that even a well functioning fuel cell has a locally varying current density. These variations may be either static or dynamic. As unproblematic as this variation may be for a single cell the situation in the stack can be quite different since these variations can accumulate. The situation may become worse if one or more fuel cells are damaged in certain areas of their MEA but still doing their jobs. For avoiding accumulations in all these cases it is mandatory not to allow any irregularity of one cell to influence the next or the previous one. This problem has been investigated by computing a large arrangement consisting of a damaged fuel cell embedded in seven intact ones on both sides. By that it is possible to investigate the damage propagation in arrangements with different flowfield materials. In the arrangement with additional aluminum plates, the number of intact cells is reduced.

5.2.1 Stack without metal plates

The stack, whose finite-volume grid is shown in Fig. (5.6), is taken into account by assuming that a homogeneous current enters the aluminum plate before the first fuel cell and a homogeneous current is leaving the aluminum plate after having passed the last fuel cell. A worst case scenario, namely a massive failure in the MEA of the central fuel cell with the result that the lower third of the MEA does not produce current at all, is simulated. This is again done by setting the conductivity in the damaged part of the MEA to $\sigma_d = 10^{-5}\mathrm{S}\cdot\mathrm{m}^{-1}$. The intact conductivity of the MEAs is set to the previous discussed (c.f. section 3.2) conductivity of $\sigma_{\mathrm{MEA}} = 5.5\,\mathrm{S}\cdot\mathrm{m}^{-1}$. For flowfield plates fabricated of isotropic graphite the resulting current densities in the defect MEA and in the following ones are shown in Fig. (5.7). Obvious is the strong current density peak in the direct neighborhood of the damage in the MEA of the central fuel cell. Such a peak will probably lead to a fast expansion of the damage. Furthermore a steep dip at the same location appears in the MEA of the following fuel cells, which attenuates slowly with the fuel cell index[6]. Although the second cell is undamaged, this dip will

---

[6]The fuel cell index describes the location of a fuel cell in reference to the damaged one, which has the index $i = 0$. As the damage propagation is identical in both directions, if there is no difference
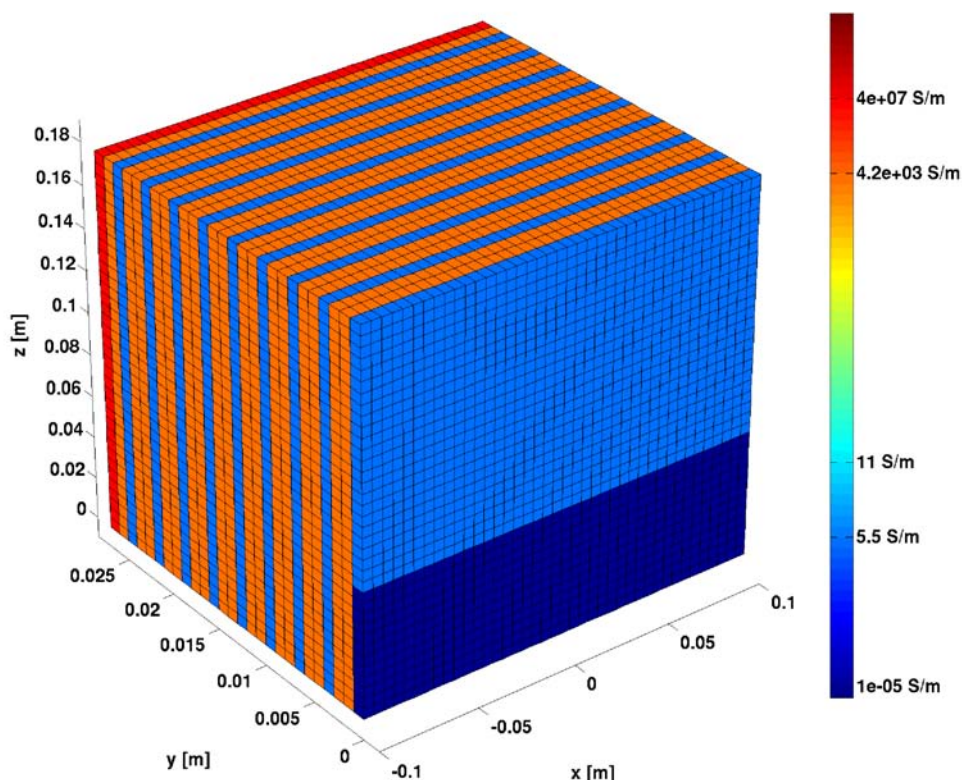
Figure 5.6: One half of the finite-volume grid of the arrangement used to investigate the defect propagation is presented here. The MEA shown in the front is the defect one. The large damage is indicated by the dark blue color. For better visibility only one half of the arrangement is shown here. The shown stack is additionally folded back on the front side of the defect MEA. The entire arrangement is again confined by aluminum plates.

probably lead to a damage in the second MEA. A resulting damage will then lead to an increased dip in the third one. In fact one has to be afraid of a chain reaction leading to more and more ill-working cells in the stack.

5.2.2 Stack with additional metal plates

The stack, whose finite-volume grid is shown in Fig. (5.8), is taken into account by assuming that a homogeneous current enters the aluminum plate before the first flowfield plate and a homogeneous current is leaving after having passed the last fuel cell, its flowfield plates and the aluminum plate. For the same damage in the central MEA as before the results are shown in Fig (5.9). Only small peaks of the electric current due to the slits can be detected. In the defect cell a step like behavior of the current density

---

in structure, the fuel cell index defines the ith fuel cell both in forward and in backward direction.

(a) i=0 (defect MEA)
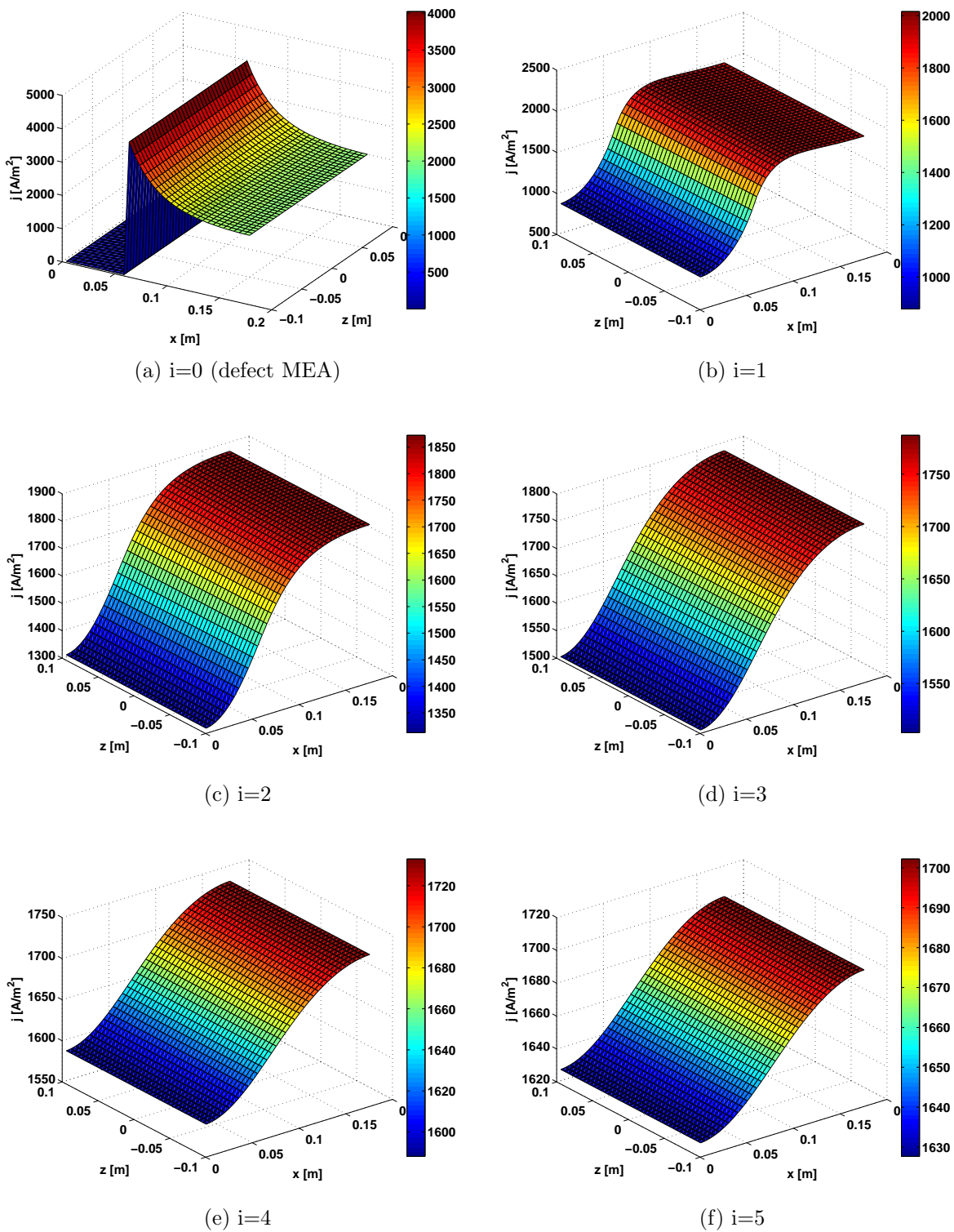
(b) i=1

(c) i=2

(d) i=3

(e) i=4

(f) i=5

Figure 5.7: The current density distribution in MEAs of a stack with flowfield plates fabricated of isotropic graphite. No aluminum plates are added in this calculation. The fuel cell index $i = 0...5$ defines the MEA in the stack, where the $i = 0$ MEA is the central one. As the current distribution is the same on both sides of the defect MEA, it suffices to investigate one direction. The color code defines the current density given in $A \cdot m^{-2}$.
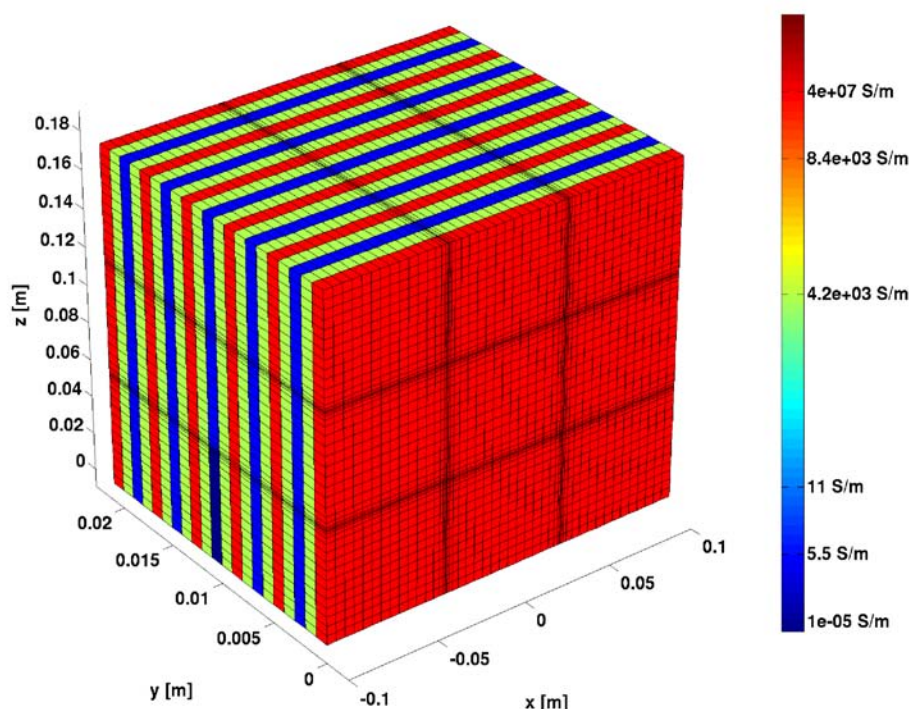
Figure 5.8: Finite-volume grid of the arrangement used to investigate the defect propagation under the usage of slitted aluminum plates. Since more than one slitted metal plate is present in this arrangement, neighboring plates are actually slitted perpendicular. For the bridge resistance the value corresponding to the maximal powerloss is used. Since a very short damage propagation is expected, only two fuel cells on both sides of the defect one is taken into account. The central cell is the defect MEA. The entire arrangement is again confined by aluminum plates without slits.

can be seen, this is due to the bridge resistance, which prevents a total compensation of the current density. For a damage limited in both X- and Z- direction, a checker is expected. Since the graphite plates cannot compensate the current density disturbance evoked by the slits, a small inhomogeneity in the MEA current occurs. This disturbance is about $1\,\mathrm{A}\cdot\mathrm{m}^{-2}$ for isotropic graphite, and even less for each of the other materials, therefore it can be neglected.

5.2.3 Comparison of defect propagation

The defect propagation without metal plates is calculated for all graphite materials, whereas the propagation with metal plates is only calculated for the material with the worst propagation, namely isotropic graphite. The peak height in the defect MEA is presented in Tab. (5.6). The dip depth for the fuel cell $i = 1...7$ is compared in Fig. (5.10). As expected, the higher the transverse conductivity of the combined layer between fuel cells, the lower the defect propagation and the lower is the peak strength in the defect
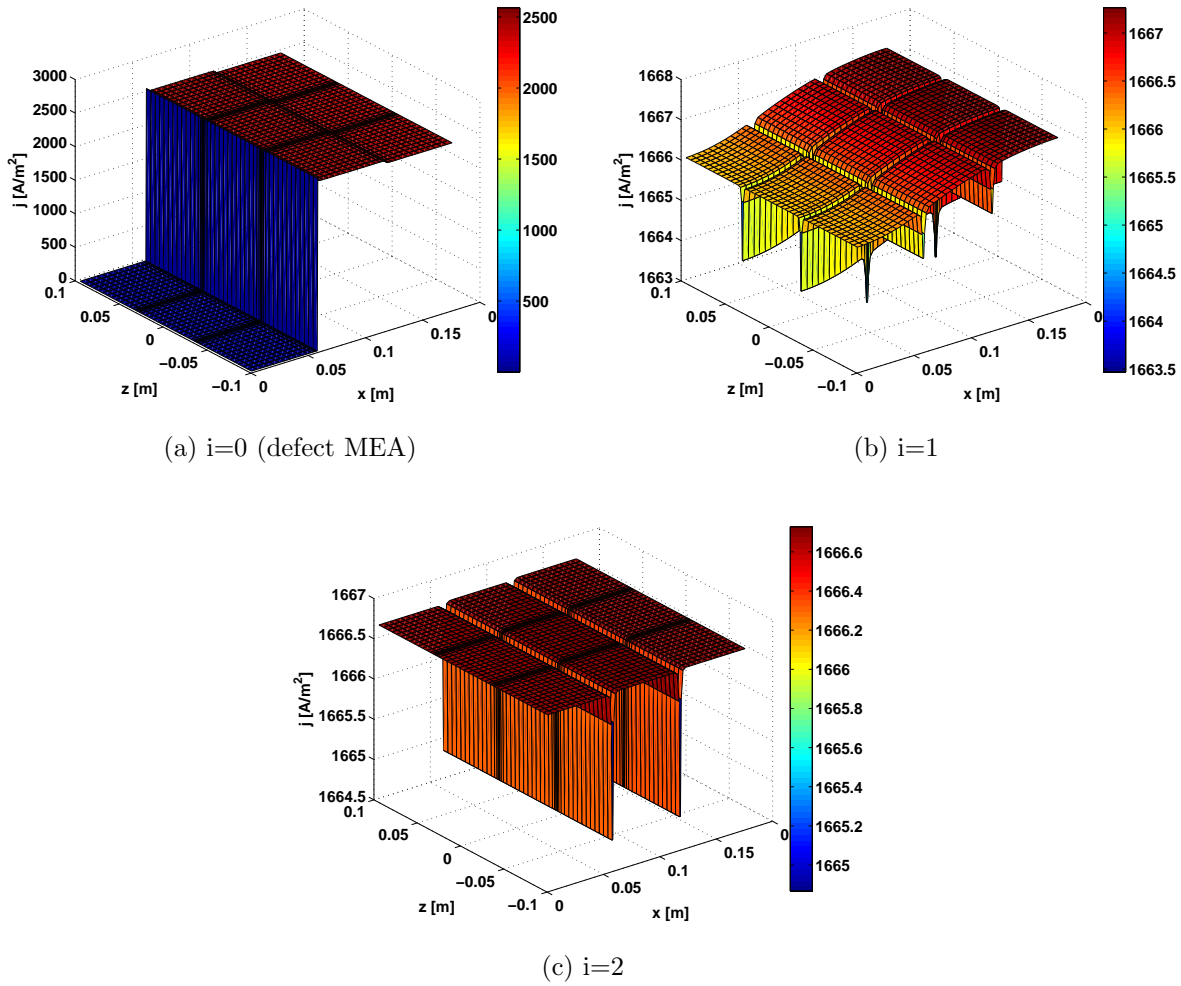
(a) i=0 (defect MEA)

(b) i=1

(c) i=2

Figure 5.9: The current density distribution in MEAs of a stack with flowfield plates fabricated of isotropic graphite. In this calculation aluminum plates are added. The fuel cell index $i = 0...2$ defines the MEA in the stack, where the $i = 0$ MEA is the central one. As the current distribution is the same on both sides of the defect MEA, it suffices to investigate one direction. The color code defines the current density given in $A \cdot m^{-2}$.

MEA itself. One could expect that the current density in the defect MEA is, except for the damage itself, homogeneous if aluminum plates are present. But due to the finite resistance of the measuring device, a step like structure is obtained. Even with the step, the current density is more homogeneous than in each of the other calculated systems. Furthermore the damage propagation is prevented completely by the aluminum plates[7]. Thus it is shown that the MEAs are electrically independent of each other. Although the defect propagation inhibition from Sigraflex seems rather impressive, these results

---

[7]Only a slight deviation can be seen in Fig. (5.9b), which has the magnitude of the slit disturbances.

material	$\Delta j \ [\mathrm{A} \cdot \mathrm{m}^{-2}]$
isotropic graphite	1976
PPG 86	1762
BMA 5	1345
BBP 4	922
Sigraflex	224
iso graphite + aluminum plates	86

Table 5.6: The peak height in the defect MEA is calculated by the maximal current density difference outside of the defect.

has to be treated with caution, as massive graphite plates are calculated. However the channels in the flowfield plates reduces the transverse conductance, which leads to a worse inhibition.

5.3 Assembling the linear transformation

The linear transformation matrix $\mathcal{A}$ (c.f. Eq. (3.15)) is determined numerically. It is convenient to do this by assembling an orthonormal basis $\{\vec{v}_n\}$ in such a way, that each bridge current vector $\vec{i}_\mathrm{S}$ can be obtained by a linear combination of this basis:

$$\vec{i}_\mathrm{S} = \sum_n a_n \vec{v}_n, \quad a_n : \ n^{th} \text{ linear factor} \tag{5.8}$$

Since adjacent MEAs are electrically independent due to the high conductivity of the aluminum plates, only a single MEA, the defect one, needs to be taken into account in this calculation. Furthermore, as only the normal current is an issue, and by following the thin MEA approximation (c.f. subsection 3.2.1), only the current density in the defect MEA is taken into account. Thus also the defect MEA can be omitted in the calculation, and the segment currents are given by Neumann boundary conditions. Fig. (5.11) shows the minimalistic arrangement, which is needed to determine the orthonormal basis vectors. This is still done with a high accuracy, as all needed components are included, the defect MEA currents predefined by Neumann boundaries on the one side, the flowfield plates reducing the signals and the homogeneous current density of the adjacent intact MEA on the other side. The currents are injected peak like on the side of the defect MEA. Thus the entire current can be uniquely allocated to one segment, as the current is still peak like when entering the metal plate. Fig. (5.12) shows the current density in the graphite plate between defect MEA and the slitted metal plate. For peak like current densities in each segment the bridge currents are calculated. Each resulting current vector is one basis vector $\vec{v}_n^*$, which is orthogonal to all other basis vectors obtained in this way, but it is not yet normalized. To obtain the orthonormal basis, each basis vector has to be normalized by the factor I_0^{-1}, since the entire stack current is injected
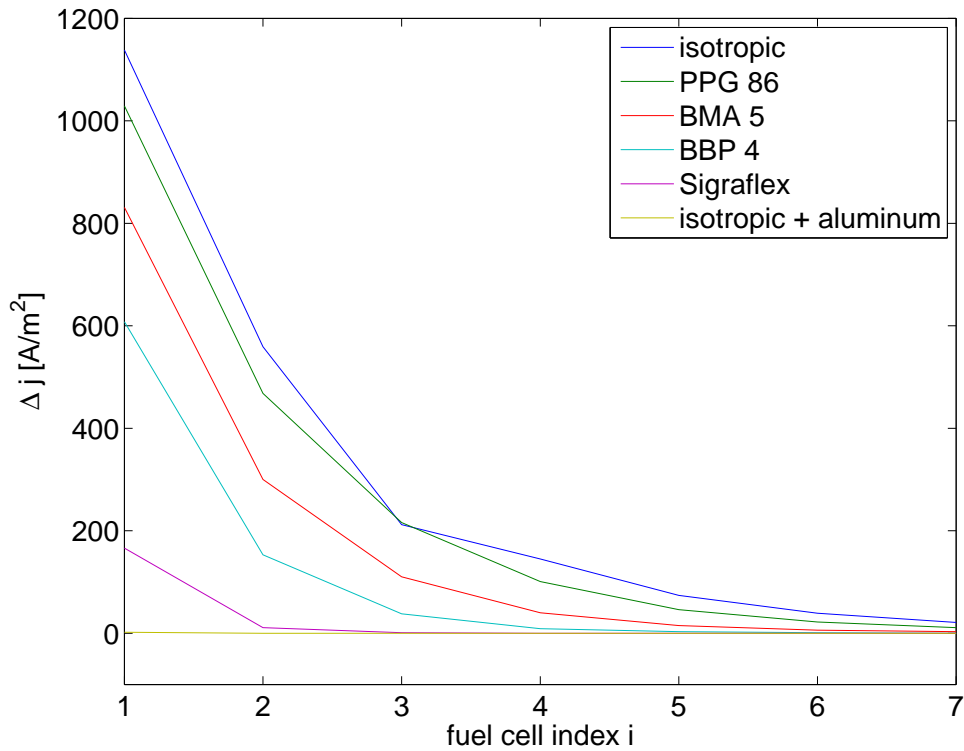
Figure 5.10: The defect propagation, expressed as the maximal current density difference Δj in dependency of the fuel cell index i.

as a peak in each segment.

To obtain the full basis $\{\vec{v}_n\}$, the currents in both metal plates confining one MEA need to be computed. Since there is only one slitted metal plate in the arrangement (c.f. Fig. (5.11)), the computation needs to be done for both a metal plate with slits in Z-direction and one with slits in X-direction. The homogeneous boundary and the one representing the defect MEA must be exchanged for one slit direction, since they are on different sides of the MEA. Together these basis vectors build the orthonormal basis $\{\vec{v}_n\}$. As this basis is chosen in such a way, that the linear factors are actually the corresponding segment currents, the basis $\{\vec{v}_n\}$ is in fact the sought linear transformation matrix $\mathcal{A}$. As an example the transformation matrix for two slits in an arrangement with PPG 86 flowfield plates is presented:

$$\mathcal{A} = \begin{pmatrix} -0.31 & 0.16 & 0.15 & -0.31 & 0.16 & 0.15 & -0.31 & 0.15 & 0.15 \\ -0.15 & -0.15 & 0.31 & -0.15 & -0.16 & 0.31 & -0.15 & -0.16 & 0.31 \\ 0.33 & 0.33 & 0.33 & -0.17 & -0.16 & -0.16 & -0.16 & -0.16 & -0.16 \\ 0.16 & 0.16 & 0.16 & 0.16 & 0.16 & 0.17 & -0.33 & -0.33 & -0.33 \end{pmatrix} \qquad (5.9)$$

Comparing this numerically assembled matrix to the analytical rule (c.f. subsection
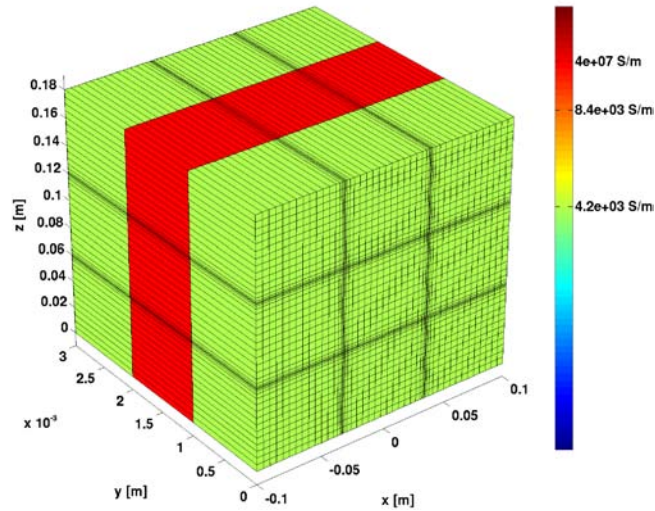
Figure 5.11: Finite-volume grid of the arrangement used in the linear transformation assembly. In the aluminum plate there are two parallel slits. On one side of the arrangement the Neumann boundary conditions are homogeneous and on the other side variable and peak like. The peak like boundary conditions represent the segment currents in the defect MEA.

3.2.2), it is obvious, that this matrix can be analytically reconstructed with $\beta_i = \alpha_{\text{PPG86}} \cdot i_Q$. There are minor variations in the matrix components in virtue of
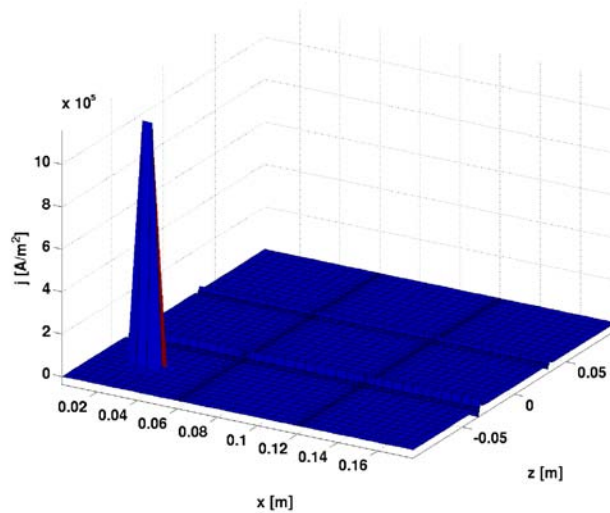

Figure 5.12: Current density distribution in the graphite plate between defect MEA and slitted metal plate. The current is injected peak like to build up a basis for the slit currents.

the damage location in a stripe. Furthermore, the matrix values corresponding to the slit in X-direction are slightly lower (the first two row vectors in Eq. (5.9)), since the same bridge resistance is used as the one for the slits in the Z-direction. As this resistance is determined by the maximal powerloss for the slits in Z-direction, an error is introduced at this point, but as the measurement device will be the same for all slits, the usage of a single resistance is close to reality.

6 The inverse problem

The connection between the current density in the MEA and the bridge currents is given by a linear transformation $\mathcal{A}$. The bridge currents $\vec{i}_\text{S}$ are invariant to two different kinds of current density variations in the MEA. First, local variations being smaller than a segment, which by that do not affect the total current across it. Therefore only the integrated current density over a segment

$$i_{\text{seg},n} = \int_{\text{seg},n} \vec{j}_\text{MEA} \cdot \vec{n}_\text{MEA} \, dx \, dz \tag{6.1}$$

influences the bridge currents. Based on this fact, the linear transformation connects the segment currents $\vec{i}_\text{seg}$ with the bridge currents $\vec{i}_\text{S}$

$$\mathcal{A} \cdot \vec{i}_\text{seg} = \vec{i}_\text{S} \tag{6.2}$$

The transformation $\mathcal{A}$ connecting the segment currents with the bridge currents is strictly linear. Since the segment size is given by the number of slits N_S in the adjacent metal plates, N_S also determines down to which lower boundary of spatial extent a variation can be detected.

Secondly, as the dimension of $\vec{i}_\text{seg}$ is

$$N_\text{seg} = (N_\text{S} + 1)^2 \tag{6.3}$$

and the dimension of $\vec{i}_\text{S}$ is only

$$N_\text{cur} = 2 \cdot N_\text{S} \tag{6.4}$$

there is a null space[1], which leads to an ambiguous mapping $\vec{i}_\text{S} \rightarrow \vec{i}_\text{seg}$. Thus there are variations in $\vec{i}_\text{seg}$, which do not change the value of $\vec{i}_\text{S}$. Segment current configurations leading to equal bridge currents do not need to be local. E.g. a homogeneous change in all segment currents induces no change in $\vec{i}_\text{S}$.

Besides increasing the number of slits, there is no possibility, neither physical nor mathematical, to encounter the first problem. For the second problem, it is possible to reduce the null space or rather pick a small number of solutions from the null space, which seems to meet the structure of a typical damage. Admittedly, the detailed structures of damages occurring in fuel cells are not well known. Nevertheless it is possible to discuss the inverse problem for some assumptive damage structures. Furthermore, the reduction

---

[1]The null space or kernel of a matrix $\mathcal{A}$ is the set of all vectors $\vec{x}$, which are mapped to the zero element (the zero or the zero vector). $Null(\mathcal{A}) = \{\vec{x}\epsilon R^n : \mathcal{A}\vec{x} = \vec{0}\}$ Therefore, the null space is the set of elements, the transformation cannot distinguish from the neutral element.

of the undetected local variations by increasing the number of slits has to be adjusted carefully, as the null space of the global problem increases quadratic with N_{S}.

6.1 The Lagrangian

In order to find solutions with specific attributes in a variety of solutions connected by the null space, it is meaningful to weight wanted and unwanted properties of solutions unequally. These properties could be spatial extent, minimal/maximal powerloss, specific structures and so forth. Furthermore there are properties, which have to be fulfilled, as the observance of the matrix equation

$$\mathcal{A} \cdot \vec{i}_{\mathrm{seg}} - \vec{i}_{\mathrm{S}} = \vec{0} \tag{6.5}$$

and the necessity of a constant total electric current

$$\sum_{n=1}^{N_{\mathrm{seg}}} i_{\mathrm{seg},n} = I_0 \tag{6.6}$$

The preferences and constraints are defined analytically[2] and are unified in a single equation, namely the Lagrangian L.

$$L(i_{\mathrm{seg}}, \lambda_\nu) = f(i_{\mathrm{seg}}) + \sum_\nu \lambda_\nu \cdot g_\nu(i_{\mathrm{seg}}) \tag{6.7}$$

The function $f(i_{\mathrm{seg}})$ contains an analytical form of the preferences. Since unwanted configurations get unfavorable function values, f is also called penal term. The functions $g_\nu(i_{\mathrm{seg}})$ contain the constraints. Each constraint is multiplied by a Lagrange parameter λ_ν. If the preferences are defined in such a way, that unwanted properties have higher weights, the function $f(i_{\mathrm{seg}})$, and by that the total Lagrangian, needs to be minimized with respect to the segment currents. If a constraint is not fulfilled, $\lambda \cdot g(i_{\mathrm{seg}})$ has a large positive contribution to the Lagrangian, if the constraint is fulfilled, it should not have any contribution at all. Therefore $g_\nu(i_{\mathrm{seg}})$ has to fulfill the condition

$$g(i_{\mathrm{seg}}) \begin{cases} > 0 & \text{,if constraint is not fulfilled} \\ \leq 0 & \text{, if constraint is fulfilled} \end{cases} \tag{6.8}$$

while the Lagrangian parameter has to obey:

$$\lambda \geq 0 \tag{6.9}$$

---

[2]Depending on the numerical algorithm used to solve this problem, it might be possible to treat some simple constraints logically, not analytically. More details about logical constraints can be found in the subsequent section.

If the Lagrangian is maximized with respect to the Lagrange parameters λ, the previous described behavior of the product $\lambda \cdot g(i_{\mathrm{seg}})$ is obtained. In the case of a fulfilled constraint, the corresponding g is negative, and thus λ should be negative to maximize L. Since this is not possible, the maximal value for L is obtained with $\lambda = 0$, therefore $\lambda \cdot g(i_{\mathrm{seg}})$ has no contribution to the Lagrangian. Whereas, if the constraint is violated, g is positive and due to the Lagrange parameter the contribution becomes dominant. As the minimal value of L with respect to i_{seg} is sought, the currents are changed until the constraint is fulfilled again and the contribution of $\lambda \cdot g(i_{\mathrm{seg}})$ vanishes. Using this method, it is possible to change the segment currents freely without any notice of the constraints.

6.1.1 Constraints

In the computations there are three kinds of constraints, while only one of them is no sum of analogous constraints.

Constancy of the total current   The constancy of the total current is not directly included as a constraint. Rather another one is used, which eventually leads to the constancy of the total current.

If Eq. (6.6) is directly used in the form

$$g(i_{\mathrm{seg}}) = \left(\sum_{n=1}^{N_{\mathrm{seg}}} i_{\mathrm{seg},n} - I_0 \right) \tag{6.10}$$

the total current constraint is observed, but it can lead to unphysical solutions. Following it, a solution may appear in which the current across a single segment is much larger than any other current occurring in this configuration. Due to the null space, this may be a valid solution. Also, if other segment currents decreased, the total current may be maintained. But physically this solution can only appear if the conductivity of the MEA has increased in this segment. Since it can be expected, that the augment of the MEA conductivity is very unlikely[3] in fuel cell operation, these solutions should be excluded.

To maintain Eq. (6.10) with decreasing local conductivities, the voltage across the MEA must increase. If the voltage is constant, the overall current is not. The pinning of the cell voltage is actually used to ensure that no solution corresponding to a local conductivity rise is obtained. Therefore the segment currents are only allowed to drop, which is the actually used constraint:

$$g_n(i_{\mathrm{seg}}) = i_{\mathrm{seg},n} - i_0 \tag{6.11}$$

with the unperturbed segment current $i_0 = I_0 / N_{\mathrm{seg}}$. This has to be applied to each segment.

---

[3]But not impossible. For example, the local closing pressure may change and lead to a lower local contact resistance.

The reduced currents $\vec{i}_{\text{seg}}$ do not fit to the bridge currents, which are determined under the conservation of the total current. But due to the linearity between $\vec{i}_{\text{seg}}$ and $\vec{i}_{\text{S}}$, it is possible to adapt the bridge currents to the new total current:

$$\vec{i}_{\text{S,new}} = \vec{i}_{\text{S,old}} \cdot \frac{1}{I_0} \sum_{n=1}^{N_{\text{seg}}} i_{\text{seg},n} \tag{6.12}$$

Afterwards, the segment currents are again adapted to the constant total current, which also yields the relative cell voltage change ζ due to the conductivity loss:

$$\zeta = \frac{U_{\text{new}}}{U_{\text{old}}} = I_0 \cdot \left(\sum_{n=1}^{N_{\text{seg}}} i_{\text{seg},n} \right)^{-1} \tag{6.13}$$

With this quantity the adaption of the segment currents can be expressed as:

$$\vec{i}_{\text{seg},I_0} = \vec{i}_{\text{seg}} \cdot \zeta \tag{6.14}$$

This procedure is only valid, if the potential across the fuel cell surface is constant. As the fuel cell is confined by aluminum plates, this requirement is very well satisfied.

Observance of the matrix equation   The most important constraint is the observance of the matrix equation Eq. (6.5). At this point the measured bridge currents are included in the inverse calculation. If this equation is not fulfilled, the results are worthless, since they wont lead to the measured bridge currents.

As the bridge currents need to be adapted to the changing total current, Eq. (6.5) transforms to

$$\mathcal{A} \cdot \vec{i}_{\text{seg}} - \vec{i}_{\text{S}} \cdot \frac{1}{I_0} \sum_{n=1}^{N_{\text{seg}}} i_{\text{seg},n} = \vec{0} \tag{6.15}$$

which can also be written as:

$$\left(\mathcal{A} - \frac{1}{I_0} \vec{i}_{\text{S}} \right) \vec{i}_{\text{seg}} = \vec{0} \tag{6.16}$$

Here, the notation $\mathcal{A} - \vec{i}_{\text{S}}$ denotes, that each row vector of $\mathcal{A}$ is subtracted by $\vec{i}_{\text{S}}$.

To observe the definition rule Eq. (6.8), the matrix equation Eq. (6.16) is slightly modified:

$$g(i_{\text{seg}}) = \left[\left(\mathcal{A} - \frac{1}{I_0} \vec{i}_{\text{S}} \right) \vec{i}_{\text{seg}} \right]^2 \tag{6.17}$$

In this way the deviation from the exact solution is the new constraint. Since this can not be negative, it always has a contribution to the Lagrangian[4].

---

[4]Except, if the matrix equation is fulfilled exactly, which is numerical very unlikely.

Maximal defect constraint Another (optional) constraint is added, if the damage inside of a particular segment is defined to be the maximal one. In this case, the current across this segment $i_{\min}$ is the minimal one of this configuration. Since the choice of the maximal defect segment is done arbitrarily, the obtained solution can lead to very unprobable segment currnet configurations. However if this procedure is applied to each segment, comparative conclusuions can be drawn. This is again a constraint, which needs to be applied to each segment:

$$g_n(i_{\mathrm{seg}}) = i_{\min} - i_{\mathrm{seg},n} \qquad\qquad \text{,with } n \neq \min \qquad (6.18)$$

6.1.2 The function $f(i_{\mathrm{seg}})$

In the choice of the function f there is even more freedom than in the choice of the constraints. To define it appropriately a deep insight about possible defect structures is required. Since this is only given terminally, a somewhat artificial function is chosen, which only includes the spatial extent of the damage. A function, which penalizes the deviation of segment currents from the homogeneous current i_0, favors local damages if it is applied to each segment current individually. Such a function is given by:

$$f(i_{\mathrm{seg}}) = \sum_{n=1}^{N_{\mathrm{seg}}} ln((i_{\mathrm{seg},n} - i_0)^2 + \epsilon) \qquad (6.19)$$

This cup-shaped function has a local minimum at i_0. As the singularity at i_0 has been circumvented by the $\epsilon > 0$ parameter, the function is analytical for all currents. The depth of the minimum is given by ϵ; the smaller ϵ the deeper the minimum. The function $f(i_{\mathrm{seg}})$ is plotted for several values of ϵ in Fig. (6.1).

6.1.3 The total Lagrangian

The Unification of all constraints and the function f leads to the total Lagrangian:

$$
\begin{aligned}
L(i_{\mathrm{seg},n}, \lambda_\nu) = \ & \sum_{n=1}^{N_{\mathrm{seg}}} ln((i_{\mathrm{seg},n} - i_0)^2 + \epsilon) \\[2mm]
& + \lambda_1 \cdot \left[\left(\mathcal{A} - \tfrac{1}{I_0}\vec{i}_{\mathrm{S}} \right) \vec{i}_{\mathrm{seg}} \right]^2 \\[2mm]
& + \sum_{n=1}^{N_{\mathrm{seg}}} \lambda_{n+1} \cdot (i_{\mathrm{seg},n} - i_0) \\[2mm]
& + \left\{ \sum_{n=1}^{N_{\mathrm{seg}}} \lambda_{n+N_{\mathrm{seg}}+1} \cdot (i_{\max} - i_{\mathrm{seg},n}) \right\}
\end{aligned}
\qquad (6.20)
$$

As mentioned before, the function f is minimal if all segment currents are equal to the homogeneous current i_0. However, the matrix equation constraint Eq. (6.17) does not allow this solution (if $\vec{i}_s \neq \vec{0}$). Thus the segment currents have to deviate from i_0. As $f(i_{\mathrm{seg}})$ is applied to each segment current individually, the Lagrangian is minimal for the
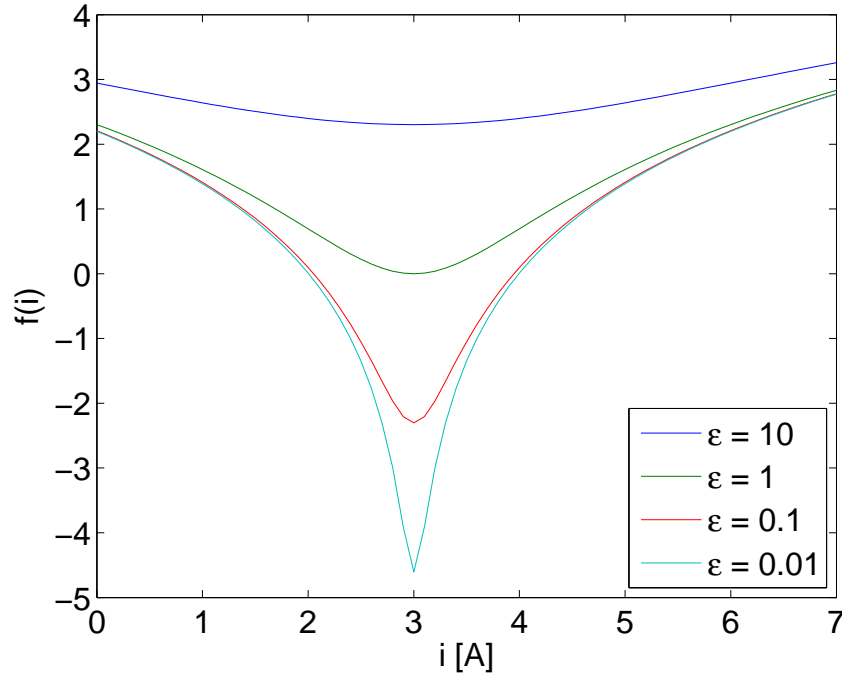
Figure 6.1: The function $f(i_{seg})$ plotted for $i_0 = 3\,\mathrm{A}$ and various values of the ϵ parameter. By constraints only the domain between $i_{seg} = 0\,\mathrm{A}$ and $i_{seg} = i_0$ is accessible.

smallest number of segment currents deviating from i_0 (as long as Eq. (6.17) is fulfilled). Since the matrix equation is included in the form of a constraint, it is guaranteed, that only valid solutions are obtained. Even though the minimization[5] of Eq. (6.20) can only lead to a solution in which barely a few segment current diverges from the homogeneous current i_0, it is possible to fine tune the localization by the factor ϵ. If the ϵ factor is changed over some orders of magnitude, the function f varies in such an extent, that solutions with different degrees of localization are obtained.

6.2 Minimization of the Lagrangian

Since Eq. (6.1) is no convex function, there are obviously local minima, whose number is not known but increases with the slit number. Therefore it is not possible to find the saddle point of the Lagrangian Eq. (6.20) by direct means. Hence the simulated annealing method (c.f. section 4.2) is used to find the global saddle point. In this section the basic program used to compute the minimum-maximum problem is described. Since there are different kinds of computations, the details of these are presented together with the results in the next section.

---

[5]It is not only a minimization with respect to the segment currents, but in addition a maximization with respect to the Lagrange parameters λ. Thus it is in fact a saddle point search.

1. At first the values are initialized, the segment currents are set to i_0 and the Lagrange parameters to zero. Since this is not a thermodynamic system, an artificial temperature parameter should be defined. An initial value of $\beta_0 = 10^5$ is chosen. Furthermore the temperature change rate is set to $\Delta\beta = +10^4$. By the choice of the reciprocal temperature change, the annealing speed decreases during the process. The initial variable shifts are set consistently to $\Delta i = \Delta\lambda = 0.05$ and the change in the variable shift to $\xi = 0.9$. At last the Lagrangian value for the initial configuration is calculated.

2. For the variable shift a simple random number generator is used. Due to the uniform distribution of this generator, the variables are shifted with equal probability by a value between $-0.5\Delta i$ and $+0.5\Delta i$.

3. At this point some minor, but nevertheless important, constraints are included. These constraints only contribute by rejecting the corresponding step if they are violated, but they do not change the value of the Lagrangian in any kind. Thus they are referred to as logical constraints (in comparison to the previous discussed analytical constraints). As neither the Lagrange parameters nor the segment currents are allowed to be negative, each step involving a transition to a negative value is rejected. Furthermore it is possible to abandon the analytical constraint Eq. (6.11) and replace it by a simple logical one[6]; all steps involving a transgression of the homogeneous current are rejected. If no logical constraint is violated, the new Lagrangian value is calculated and the Lagrangian shift is determined. Following the metropolis algorithm Eq. (4.19) steps are accepted or rejected.

4. The total Monte Carlo step is executed for each segment current and Lagrange parameter.

5. A number of MCSs, which leads to a fast convergence is found: $N_{\mathrm{MCS}} = 2000$. After that, the temperature parameter $\beta_{t+1} = \beta_t + \Delta\beta$, as well as the maximal step range $\Delta i_{t+1} = \Delta\lambda_{t+1} = \xi \cdot \Delta i_t$ is adjusted.

6. In all temperature steps β_t the mean value of each segment current

$$\left\langle \vec{i}_{\mathrm{seg}} \right\rangle_{\beta_t} \tag{6.21}$$

and the deviation to the corresponding mean value of the previous temperature step

$$\Delta\vec{i}_{\mathrm{seg}} = \vec{i}_{\mathrm{seg}} - \left\langle \vec{i}_{\mathrm{seg}} \right\rangle_{\beta_{t-1}} \tag{6.22}$$

---

[6]As a Monte Carlo step includes the shift of each variable, the computing time increases linear with the number of Lagrange parameters. Whereas logical constraints lead to a lower step acceptance rate, and thus to a slower convergence. Nevertheless most of the time logical constraints are preferable, due to lower overall computation time.

is calculated. To ensure the statistical independence of each contribution, the values are only updated at each fiftieth MCS. If the mean quadratic deviation to the previous temperature step

$$\left\langle (\Delta \vec{i}_{\text{seg}})^2 \right\rangle_{\beta_t} = \left\langle \left(\vec{i}_{\text{seg}} - \left\langle \vec{i}_{\text{seg}} \right\rangle_{\beta_{t-1}} \right)^2 \right\rangle \tag{6.23}$$

is smaller than a limit $\Delta i_{\text{lim}} = 10^{-15}$, the iteration is terminated and the latest segment-current mean values form the converted configuration $\vec{i}_{\text{seg|conv}}$.

7. As mentioned in the previous section the voltage change ΔU is calculated (c.f. Eq. (6.13)) and based on this the segment currents are adapted to the total current I_0 (c.f. Eq. (6.14)).

6.3 Inverse computations I : Damage extent

In the first part of the computations the Lagrangian has the following form:

$$
\begin{aligned}
L(i_{\text{seg},n}, \lambda_\nu) = \ & \sum_{n=1}^{N_{\text{seg}}} ln((i_{\text{seg},n} - i_0)^2 + \epsilon) \\
& + \lambda_1 \cdot \left[\left(\mathcal{A} - \tfrac{1}{I_0} \vec{i}_{\text{S}} \right) \vec{i}_{\text{seg}} \right]^2
\end{aligned}
\tag{6.24}
$$

No maximal damage segment is predefined here, therefore Eq. (6.18) is not included in the Lagrangian. Furthermore the $i_{\text{seg}} \leq i_0$ constraint is implemented logically. Thus only one Lagrange parameter is needed, which limits the number of variables to $N_{\text{seg}} + 1$. To investigate the solutions in dependency of the allowed damage extent, the saddle point for various ϵ values is determined. Therefore, the annealing program is executed for ϵ values between 10^{-2} and 10 (100), while for each order of magnitude nine computations are performed $\epsilon = \{0.01\ 0.02\ \ldots\ 0.09\ 0.1\ 0.2 \ldots 10\}$. For the sake of compatibility the input vector $\vec{i}_{\text{S,input}}$ is calculated by the multiplication of a given segment current vector $\vec{i}_{\text{seg}}^{\,*}$ with the corresponding transformation matrix:

$$\vec{i}_{\text{S,input}} = \mathcal{A}_{N_{\text{S}}} \cdot \vec{i}_{\text{seg}}^{\,*} \tag{6.25}$$

The transformation matrices for the corresponding number of slits N_{S} has been computed only for PPG 86 graphite plates by the method discussed in section 5.3. It has been shown, that the diagnostic method is applicable for all discussed materials, thus the matrices could be calculated on the basis of other graphite plates as well. The actual values of the matrix elements are of no concern for the selection of inverse problem solutions, as long as the relation between the elements is correct and the bridge currents correspond. Because of this it suffices to investigate the reconstruction for one flowfield material[7].

---

[7]Even the ideal matrix could be used for the investigation of the inverse problem and still the same results would be obtained.

1	2	3
4	5	6
7	8	9

1	2	3	4
5	6	7	8
9	10	11	12
13	14	15	16

Figure 6.2: The segment index for $N_s = 2$ (left) and $N_s = 3$ (right).

For various defect structures these computations are done and the results are discussed. These are done either in an arrangement with two slits or with three slits. Some calculations are done in both arrangement. These are compared to emphasize, that there is no principle difference of an arrangement with $N_S = 2$ and $N_S = 3$ for the inverse problem. Mathematically there is even no difference to arbitrary slit numbers. In the following figures, there is always a sketch of the segment current configuration used in the forward calculation and the solutions of the inverse calculation in dependency of ϵ. The segment index is given in reference to Fig. (6.2) It should be clarified, that each point in this plot is a converged inverse calculation for a given ϵ and a given bridge current vector $\vec{i}_S$.

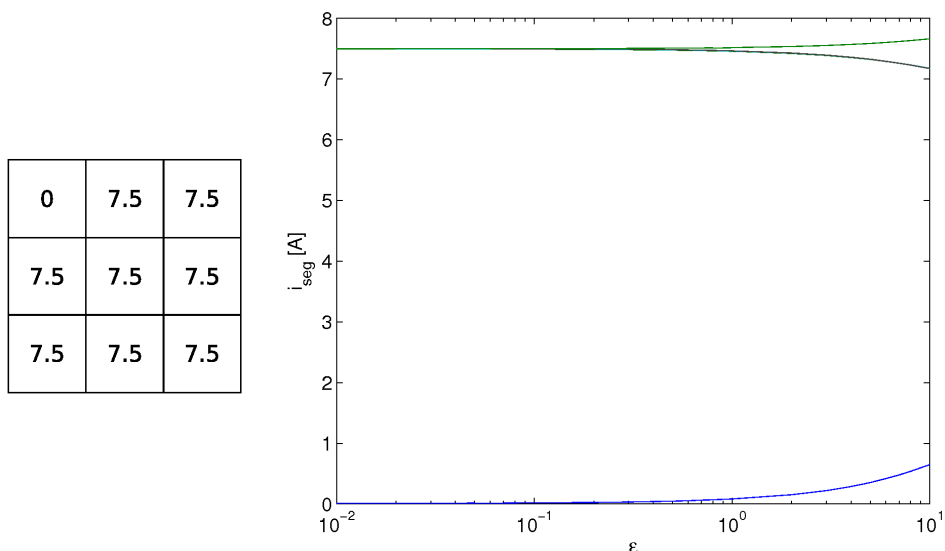| 0 | 7.5 | 7.5 |
| 7.5 | 7.5 | 7.5 |
| 7.5 | 7.5 | 7.5 |

Figure 6.3: The left sub-figure shows the predefined slit current configuration, which is used in the forward calculation. The right sub-figure shows the results of the corresponding inverse calculation in dependency of the ϵ parameter. The blue curve represents the current across the defect segment $n = 1$. The black curve represents $n = 5, 6, 8, 9$ and the green one respectively $n = 2, 3, 4, 7$.
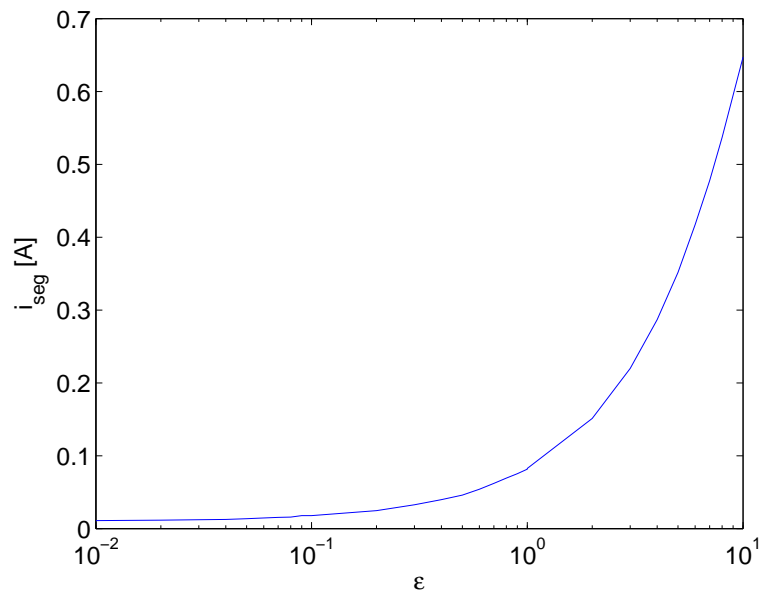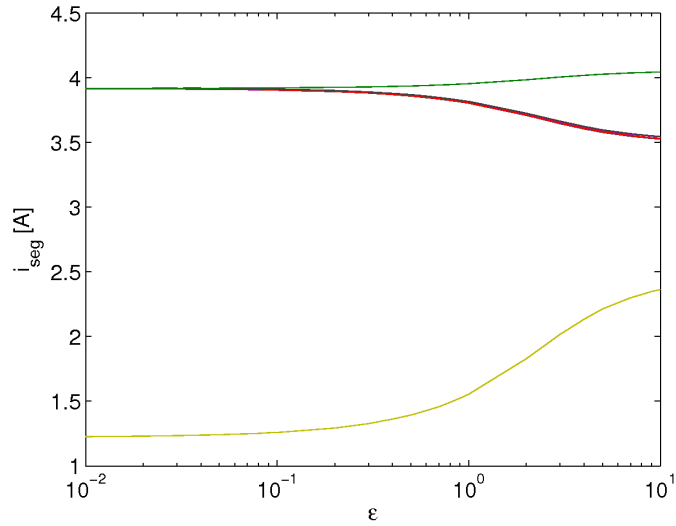

Figure 6.4: The result of the inverse calculation only of the defect segment corresponding to Fig. (6.3).

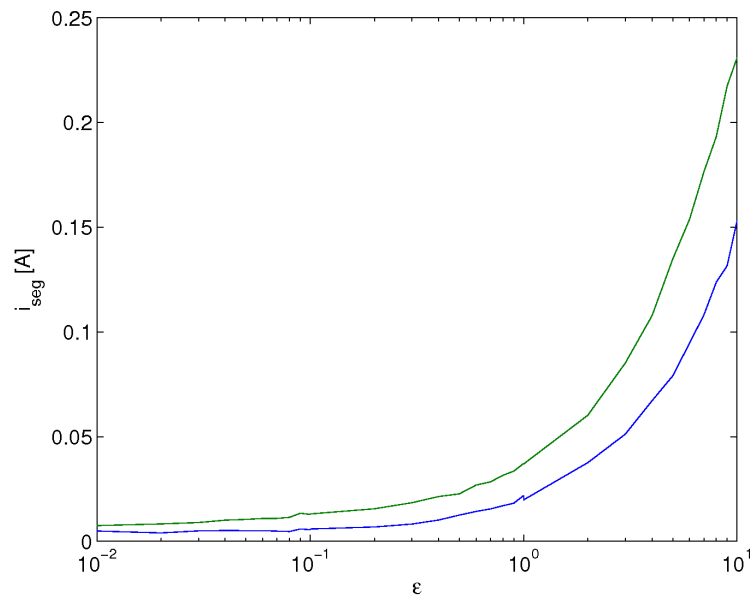| 3.92	3.92	3.92	3.92
3.92	1.2	3.92	3.92
3.92	3.92	3.92	3.92
3.92	3.92	3.92	3.92

Figure 6.5: The left sub-figure shows the predefined slit current configuration, which is used in the forward calculation. The right sub-figure shows the results of the corresponding inverse calculation in dependency of the ϵ parameter. The lower curve represents the current across the defect segment $n = 6$. The descending curve represents $n = 2, 5, 7, 8, 10, 14$. The other segment currents are represented by the green one.

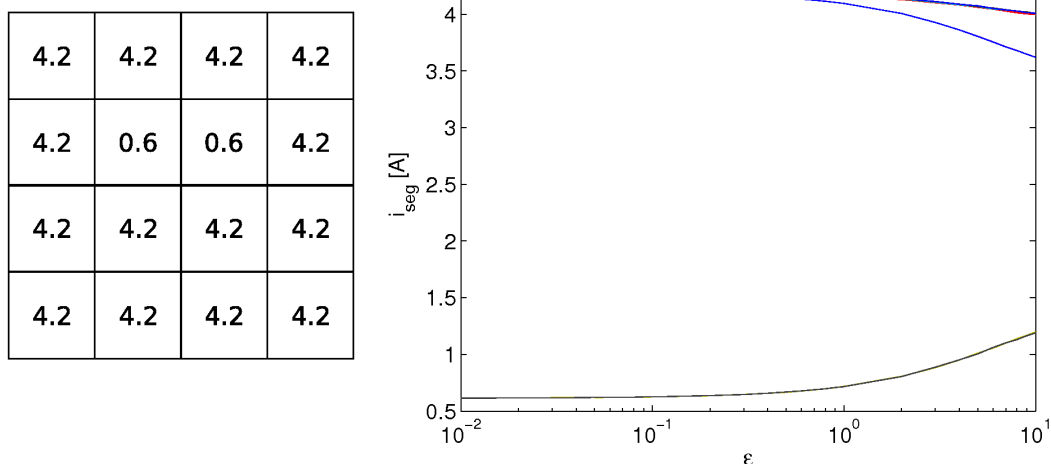| 0	0	8.6
8.6	8.6	8.6
8.6	8.6	8.6

Figure 6.6: The left sub-figure shows the predefined slit current configuration, which is used in the forward calculation. The right sub-figure shows the results of the corresponding inverse calculation in dependency of the ϵ parameter. In this plot only the currents across the two defect segments are shown (blue: $n = 1$, green: $n = 2$).

Figure 6.7: The left sub-figure shows the predefined slit current configuration, which is used in the forward calculation. The right sub-figure shows the results of the corresponding inverse calculation in dependency of the ϵ parameter. The lower curve is in fact two curves representing both defect segments. The topmost curve represents $n = 1, 4, 9, 12, 13, 16$, the second curve $n = 2, 3, 10, 11, 14, 15$ and the blue one $n = 5, 8$.
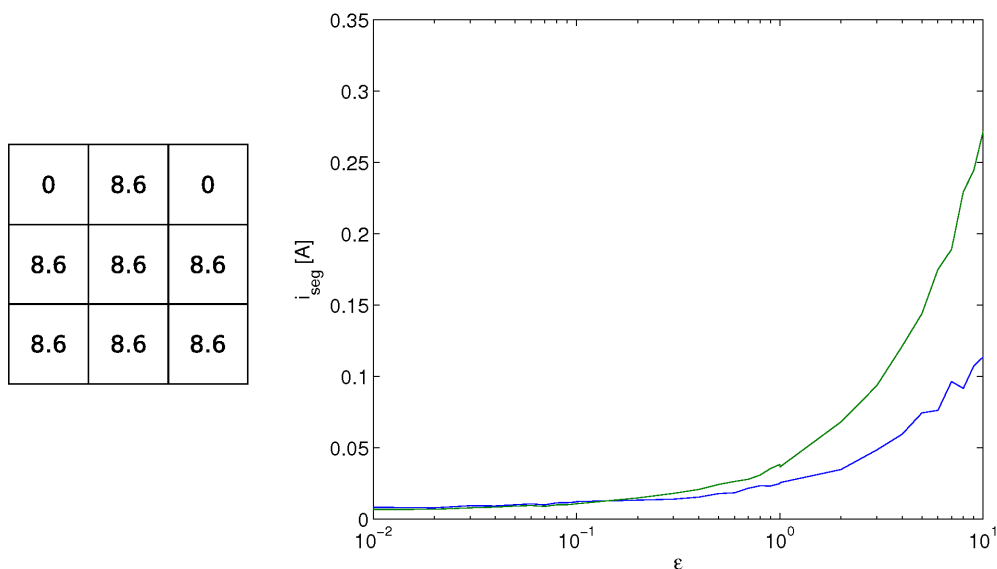

Figure 6.8: The left sub-figure shows the predefined slit current configuration, which is used in the forward calculation. The right sub-figure shows the results of the corresponding inverse calculation in dependency of the ϵ parameter. In this plot only the currents across the two defect segments are shown. The blue curve represents $n = 1$ and the green one $n = 3$.

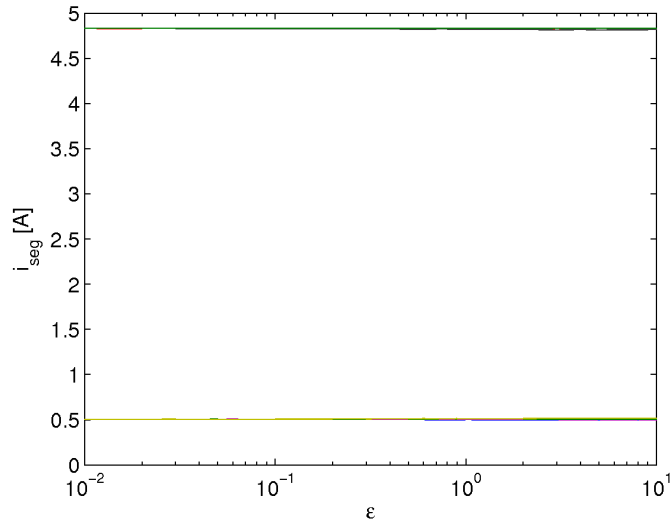| 0.5 | 4.8 | 4.8 | 4.8 |
0.5	4.8	4.8	4.8
0.5	4.8	4.8	4.8
0.5	4.8	4.8	4.8

Figure 6.9: The left sub-figure shows the predefined slit current configuration, which is used in the forward calculation. The right sub-figure shows the results of the corresponding inverse calculation in dependency of the ϵ parameter. The lower curve represents the defect segments and the upper one the undamaged segments.

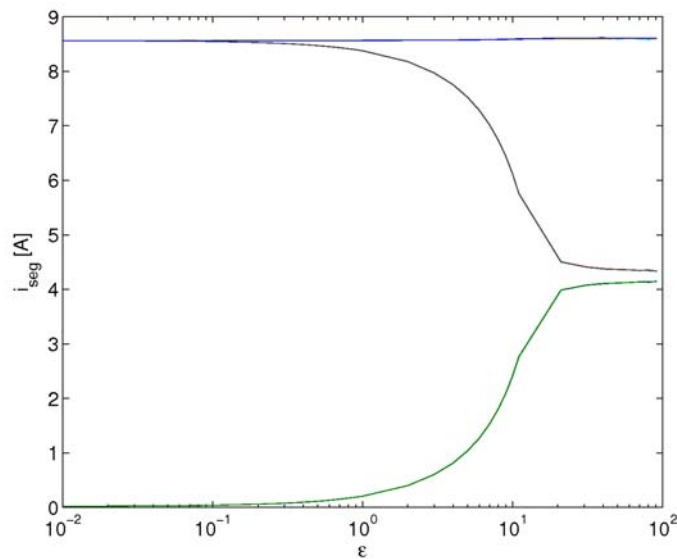| 0 | 8.6 | 8.6 |
| 8.6 | 8.6 | 8.6 |
| 8.6 | 8.6 | 0 |

Figure 6.10: The left sub-figure shows the predefined slit current configuration, which is used in the forward calculation. The right sub-figure shows the results of the corresponding inverse calculation in dependency of the ϵ parameter. The lower green curve includes both $n = 1$ and $n = 9$, the black curve decreasing to $i_{seg} \approx 4\,A$ includes both $n = 3$ and $n = 7$. All other segment currents are represented by the constant curve.

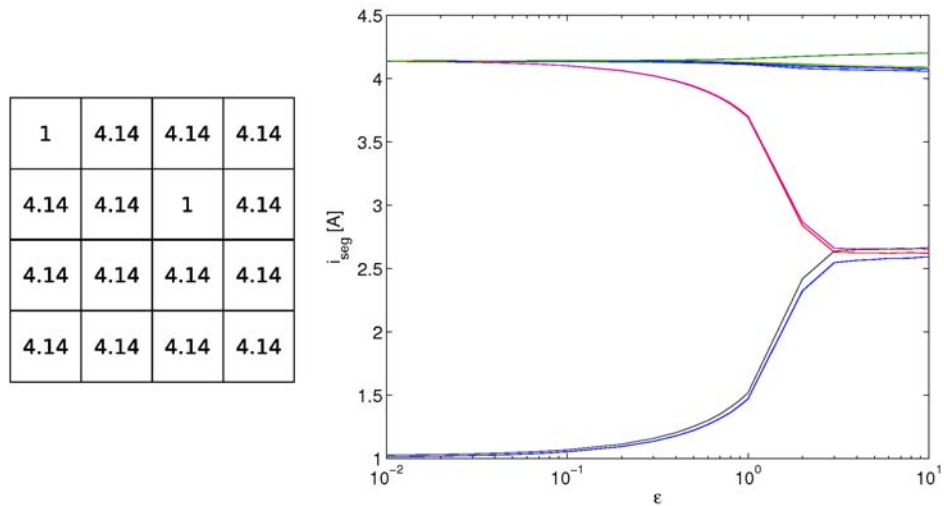| 1 | 4.14 | 4.14 | 4.14 |
4.14	4.14	1	4.14
4.14	4.14	4.14	4.14
4.14	4.14	4.14	4.14

Figure 6.11: The left sub-figure shows the predefined slit current configuration, which is used in the forward calculation. The right sub-figure shows the results of the corresponding inverse calculation in dependency of the ϵ parameter. The two lower curves are $n = 1$ and $n = 7$, whereas the decreasing curves represent $n = 3$ and $n = 5$. All other segment currents are represented by the nearly constant curve.

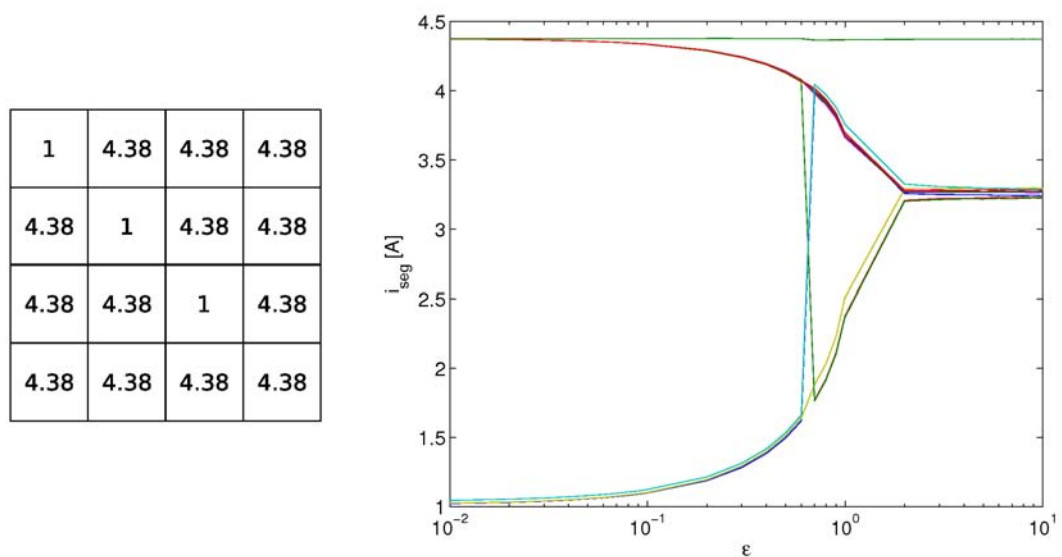| 1 | 4.38 | 4.38 | 4.38 |
4.38	1	4.38	4.38
4.38	4.38	1	4.38
4.38	4.38	4.38	4.38

Figure 6.12: The left sub-figure shows the predefined slit current configuration, which is used in the forward calculation. The right sub-figure shows the results of the corresponding inverse calculation in dependency of the ϵ parameter. The two lower curves stepping up are $n = 1$ and $n = 11$, the curves stepping down are $n = 3$ and $n = 9$. The not stepping lower curve is $n = 6$. Also the curves $n = 2, 5, 7, 10$ are converging to $i_{seg} = 3.7\,A$. All other segment currents are represented by the constant curve.

The simplest defect is a single completely damaged segment. The results for this
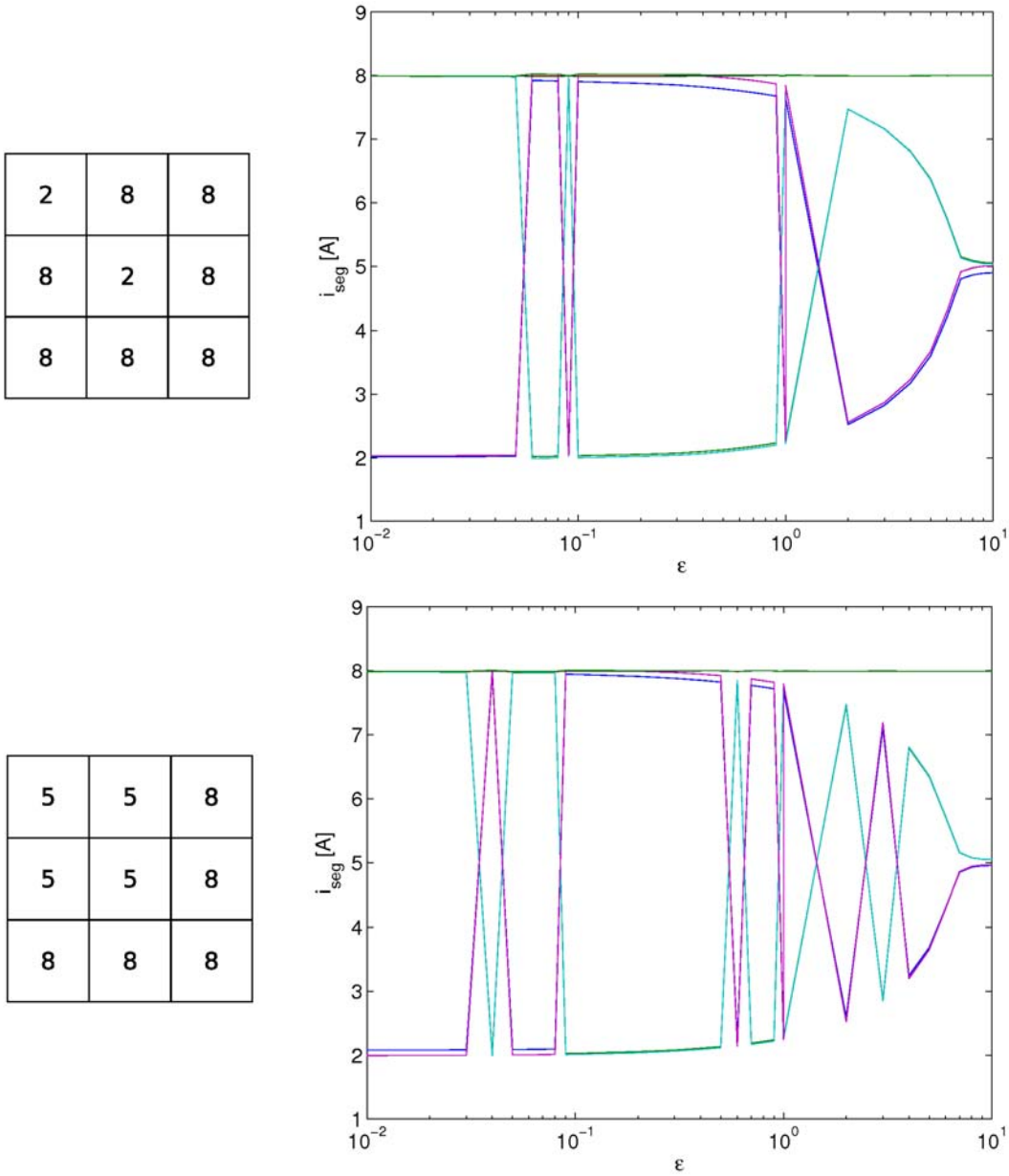
Figure 6.13: Comparison between a block like defect and a diagonal defect. The left sub-figures show the predefined slit current configuration, which is used in the forward calculation. The right sub-figures show the results of the corresponding inverse calculation in dependency of the ϵ parameter. In both plots the curve pairs interchanging their positions are on the one hand $n = 1, 5$ and on the other hand $n = 2, 4$. All other segment currents are represented by the constant curve.

configuration are shown in Fig. (6.3) and the defect segment current individually in Fig. (6.4). First of all the conformity between the given configuration and the recalculated one is considerable. The segment currents are in fact completely reconstructed of the bridge currents. Furthermore it is obvious, that the result improves for small ϵ values. This can be explained by the extent of the given defect. As it is concentrated in only one segment, there can be no stronger defect localization for a given N_{S}. Thus, the larger the penalty for unlocalized solutions, which is conformal with a small ϵ, the better the localized solution reconstructed. At large ϵ values, the solution diverges from the predefined one, as less localized solutions are accepted as well. In fact the defect current increases whilst the segment currents in the same stripe as the defect decreases. In Fig. (6.5) a more general variant of the same damage is shown. Here a finite damage occurs at an arbitrary position. Nevertheless, the $i_{\mathrm{seg}}(\epsilon)$ plot shows the same qualitative result and the predefined configuration is reconstructed perfectly. These two results show, that each damage being smaller than one segment can be reconstructed loss-less.

In Fig. (6.6) and Fig. (6.7) there are two examples for a defect, which extends over two adjacent segments. As this kind of damage is also a localized one, it shows an equivalent behavior and therefore it is possible to reconstruct it either. In Fig. (6.6) the values of the two damaged segments increase distinct, whereas in Fig. (6.7) both curves are exactly equal. This might occur due to symmetry reasons, as the second configuration is more symmetric than the first one. Thus the null space leads to different less localized solutions for increasing ϵ.

In Fig. (6.8) a non local defect is predefined. But this configuration is still restricted, as there are only two damaged segments, which are in addition located on the same stripe in one direction. Although there is again a divergence in the high ϵ domain, the solution converges to the predefined one for small ϵ values. Even though this is not a local defect, it is also loss-less reconstructed. In the following figure, Fig. (6.9) an entire stripe is defect, which is perfectly reconstructed for all ϵ values. In the previous configurations the currents across the segments in the defect slits decreases (except for the defect segments itself), whereas the other segments increases. Since in this configuration there are only segments in defect slits and by following the current conservation, there can be no change in segment currents at high ϵ values.

In the following figures, two different solutions appear, a local one for low ϵ values and a less localized one above these. Although in most of the cases the local solution has been predefined, in one figure (Fig. (6.13)) both configurations are predefined once. In Fig. (6.10) and Fig. (6.11) the configuration consists of two damaged segments in totally different stripes. In both cases the slow transition from the local solution to the less localized one can be seen well. In the minimal localized solution, two other segments have a contribution. These segments are defined by the intersection of the damaged stripes (c.f. Fig. (6.14)). In fact the predefined solution and the solution given by the intersection are degenerated for low ϵ values. This can be seen better in the subsequent figures, since there are obvious jumps between the degenerated solutions.

In Fig. (6.12) the predefined configuration is a diagonal. Here it can be seen very well, that the solution containing the diagonal and the one containing the anti-diagonal are degenerated. As the central segment of the damage structure $n = 6$ is part of
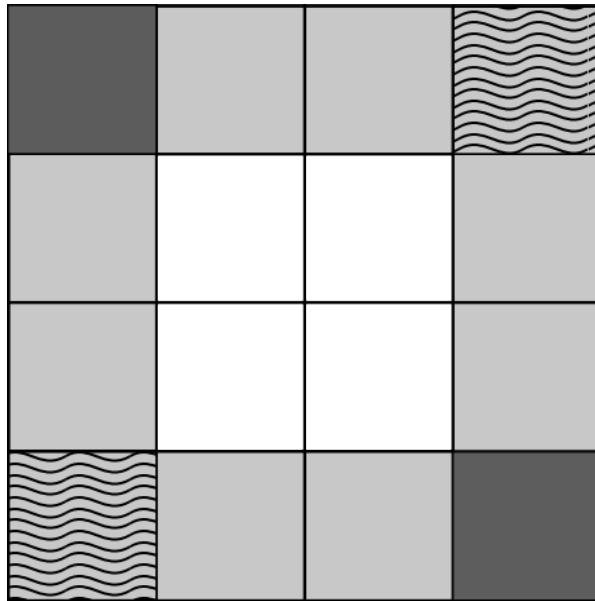
Figure 6.14: Schematically view of degenerated solutions. The defect configuration is indicated by the dark gray segments. The light gray segments are part of stripes, in which an actual defect can be found.. The intersection of these stripes form the degenerated solution (denominated by the wave texture).

both solutions, it does not change in the step. These different solutions appear due to the statistically nature of the simulated annealing method. As the minimum of both solutions are equally deep, the method finds either the one solution or the other one. Thus even more steps could appear in a $i_{\mathrm{seg}}(\epsilon)$ plot. The minimal localized solution does not contain only the diagonal and the anti-diagonal, but all intersections of the predefined segments. Thus at high ϵ a block is reconstructed. The integrated current across this block in both solutions is equal. Therefore one could expect equal curves for a diagonal and a corresponding block with the same integrated current flowing across all participating segments. This is done for a simple two segment diagonal and respectively four segment block. The results are shown in Fig. (6.13). In both configurations the total current across the block is $20\,\mathrm{A}$. The resemblance between both plots is obvious. They only differ in the location and number of steps between the diagonal and the anti-diagonal solution. However, arbitrary numbers of steps can appear for small ϵ values (local damages), these are totally random and the difference can be neglected.

6.4 Inverse computations II : Voltage difference

If one is only interested which segments are definitely undamaged, another presentation of the inverse problem is appropriate. The calculation is done only for one ϵ value, but one segment is defined as the one with the largest damage. In fact this is done for each segment. Due to the large null space, there is always a solution, but the change of

the overall MEA resistance may vary largely. Therefore at the end the relative voltage differences are compared, as they represent the increase in this resistance.

For this calculation the following Lagrangian is used:

$$
\begin{aligned}
L(i_{\mathrm{seg},n}, \lambda_\nu) = \quad & \textstyle\sum_{n=1}^{N_{\mathrm{seg}}} ln((i_{\mathrm{seg},n} - i_0)^2 + \epsilon) \\
& +\lambda_1 \cdot \left[\left(\mathcal{A} - \tfrac{1}{I_0}\vec{i}_{\mathrm{S}} \right) \vec{i}_{\mathrm{seg}} \right]^2 \\
& + \textstyle\sum_{n=1}^{N_{\mathrm{seg}}} \lambda_{n+N_{\mathrm{seg}}+1} \cdot (i_{\max} - i_{\mathrm{seg},n})
\end{aligned}
\tag{6.26}
$$

Again the constant total current constraint is included logically. Though it is more meaningful to include the maximal defect constraint in an analytical way, since a violation of it could also be reversed by lowering the current across the maximal defect segment. If applied logical, this constraint would increase the convergence time immensely, as no transgression across the variable lower limit is permitted. For some of the previous discussed configurations this presentation scheme is applied.

The information obtained from these figures contains which segments are definitely undamaged, and which segment might be damaged. In Fig. (6.15) and Fig. (6.16) configurations are used, which can be reconstructed uniquely. The relative voltage change for the damaged segments is clearly lower than for the other segments. This means, that a damage, which is maximal at these locations, can be very local and still reproduce the measured bridge currents. In Fig. (6.17) and Fig. (6.18) there are configurations chosen, which lead to degenerated solutions in the inverse calculation. Again it can be clearly seen in which segments the damage may have been occurred.

Since the number of unknown segment currents in the MEA N_{seg} is much larger than the number of signals N_{cur}, a lot of information about the MEA condition is lost, if only the bridge currents are measured. Though it is much less complicated to measure only the currents emerging at the bridges. If a local damage occur, the MEA condition can be reconstructed with a good accuracy. Therefore is seems, that only minor information is lost and the MEA condition is adequately represented by the bridge currents.

0	7.5	7.5
7.5	7.5	7.5
7.5	7.5	7.5

12.5%	51.5%	51.1%
51.4%	61.5%	50.5%
51.1%	44.4%	45.2%

Figure 6.15: The left sub-figure shows the predefined slit current configuration, which is used in the forward calculation. The right sub-figure shows the results of the corresponding inverse calculation for $\epsilon = 0.1$. The percental values represents the voltage change, if the corresponding segment is assumed to have the maximal damage.

0	0	8.6
8.6	8.6	8.6
8.6	8.6	8.6

28.5%	28.5%	68.7%
71.3%	71.7%	152.5%
75.2%	72.9%	158.3%

Figure 6.16: The left sub-figure shows the predefined slit current configuration, which is used in the forward calculation. The right sub-figure shows the results of the corresponding inverse calculation for $\epsilon = 0.1$. The percental values represents the voltage change, if the corresponding segment is assumed to have the maximal damage.

0	8.6	8.6		28.5%	73.7%	29.5%
8.6	8.6	8.6		72.8%	72.5%	72.4%
8.6	8.6	0		29.5%	72.5%	28.5%

Figure 6.17: The left sub-figure shows the predefined slit current configuration, which is used in the forward calculation. The right sub-figure shows the results of the corresponding inverse calculation for $\epsilon = 0.1$. The percental values represents the voltage change, if the corresponding segment is assumed to have the maximal damage.

5	5	8		20.0%	20.1%	48.1%
5	5	8		20.1%	19.9%	48.8%
8	8	8		49.2%	48.7%	52.4%

Figure 6.18: The left sub-figure shows the predefined slit current configuration, which is used in the forward calculation. The right sub-figure shows the results of the corresponding inverse calculation for $\epsilon = 0.1$. The percental values represents the voltage change, if the corresponding segment is assumed to have the maximal damage.

7 Conclusion

For graphite flowfield plates it has been shown, that by placing slitted 1mm aluminum plates between the flowfield plates of adjacent fuel cells in a stack - which elongates a 100 cell stack by about 10 cm - it is possible to localize damaged areas in the MEAs of the fuel cells and to determine how serious the damage is. This is made possible by enforcing inner compensation currents to appear at the surface of the stack where they can be measured. All computations testing the measurability of the bridge currents including various graphite flowfield materials have been positive. For most of these materials it is even possible to reduce the aluminum plate thickness. For PPG 86 it is even possible to reduce it to less than $100 \, \mu$m. In a fuel cell with BBP 4 graphite flowfields the insertion of slitted 0.5 mm thick aluminum plate suffices to measure the bridge currents satisfactorily.

Furthermore it is possible to smoothen inhomogeneities of currents in the MEAs and prevent irregularities in one MEA to induce irregularities in the MEAs of the next and previous fuel cell which otherwise could lead to a destructive chain reaction. The defect expansion in the damaged MEA due to current density peaks at the defect-boundary is also prevented completely.[1] A further, not investigated, secondary effect of the aluminum plate is the equalization of temperature peaks, which also could damage the fuel cells. Since the thermal conductivity of aluminum is also very high ($2.37 W \cdot (cm \cdot K)^{-1}$ at 300K), thermal irregularities are smoothed out, too.

For the reconstruction of the MEA condition it has been shown, that it is possible to define a Lagrangian in such a way, that solutions concerning specific defect structures can be found. In fact, using a simple Lagrangian preferring local solutions a large variety of defects can be reconstructed. Investigating typical damages occurring in fuel cells it seems that most of them are local and by that reconstructible.

- Flooding of cathode flowfields: If water is deposited in the cathode flowfield, it blocks complete channels. Usually the channels are parallel to one slit direction, therefore the defect is limited to one stripe and can be reconstructed.

- Flooding of the diffusion layer: This flooding effect is not bound to a flowfield channel, but as long as it is connected, its location can be determined (c.f. Fig. (7.1)).

---

[1] This is actually not investigated for thinner aluminum plates. Though an approximation for a $100 \mu m$ aluminum plate in between two $1mm$ PPG 86 plates leads to a conductance one order of magnitude larger than that of a $2mm$ Sigraflex plate of the same width and length. Thus the inhibition of the damage expansion is expected to be still almost perfect.
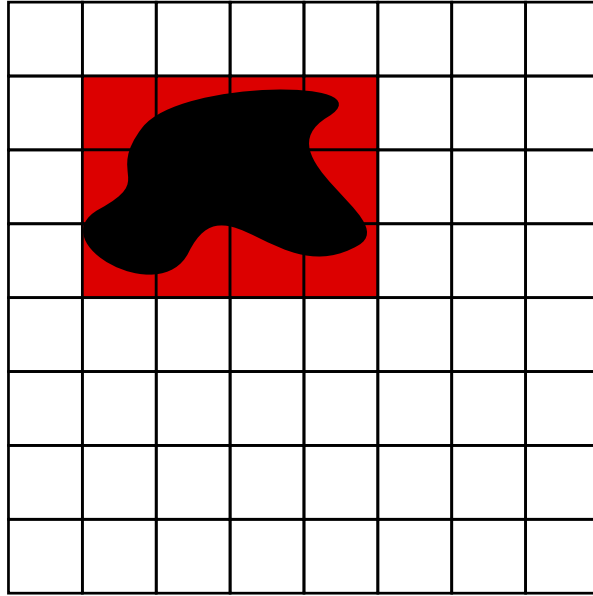
Figure 7.1: For large numbers of slits (here $N_s = 7$) it is also possible to reconstruct MEA failures. Complex defects (black structure) would be reconstructed as a damage spread over the red segments.

- Oxidizing of the catalyst and destruction of the membrane: Both effects may appear at different locations of the MEA and are thus not necessarily connected. But as long as they do not emerge exactly at the same time, it is possible to detect them independently.

Of course more than one defect may occur in the same MEA, but as long as they emerge at different times it is possible to detect one by one measuring the current difference at the bridges. Fig. (7.1) shows an exemplary defect and its reconstruction by the presented diagnostic scheme. In order to verify the theoretical and numerical results experiments will be done in the near future.

A Appendix

A.1 Finite-volume conductivity in material interfaces

In reference to Fig. (A.1) the current density j between x_1 and x_2 is calculated to quantify the conductivity at the location x_0. This can be done by the Ohm's law

$$j = \frac{\phi_2 - \phi_1}{\rho} \tag{A.1}$$

where ρ is the area related resistivity. If objects with identical cross sections are connected in series, it is possible to add up the individual resistivities to obtain the total one. According to the prerequisites of the finite-volume method, the connecting surfaces of adjacent cells are of the same size. Hence it is possible to calculate the total resistivity by the sum of the individual ones:

$$\rho = \rho_1 + \rho_2 = \frac{x_0 - x_1}{\sigma_1} + \frac{x_2 - x_0}{\sigma_2} \tag{A.2}$$

If the two cells are of the same size, the distances are equal and can be written as $x_0 - x_1 = x_2 - x_0 = l$, which leads to:

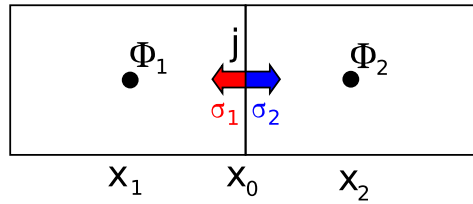$$\rho = 2 \cdot l \left(\frac{1}{2} \left(\frac{1}{\sigma_1} + \frac{1}{\sigma_2} \right) \right) \tag{A.3}$$

Figure A.1: The two adjacent cells with the potentials ϕ_1 and ϕ_2 have different conductivities, which are unambiguously defined at the locations x_1 and x_2. The unknown conductivity, which is needed for the calculation of the current density j between ϕ_1 and ϕ_2, is located at x_0.

Combining Eq. (A.3) with Eq. (A.1) leads, under the consideration that $2 \cdot l$ is the distance from x_1 to x_2, to:

$$j = 2 \left(\frac{1}{\sigma_1} + \frac{1}{\sigma_2} \right)^{-1} \cdot \frac{\phi_2 - \phi_1}{x_2 - x_1} \tag{A.4}$$

The second term on the right hand side of the equation is the difference quotient of the potential derivative, and the prefactor is the harmonic mean value σ_{h} of the conductivities in the two cells[1]. The resemblance between Eq. (A.4) and the canonical approximation Eq. (4.11) is obvious, whereas the harmonic mean value is used for the conductivity at the material interface. In this manner the current density between these two cells is calculated correctly.

A.1.1 The electric field at material interfaces

Due to Ohm's law $j = \sigma \cdot E$, the conductivity step at x_0 and the uniformity of the current density, follows a step in the electric field at x_0. With a known current density j it is possible to determine the electric field in the two adjacent cells:

$$E_1 = \frac{j}{\sigma_1} \qquad\qquad E_2 = \frac{j}{\sigma_2} \tag{A.5}$$

As the conductivity within a cell is constant, the electric field is constant, too. Thus, the potential increases linear with a slope of $-E$, and has a step at x_0. The progression of the potential, indicated in Fig. (A.2), suggests a linear characterization:

$$\phi(x) = \phi(x_1) + (x - x_1) \cdot E_1, \;\; x \leq x_0 \tag{A.6}$$
$$\phi(x) = \phi(x_2) + (x - x_2) \cdot E_2, \;\; x \geq x_0$$

If these two equations are consistent, the potential can by quantified completely without any further approximations. The consistency is shown if both equations yield the same value for $x = x_0$:

$$\begin{aligned} \phi(x_0)_{x \leq x_0} &= \phi(x_0)_{x \geq x_0} \\ \phi(x_1) + (x_0 - x_1) \cdot E_1 &= \phi(x_2) + (x_0 - x_2) \cdot E_2 \\ \phi(x_2) - \phi(x_1) &= (x_0 - x_1) \cdot E_1 + (x_2 - x_0) \cdot E_2 \end{aligned} \tag{A.7}$$

With $x_0 - x_1 = x_2 - x_0 = l$ and $E = j/\sigma$ follows:

$$\phi(x_2) - \phi(x_1) = 2 \cdot l \cdot j \left(\frac{1}{2\sigma_1} + \frac{1}{2\sigma_2} \right) \tag{A.8}$$

---

[1]If the two cells are of different size, the harmonic mean value of the conductivities is given by $\sigma_{\mathrm{h}} = \frac{1}{x_2 - x_1} \left(\frac{x_0 - x_1}{\sigma_1} + \frac{x_2 - x_0}{\sigma_2} \right)^{-1}$
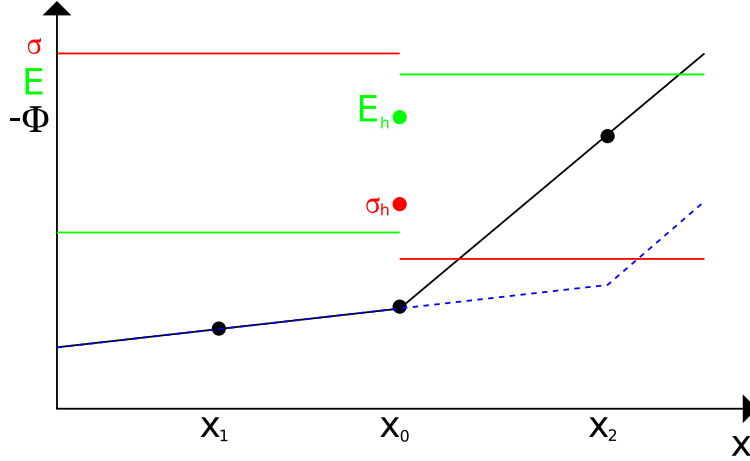
Figure A.2: Qualitative sketch of the conductivity σ, the electric field E and the electric potential ϕ in the vicinity of a material interface at x_0. The conductivity, as well as the electric field are constant in both cells, but have a step at the interface. Their values at x_0 due to the harmonic mean value, σ_h and E_h, are shown as dots. The potential ϕ increases constantly with a discontinuity at the interface x_0. The dashed blue line indicates the potential progression, if the conductivity of the first cell had been used instead of the harmonic mean value.

$$\left(\frac{1}{2\sigma_1} + \frac{1}{2\sigma_2}\right)^{-1} \frac{\phi(x_2) - \phi(x_1)}{2 \cdot l} = j \tag{A.9}$$

This shows, that the linear description of the potential is only valid if the harmonic mean value for the conductivity is used. Thus, the finite-volume method can include conductivity steps even of high magnitude if the harmonic mean value for the boundary conductivity is used.

A.2 Finite-volume method for the magnetic field

Using the finite-volume method, it is possible to calculate the magnetic field in a body Ω consistently. To do that a differential equation for the magnetic vector potential $\vec{A}$ is assembled. This is done on the basis of the following two equations:

$$rot\,\vec{A} = \vec{H} \tag{A.10}$$

$$rot\,\vec{H} = \vec{j} \tag{A.11}$$

Eq. (A.10) is the calibration of the magnetic vector potential, and Eq. (A.11) is the time independent Ampere's law. Both equations are treated analogously by applying a surface integral. This calculation can not be done in two dimensions since the curl
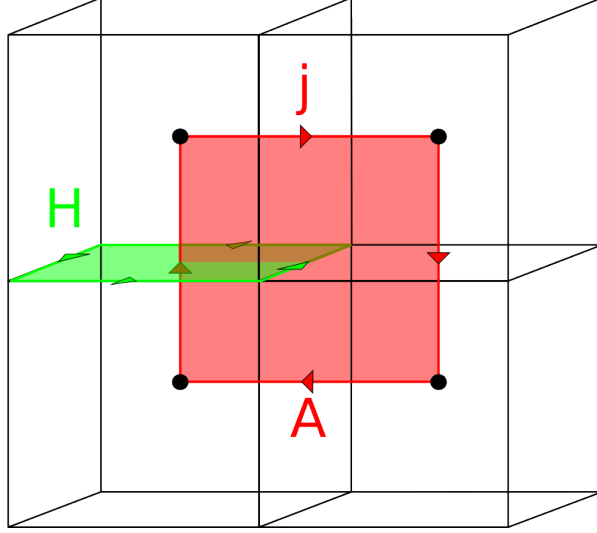
Figure A.3: The electric potential ϕ is defined at the black dots in the center of the cell. The current density $\vec{j}$ and the magnetic vector potential $\vec{A}$ are defined at the location of the red arrows at the face center of each cell. The magnetic field $\vec{H}$ is defined at the location of the green arrows in the middle of each lateral edge.

operator (rot) is only defined in three dimension. For Eq. (A.11) this leads to:

$$\int_F rot\,\vec{H} \cdot \vec{n}dF = \int_F \vec{j} \cdot \vec{n}dF \tag{A.12}$$

Here $\vec{n}$ denotes the normal vector of the surface F. The Stokes integral theorem[39] is used to substitute the surface integral of $rot\,\vec{H}$ by a line integral of $\vec{H}$ over the boundary of the surface ∂F:

$$\int_{\partial F} \vec{H}dl = \int_F \vec{j}_n dF \tag{A.13}$$

The line of integration ∂F is indicated by the green line in Fig. (A.3), while the magnetic field is defined at each lateral edge. On the right hand side of the equation only the current density components normal to the green area have a contribution to the integral. These can be calculated by the canonical approximations Eq. (4.11). By identifying the electric potential of the bottom left cell by $\phi_{ijk}{}^2$, this leads to the discretized form of Eq. (A.13):

$$
\begin{aligned}
j_{\mu,\nu,\kappa+1/2} \cdot h_x \cdot h_y \;\; = \;\; & \left(H_{x|\mu,\nu-1/2,\kappa+1/2} - H_{x|\mu,\nu+1/2,\kappa+1/2} \right) h_x \\
+ \; & \left(H_{y|\mu+1/2,\nu,\kappa+1/2} - H_{y|\mu-1/2,\nu,\kappa+1/2} \right) h_y
\end{aligned}
\tag{A.14}
$$

---

[2]Since this calculation is done in three dimensions, the potential ϕ has three indices.
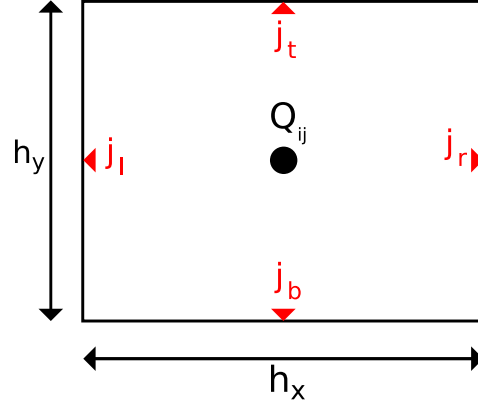
Figure A.4: The charge inside of a cell is defined at the center, likewise to the electric potential. The current density is defined at the face centers.

The application of the Stokes integral theorem to Eq. (A.10) leads to:

$$\int_{\partial F_2} \vec{A} dl_2 = \int_{F_2} \vec{H}_n dF_2 \tag{A.15}$$

∂F_2 is the red line in Fig. (A.3) and respectively F_2 the red area. Thus follows the canonical approximation of the magnetic field:

$$
H_{y|\mu+1/2,\nu,\kappa+1/2} \cdot h_x \cdot h_y \;=\; \begin{aligned}
& \left(A_{x|\mu+1/2,\nu,\kappa+3/2} - A_{x|\mu+1/2,\nu,\kappa} \right) h_x \\
+\; & \left(A_{z|\mu,\nu,\kappa+1/2} - A_{z|\mu+1,\nu,\kappa+1/2} \right) h_y
\end{aligned} \tag{A.16}
$$

Each component of H in Eq. (A.14) is replaced by the corresponding vector potential term Eq. (A.16). Thus, a differential equation for the magnetic vector potential A with the current densities $j_{\mu\nu\kappa}$ as an inhomogeneity is obtained. From a known vector potential $\vec{A}$ the magnetic field $\vec{H}$ can be calculated using Eq. (A.10).

A.3 Maxwell equations in the finite-volume method

The major advantage of the finite-volume method is, that it fulfills all Maxwell equations. The static Ampere's law $rot\,\vec{H} = \vec{j}$ is fulfilled by default, as it is directly used in the assembling of the differential equations Eq. (A.14) and Eq. (A.16).

Gauss law The finite-volume method does not fulfill the Gauss law by default, as no charges are defined. To add the Gauss law

$$\oint \vec{E} d\vec{S} = Q \tag{A.17}$$

with the included charge Q and the enclosing surface $\vec{S}$, to the finite-volume method, the charge density has to be discretized. Since the electric field is defined at the face centers of the cells (like the current density) it is appropriate to define the total charge at the center of the cells. After the electric field is substituted by the negative potential gradient, the charge Q_{ij} can be calculated analogously to Eq. (4.10). If Eq. (4.5) is solved and the potential as well as the current density distribution is known, it is possible to calculate the charge as a function of the current density and of the conductivity. In two dimensions (c.f. Fig. (A.4)) the charge is given by:

$$Q_{ij} = \frac{j_\mathrm{l}}{\sigma_\mathrm{l}} h_y - \frac{j_\mathrm{r}}{\sigma_\mathrm{r}} h_y + \frac{j_\mathrm{b}}{\sigma_\mathrm{b}} h_x - \frac{j_\mathrm{t}}{\sigma_\mathrm{t}} h_x \tag{A.18}$$

In an isotropic material all conductivities are equal, thus this equation is reduced to the sum over all surface currents, which must vanish. In an anisotropic material this equation does not vanish even though the sum over the surface currents does. Therefore inside of isotropic materials no charges occur, whereas inside of anisotropic materials charges may occur. At material interfaces charges can definitely be found. This is due to the harmonic mean value of the conductivity, which leads to an anisotropic conductivity in surface cells, even in isotropic materials. Although there may be no contribution to Eq. (A.18) in the direction parallel to the interface, the perpendicular components differ. If the interface is at the right side of cell Q_{ij}, σ_b may be equal to σ_t, but σ_r is given by the harmonic mean value and is thus different to σ_l. In the time independent case, the charge density does not change. Therefore current conservation in the form $div \, \vec{j} = 0$ is still fulfilled, and the emergence of charges can be ignored if electrostatic or magnetostatic boundary problems are solved. Nevertheless, after the boundary problem is solved, the charge can be calculated consistently by the Gauss law Eq. (A.17).

Faraday's law   The observance of the static Faraday's law $\oint \vec{E} \, d\vec{s} = 0$ can be shown easily. Fig. (A.5) shows a closed line along which the electric field is integrated. The time independent Faraday's law demands this integral to vanish. This is shown for a line of integration across a material interface; if the line integral vanishes at the interface, it vanishes all the more for closed lines inside of one material. As the electric field has a step at material interfaces the integrations from ϕ_1 to ϕ_2 and from ϕ_3 to ϕ_4 are separated. For the electric field at the interface Eq. (A.5) and Eq. (A.4) is used:

$$\int \vec{E_1} d\vec{s} = \sigma_\mathrm{h} \frac{\phi_2 - \phi_1}{\frac{1}{2} d_x \sigma_1} d_x + \sigma_\mathrm{h} \frac{\phi_2 - \phi_1}{\frac{1}{2} d_x \sigma_2} d_x \tag{A.19}$$

$$\int \vec{E_3} d\vec{s} = \sigma_\mathrm{h} \frac{\phi_4 - \phi_3}{\frac{1}{2} d_x \sigma_1} d_x + \sigma_\mathrm{h} \frac{\phi_4 - \phi_3}{\frac{1}{2} d_x \sigma_2} d_x \tag{A.20}$$

The electric field E_2 and E_1 are once again approximated in the canonical form:

$$\oint E \, ds = 2\sigma_\mathrm{h} \left(\frac{1}{\sigma_1} + \frac{1}{\sigma_2} \right) \phi_2 - \phi_1 + 2\sigma_\mathrm{h} \left(\frac{1}{\sigma_1} + \frac{1}{\sigma_2} \right) \phi_4 - \phi_3 + \phi_1 - \phi_4 + \phi_3 - \phi_2 \tag{A.21}$$
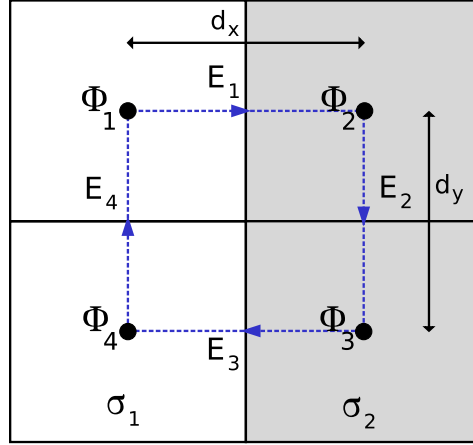
Figure A.5: The line integral of the electric field over a closed line vanishes, even at a material interface. This also holds in the finite-volume discretization. The electric field is integrated clockwise along the blue line. The different shaded cells indicate different conductivity.

With the harmonic mean value $\sigma_h = 0.5(1/\sigma_1 + 1/\sigma_2)^{-1}$ this leads to:

$$\oint E\, ds = \phi_2 - \phi_1 + \phi_4 - \phi_3 + \phi_1 - \phi_4 + \phi_3 - \phi_2 = 0 \tag{A.22}$$

Thus it is proved, that the static Faraday's law holds in the finite-volume discretization.

Gauss law for the magnetic field The magnetostatic Gauss law demands the solenoidality of the magnetic field $\oiint \vec{H}\, d\vec{S} = 0$. To show this, a different discretization is chosen, in which the magnetic field is defined on the face centers. In this way each magnetic field point represents one face of the cuboid and the closed surface integral can be divided into the sum over six separate surface integrals. The resulting sum is shown for the first two faces:

$$\oiint \vec{H}\, dF = \int_{F_1} H_1 dF + \int_{F_2} H_2 dF + ... \tag{A.23}$$

With Eq. (A.10), and by applying the Stokes integral theorem to each surface integral of $rot\ \vec{A}$, this leads to a sum over line integrals:

$$\begin{aligned}
\oiint \vec{H}\, dF &= \int_{\partial F_1} A_1 dl + \int_{\partial F_2} A_2 dl + ... \\
&= A_{1,1} d_x + A_{1,2} d_z + A_{1,3} d_x + A_{1,4} d_z \\
&\quad + A_{2,1} d_y + A_{2,2} d_z + A_{2,3} d_y + A_{2,4} d_z + ...
\end{aligned} \tag{A.24}$$

As can be seen in Fig. (A.6) $A_{1,2}$ is equal to $-A_{2,4}$ and therefore these two quantities cancel out mutually. Each component of the magnetic vector potential occurs in two
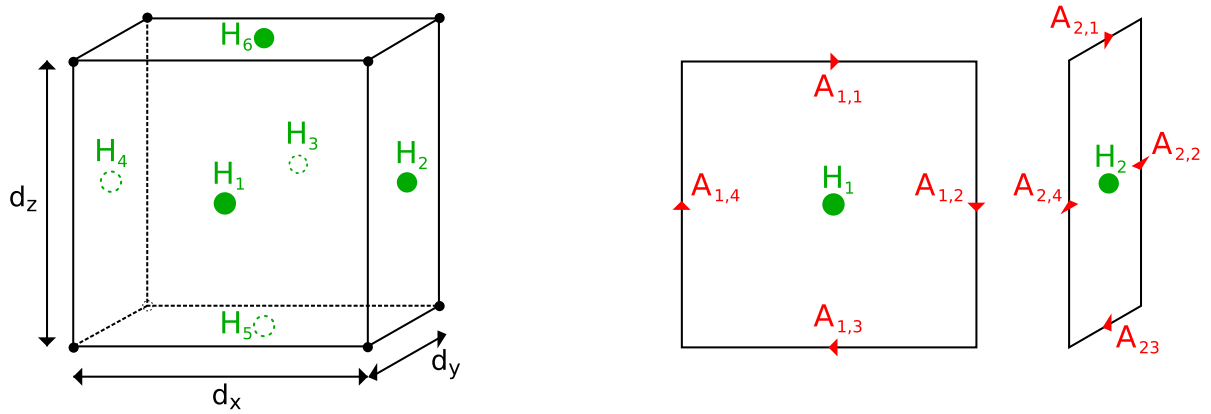
Figure A.6: On the left hand side a cell, in which the magnetic field is discretized on the face centers and the electric potential is discretized in the edges, is shown. On the right hand side the faces corresponding to H_1 and H_2 are shown separately. The red arrows indicates the magnetic vector potential, which are defined on the lateral edges in this discretization.

line integrals, since each edge is boundary of two faces. All integrations are done clockwise, which concludes, that any vector potential component appears once negative and once positive. Thus, the sum over all faces is zero, which shows the observance of the magnetostatic Gauss law by the finite-volume method.

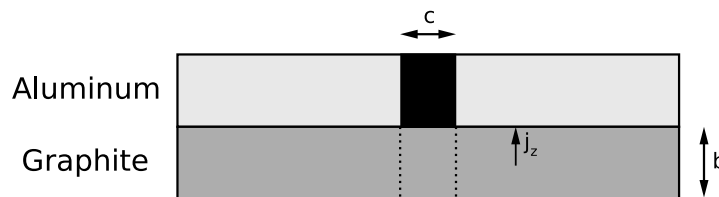## A.4 Circulation resistance approximation

Figure A.7: Schematic view of the graphite aluminum boundary layer at the slit. The slit in the aluminum plate is indicated by the black area. On the top of the aluminum layer there is another not shown graphite plate.

To approximate the circulation resistance R_C via the graphite layer, the system shown in Fig. (A.7) is used. R_C is separated into two domains, the linear domain parallel to the slit and the domain in which the current flows out of and into the aluminum. The

resistance in the parallel domain can easily be calculated by:

$$R_1 = \frac{c}{b \cdot L \cdot \sigma_\perp} \tag{A.25}$$

To determine the potential in the other domain, the Laplace equation

$$\frac{\partial j_x}{\partial x} = -\frac{\partial j_z}{\partial z} \tag{A.26}$$

with $j_y = const. = 0$ is used. The current density derivative in the z-direction is approximated by the difference quotient:

$$-\frac{\partial j_z}{\partial z} = -\frac{j_b - j_z}{b} \tag{A.27}$$

If no current enters the system from the bottom, j_b vanishes. Since the conductivity in the graphite layer is constant, so is the electric field in the z-direction E_z. Thus the current j_z is can be approximated by:

$$j_z = E_z \cdot \sigma_\parallel = -\frac{\partial \phi}{\partial z} \cdot \sigma_\parallel \approx -\frac{\phi}{b}\sigma_\parallel \tag{A.28}$$

Consequently, the differential equation can be written as

$$-\frac{\partial^2 \phi}{\partial x^2} = -\frac{\phi}{b^2}\frac{\sigma_\parallel}{\sigma_\perp} \tag{A.29}$$

which can also be expressed as

$$\phi'' - \beta^2 \phi = 0 \tag{A.30}$$

with:

$$\beta = \sqrt{\frac{\sigma_\parallel}{b^2 \cdot \sigma_\perp}} \tag{A.31}$$

If the potential vanishes for $x \to \infty$, the solution is given by

$$\phi(x) = U_0 e^{-\beta x} \tag{A.32}$$

with the voltage between the boundary to the aluminum and the boundary to the parallel domain U_0.

To calculate the resistance, the total current across the boundary layer to the intermediate domain is determined. The current density at this point is

$$j = -\sigma_\perp \frac{\partial \phi}{\partial x}\bigg|_{x=0} = U_0 \sigma_\perp \beta \tag{A.33}$$

so the total current is

$$I = b \cdot L \cdot j = b \cdot L \cdot U_0 \cdot \sigma_\perp \cdot \beta \tag{A.34}$$

and the resistance:

$$R = \frac{U_0}{I} = \frac{1}{L}\sqrt{\frac{1}{\sigma_\perp \sigma_\parallel}} \tag{A.35}$$

The total resistance according to this approximation is given by:

$$R_C = R + \frac{1}{2}R_1 = \frac{1}{L}\sqrt{\frac{1}{\sigma_\perp \sigma_\parallel}} + \frac{c}{2 \cdot b \cdot L \cdot \sigma_\perp} \tag{A.36}$$

For $b = c = 10^{-3}m$, $L = 0.18m$ and isotropic graphite the circulation resistance in this approximation is:

$$R_C = \frac{3}{0.18\,\text{m} \cdot 4200\,\text{S} \cdot \text{m}^{-1}} \approx 4 \cdot 10^{-3}\Omega \tag{A.37}$$

Although this approximation does not give exact quantitative results, it gives the correct qualitative dependencies.

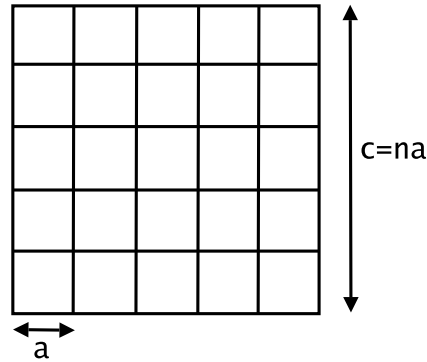## A.5 Normal resistance of a diffusion layer consisting of graphite fabric

Figure A.8: Cross section of a wire. The wire consists of n fiber layers, each consisting of n fibers. Both wire and fiber have quadratic cross sections, with the edge length of a fiber a. Thus the edge length of a wire is $n \cdot a$.

The diffusion layer between MEA and flowfield plates consists of a graphite fabric, which has a pressure-dependent normal resistance in the order of isotropic graphite, although only a small fraction of the space is filled with material. Small graphite fibers are skewed to wires, which are weaved to the diffusion layer. In order to approximate the normal resistance of the diffusion layer analytically only one wire with a quadratic cross section is investigated, which has the height of the total layer thickness. Since the individual fibers are skewed, each fiber layer has contact to both the upper and the lower boundary.
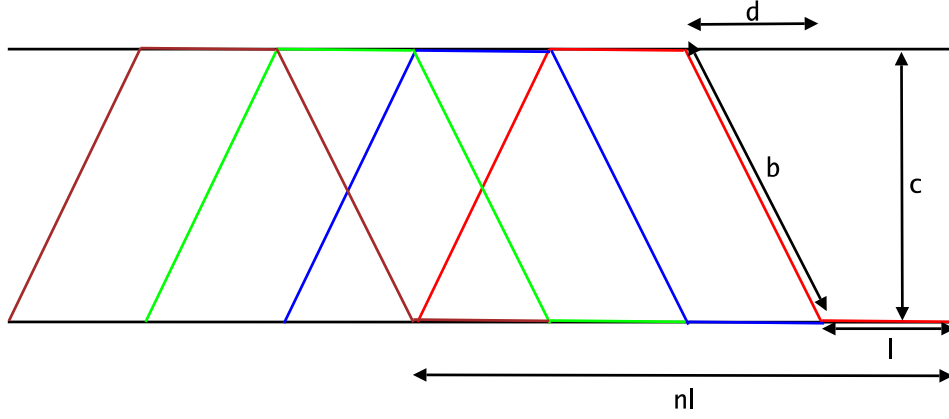
Figure A.9: Profile of a wire. The different colors indicate individual fiber layers. These have overlays with the lower boundary and with the upper boundary, both have the length l. In between these overlays, the way length is b. This is repeated periodically, while the periodicity is given by l and the number of fiber layers in a wire n.

Following Fig. (A.8) and Fig. (A.9) the length of a period is $n \cdot l$, therefore the length d is given by:

$$d = \frac{nl}{2} - l \tag{A.38}$$

The way b between the overlays is therefore:

$$b = \sqrt{d^2 + c^2} = \sqrt{\left(\frac{nl}{2} - l\right)^2 + c^2} \tag{A.39}$$

The total electric resistance of a single fiber layer is determined by the contact resistance R_{C} and the resistance of the fiber. The resistance of one contact is:

$$R_1 = \frac{2 \cdot R_{\mathrm{C}}}{a \cdot n \cdot l \cdot f(p)} \tag{A.40}$$

Here, $f(p)$ is a pressure dependent function describing how many fibers of a fiber layer are actually in contact with the boundary at a given pressure (at $f(p) = 1$ all fibers of a layer have contact to the boundary). Due to symmetry reasons the length of the overlay contributes only half. Following this, the fiber resistance is given by:

$$R_2 = \frac{b + l}{\sigma_{\parallel} \cdot n \cdot a^2 \cdot f(p)} \tag{A.41}$$

A current between different fibers are neglected[3], therefore current enters and leaves the fiber only at the overlays. The resistance of an entire period is given by:

$$R_{per} = \frac{1}{2n}\left(2R_1 + R_2\right) = \frac{1}{2n}\left(\frac{4 \cdot R_C}{a \cdot n \cdot l \cdot f(p)} + \frac{b+l}{\sigma_\parallel \cdot n \cdot a^2 \cdot f(p)}\right) \tag{A.42}$$

The contact resistance has a double contribution, since it occurs at the upper and lower boundary. As the fiber layers are of identical resistance and connected parallel, the resistance is divided by the number of current channels. In a period one fiber forms two connections between the upper and the lower boundary, therefore the resistance is divided by $2n$. The total resistance of a wire is given by the number of periods N in it. With $R_{tot} = R_{per}/N$ and $N = L_w \cdot (nl)^{-1}$ (L_w is the length of the wire) follows:

$$R_{tot} = \frac{l}{2L_w}\left(\frac{2 \cdot R_C}{a \cdot n \cdot l \cdot f(p)} + \frac{b+l}{\sigma_\parallel \cdot n \cdot a^2 \cdot f(p)}\right) \tag{A.43}$$

The collectivity of all wires in a diffusion layer should only fill a fraction α of its area:

$$L_w \cdot n \cdot a = A_w = \alpha \cdot A_{DL} = \alpha L^2 \tag{A.44}$$

$$\Longrightarrow L_w = \frac{L^2\alpha}{na} \tag{A.45}$$

$$R_{tot} = \frac{n \cdot a \cdot l}{2 \cdot L^2 \cdot \alpha}\left(\frac{2R_C}{a \cdot n \cdot l \cdot f(p)} + \frac{b+l}{\sigma_\parallel \cdot n \cdot a^2 \cdot f(p)}\right) \tag{A.46}$$

Investigating the specific resistance of the diffusion layer $\rho = R_{tot}L^2/c$, it follows:

$$\rho = \frac{l}{2 \cdot \alpha \cdot f(p) \cdot c}\left(\frac{2R_C}{l} + \frac{b+l}{\sigma_\parallel \cdot a}\right) \tag{A.47}$$

The contact resistance is approximated by resistance of the half fiber:

$$R_C = \frac{a}{2\sigma_\perp} \tag{A.48}$$

The length of the overlay l depends on a:

$$l = \beta a \tag{A.49}$$

This leads to:

$$b = \sqrt{\left(\frac{nl}{2} - l\right)^2 + c^2} = \sqrt{\frac{c^2\beta^2}{4} - c\beta^2 a + \beta^2 a^2 + c^2} = \sqrt{c^2\left(\frac{\beta^2}{4} + 1\right) + a\beta^2(a - c)} \tag{A.50}$$

---

[3]If the current between fibers is included, the normal resistance of the diffusion layer is less. Thus if the approximation describes the low normal resistance well, there is no need to include this effect.

Using the previous equation, the resistance becomes:

$$\rho = \frac{\beta}{2 \cdot \alpha \cdot c \cdot f(p)} \left(\frac{a}{\beta \cdot \sigma_\perp} + \frac{\sqrt{c^2 \left(\frac{\beta^2}{4} + 1 \right) + a\beta^2(a - c)} + \beta a}{\sigma_\parallel} \right) \tag{A.51}$$

Now, if the fiber size goes to zero:

$$lim_{a \to 0}\rho = \frac{\beta}{2 \cdot \alpha \cdot f(p)} \cdot \frac{\sqrt{\frac{\beta^2}{4} + 1}}{\sigma_\parallel} \tag{A.52}$$

For large pressures $f(p)$ is unity. With $\alpha = 0.2$ and $\beta = 2$ follows

$$lim_{a \to 0}\rho = \frac{2\sqrt{\frac{2^2}{4} + 1}}{2 \cdot 0.2 \cdot \sigma_\parallel} = 5\sqrt{2}\rho_\parallel \tag{A.53}$$

and:

$$\sigma_{DL} = \sigma_\parallel \frac{1}{5\sqrt{2}} \tag{A.54}$$

For the transverse conductivity $\sigma_\parallel$, the corresponding value of Sigraflex is used

$$\sigma_{DL} = \frac{110\,\text{S} \cdot \text{mm}^{-1}}{5\sqrt{2}} = 15.5\,\text{S} \cdot \text{mm}^{-1} \tag{A.55}$$

which is by a factor of four larger than the conductivity of isotropic graphite ($\sigma_{\text{isotropic}} = 4\,\text{S} \cdot \text{mm}^{-1}$). This shows, that even though the transverse conductivity of the diffusion layer is very large, it is possible to have a higher normal conductivity than that of isotropic graphite.

Bibliography

[1] McLean, G.F., Niet, T., Prince-Richard, S., Djilali, N., 2002, "An assessment of alkaline fuel cell technology", Int. J. Hydrogen Energy **27**, pp. 507–526

[2] Tu, H., Stimming, U., 2004, "Advances, aging mechanisms and lifetime in soli-oxide fuel cells", J. Power Sources **127**, pp. 284–293

[3] Wind, J., Spah, R., Kaiser, W., and Bohm, G., 2002, "Metallic bipolar plates for PEM fuel cells", J. Power Sources **105**, pp. 256–260.

[4] Larminie, J., Dicks, A., 2003, "Fuel Cell Systems Explained", John Wiley & Sons Ltd., West Sussex

[5] Dohle, H., Schmitz, H., Bewer, T.,Mergel, J., and Stolten, D., 2002, "Development of a compact 500 W class direct methanol fuel cell stack", J. Power Sources **106**, p. 313.

[6] Heinzel, A., Nolte, R., Ledjeff-Hey, K., and Zedda, M., 1998, "Membrane fuel cells – concepts and system design", Electrochim. Acta **43**, pp. 3817–3820.

[7] Mikkola, M., 2001, "Experimental Studies on Polymer Electrolyte Membrane Fuel Cell Stacks", Master Thesis at the Helsinki University of Technology

[8] Wang, L., Husar, A., Zhou, T. and Liu, H., 2003, "A parametric study of PEM fuel cell performances", Int. J. Hydrogen Energy **28**, pp. 1263–1272.

[9] Tüber, K., Pócza, D., and Hebling, C., 2003, "Visualization of water buildup in the cathode of a transparent PEM fuel cell", J. Power Sources **124**, pp. 403–414.

[10] Tüber, K., Zobel, M., Schmidt, H., and Hebling, C., 2003, "A polymer electrolyte membrane fuel cell system for powering portable computers", J. Power Sources **122**, pp. 18.

[11] Scott, K., Taama, W.M., and Argyropoulos, P., 1999, "Engineering aspects of the direct methanol fuel cell system", J. Power Sources **79**, p. 43T.

[12] Yoon, Y.G., Lee, W.Y., Yang, T.H., Park, G.G., and Kim, C.S., 2003, "Current distribution in a single cell of PEMFC", J. Power Sources **118**, p. 193.

[13] Noponen, M., Mennoloa, T., Mikkola, M., Hottinen, T., and Curnd, P., 2002, "Measurement of current distribution in a free-breathing PEMFC", J. Power Sources **106**, pp. 304–312.

[14] K. Wippermann, private communication

[15] Kulikovsky, A.A., 2006, "Electrostatic broadening of current-free spots in a fuel cell stack: The mechnism of stack aging?", Electrochem. Commun. **8**, pp. 1225–1228.

[16] J. Stumper, S.A. Campbell, D.P. Wilkinson, M.C. Johnson and M. Davis, 1998, "In-situ methods for the determination of current distributions in PEM fuel cells", Electrochim. Acta **43**, pp. 3773 –3783.

[17] Yuan, X., Sun, J.C., Wang, H., and Zhang, J., 2006, "AC impedance diagnosis of a 500 W PEM fuel cell stack Part II: Individual cell impedance", J. Power Sources **161** (2), pp. 929–937.

[18] Mennola, T., Mikkola, M., Noponen, M., Hottinen, T., and Lund, P., 2002, "Measurement of ohmic voltage losses in individual cells of a PEMFC stack", J. Power Sources **112**, pp. 261–272.

[19] Wieser, C., Helmbold, A., and Gülzow, E., 2000, "A new technique for two-dimensional current distribution measurements in electrochemical cells", J. Appl. Electrochem. **30**, pp. 803–807

[20] Lustfeld, H., Reißel, M., Schmidt, U., and Steffen, B., "Reconstruction of Electric Currents on a Fuel Cell by Magnetic Field Measurements", J. Fuel Cell Sci. Technol., in press

[21] Hauer, K.H., and Potthast, R., 2007, "Magnetic tomography for fuel cells - current status and problems", J. Phys.: Conf. Ser. **73**, Issue 1, pp. 012008.

[22] Hauer, K.H., Potthast, R., and Wannert, M., 2008, "Algorithms for magnetic tomography on the role of a priori knowledge and constraints", Inverse Problems **24** pp. 045008.

[23] Tübner, K., 2004, "Analyse des Betriebsverhaltens von Polymer-Elektrolyt-Membran-Brennstoffzellen für portable Systeme", Dissertation at the Universität Duisburg-Essen

[24] Mortimer, C.E., Müller, U., 2003, "Chemie", Georg Thieme Verlag, Stuttgart

[25] Blomen, L. J. M. J., Mugerwa, M. N., 1993, "Fuel Cell Systems", Plenum Press, New York

[26] Kordesch, K., Simader, G., 1996, "Fuel Cells and Their Applications", VCH Verlagsgesellschaft mbH, Weinheim

[27] Vielstich, W., Lamm, A., Gasteiger, H. A., 2003, "Handbook of fuel cells Vol. 1", John Wiley & Son Ltd., West Sussex

[28] Rayment, C., Sherwin, S., 2003,"Introduction to fuel cell technology", University of Notre Dame

[29] Wippermann, K., 2004, "Brennstoffzellen - Eine Zukunftstechnologie?", lecture notes FH Aachen

[30] Haber, E., Ascher, U. M., 2001, "Fast finite volume simulation of 3D electromagnetic problems with highly discontinuous coefficients", SIAM J. Sci. Comput. Vol. **22** No.6, pp. 1943–1961

[31] Bärwolff, G. 2006, "Numerik partieller Differentialgleichungen", lecture notes TU Berlin

[32] Press, W. H., Teukolsky, S. A., Vetterling, W. T., Flannery, B.P., 2007 "Numerical Recipies", Cambridge University press, Cambridge

[33] Lustfeld, H., 2008, "Neuronale Netze und Support Vektor Maschinen (SVM) in Physik, Geophysik, Chemie und Industrie II", lecture notes Universität Duisburg-Essen

[34] Lustfeld, H., Reißel, M., Steffen, B., 2007, "Defektkontrolle für ein oder mehrere elektrische Betriebselemente", Deutsche Patentanmeldung DE: 102007061642.4-35 (20.12.2007)

[35] Hirschfeld, J. A., Lustfeld, H., Reißel, M., Steffen, B., 2008, "Precise Diagnostics and Effective Stabilization of Currents in a Fuel Cell Stack", submittet to J. Fuel Cell Sci. Technol.

[36] Lustfeld, H., Reißel, M., Steffen, B., 2008, "Magnetotomography and Electruc Currents in a Fuel Cell", submitted to Fuel Cells

[37] Dowell, M., Jarratt, P., 1972, "The "Pegasus" method for compution the root of an equation", BIT **12**, pp. 503–508

[38] King, R. F., 1973, "An improved Pegasus method for root finding", BIT **13**, pp. 423–427

[39] Bronstein, I. N., Semendjajew, K. A., Musiol, G., 2000, "Taschenbuch der Mathematik", Verlag Harry Deutsch, Frankfurt am Main

Acknowledgments

I would like to thank my supervisor PD. Dr. Hans Lustfeld for his patience and his massive confidence in me. But especially I thank him for always finding time to discuss my problems and help me solve them.

Further thanks to Dr. Bernhard Steffen and Prof. Dr. Martin Reißel for helpful discussions and for professionally supporting my work. I specially thank the latter one for his immediate aid whenever I had problems with his code.

At last I want to thank Prof. Dr. Stefan Blügel to enable me to do my diploma thesis in his institute.